LOW-COST SUB-NYQUIST SAMPLING HARDWARE AND ALGORITHM CO-DESIGN FOR WIDEBAND AND HIGH-SPEED SIGNAL CHARACTERIZATION AND MEASUREMENT

A Dissertation
Presented to
The Academic Faculty

by

Nicholas Lin Tzou

In Partial Fulfillment
of the Requirements for the Degree
Doctor of Philosophy in the
School of Electrical and Computer Engineering

Georgia Institute of Technology
May, 2014

LOW-COST SUB-NYQUIST SAMPLING HARDWARE AND ALGORITHM CO-DESIGN FOR WIDEBAND AND HIGH-SPEED SIGNAL CHARACTERIZATION AND MEASUREMENT

Approved by:

Dr. Abhijit Chatterjee, Advisor
School of Electrical and Computer Engineering
Georgia Institute of Technology

Dr. David Keezer
School of Electrical and Computer Engineering
Georgia Institute of Technology

Dr. Mark Davenport
School of Electrical and Computer Engineering
Georgia Institute of Technology

Dr. Le Song
School of Computer Science Engineering
Georgia Institute of Technology

Dr. Madhavan Swaminathan
School of Electrical and Computer Engineering
Georgia Institute of Technology

Date Approved: March 31, 2014

To my family…

ACKNOWLEDGEMENTS

First and foremost, I would like to express my sincere gratitude to my advisor Dr. Abhijit Chatterjee for his guidance, encouragement, and constant support throughout the course of my PhD. I would like to thank him for providing me an opportunity to conduct research under his guidance. I would never have been able to finish this dissertation without his help. Over the years, our numerous discussions have had a significant influence in my professional and personal outlook. He is a remarkable person who has made this entire journey highly interesting.

I am also grateful to my committee members: Dr. Mark Davenport for serving as the chair of my PhD proposal exam, Dr. Madhavan Swaminathan, Dr. David Keezer, and Dr. Le Song for their individual time and advice. The dissertation would never have been possible without their precious input.

I would like to acknowledge all my colleagues in Dr. Abhijit Chatterjee's lab: Dr. Shyam Kumar Devarakond, Dr. Sen-Wen Hsiao, Dr. Aritra Banerjee, Joshua W. Wells, Jayaram Natarajan, Debesh Bhatta, Thomas Moon, Xian Wang, Sabyasachi Deyati, Suvadeep Banerjee, and Barry John Muldrey Jr. for their support and friendship.

My deepest gratitude is given to my beloved parents, Leon Tzou and Bih-Fong Chang Tzou, and my wife, Wei-Chen Li. I would also like to thank my sister and brother-in law Olivia Tzou and Kuan-Tsen Chen. Your unconditional love and support keep me motivated in the long journey. I dedicated this dissertation to them.

TABLE OF CONTENTS

LIST OF TABLES

LIST OF FIGURES

LIST OF SYMBOLS AND ABBREVIATIONS

3G	3rd generation; 3rd generation of mobile telecommunications technology
4G	4th generation; 4th generation of mobile telecommunications technology
ADC	analog-to-digital converter
ADRS	asynchronous dual-rate sampling
AMRS	asynchronous multi-rate sampling
BUJ	bounded uncorrelated jitter
BER	bit error rate
CJ	crosstalk jitter
CR	cognitive radio
CS	compressed sensing
DDJ	data-dependent jitter
DJ	deterministic jitter
DRS	dual-rate sampling
DSP	digital signal processing
DUT	device under test
ETS	equivalent time sampling
Gbps	Giga-bit per second
GHz	Gigahertz
HDMI	high-definition multimedia interface
IEEE	Institute of Electrical and Electronics Engineers
InP	Indium-Phosphide
I/O	input output (interface)
IUS	incoherent undersampling
LFSR	linear-feedback-shift-register
LTE	long-term evolution
MHz	Megahertz
mmW	millimeter-wave
MWC	modulated wideband converter
MRS	multirate sampling
NUS	non-uniform sampling
OPG	optical pulse generator
PJ	periodic jitter
PRBS	pseudo-random bit sequence
RD	random demodulation
RF	radio frequency
RJ	random jitter
RS	random sampling
SDRS	synchronous dual-rate sampling
SMRS	synchronous multi-rate sampling
SoC	system-on-chip
SR	shift-register
TIE	time interval error

USB	universal serial bus
WLAN	wireless local area network
WPAN	wireless personal area network

SUMMARY

Cost reduction has been and will continue to be a primary driving force in the evolution of hardware design and associated technologies. The objective of this research is to design low-cost signal acquisition systems for characterizing wideband and high-speed signals. As the bandwidth and the speed of such signals increase, the cost of testing also increases significantly; therefore, innovative hardware and algorithm co-design are needed to relieve this problem.

In Chapter 2, a low-cost multi-rate system is proposed for characterizing the spectra of wideband signals. The design is low-cost in the sense of the actual component cost, the system complexity, and the effort required for calibration. The associated algorithms are designed such that the hardware can be implemented with low-complexity yet be robust enough to deal with various hardware variations. A hardware prototype is built not only to verify the proposed hardware scheme and algorithms but to serve as a concrete example that shows that characterizing signals with sub-Nyquist sampling rate is feasible.

Chapter 3 introduces a low-cost time-domain waveform reconstruction technique, which requires no mutual synchronization mechanisms. This brings down cost significantly and enables the implementation of systems capable of capturing tens of Gigahertz (GHz) signals for significantly lower cost than high-end oscilloscopes found in the market today. For the first time, band-interleaving and incoherent undersampling techniques are combined to form a low-cost solution for waveform reconstruction. This is enabled by co-designing the hardware and the back-end signal processing algorithms to

compensate for the lack of coherent Nyquist rate sampling hardware. A hardware prototype was built to support this work.

Chapter 4 describes a novel test methodology that significantly reduces the required time for crosstalk jitter characterization in parallel channels. This is done by using bit patterns with coprime periods as channel stimuli and using signal processing algorithms to separate multiple crosstalk coupling effects. This proposed test methodology can be applied seamlessly in conjunction with the current test methodology without re-designing the test setup. More importantly, the conclusion derived from the mathematical analysis shows that only such test stimuli give unbiased characterization results, which are critical in all high-precision test setups. Hardware measurement results and analysis are provided to support this methodology.

This thesis starts with an overview of the background and a literature review. Three major previously mentioned works are addressed in three separate chapters. Each chapter documents the hardware designs, signal processing algorithms, and associated mathematical analyses. For the purpose of verification, the hardware measurement setups and results are discussed at the end of these three chapters. The last chapter presents conclusions and future directions for work from this thesis.

CHAPTER 1

INTRODUCTION

1.1 Motivation

Integrated circuits are the enabling technology behind virtually every electronics device people use on a daily basis. The technology revolution has been driven by reducing the cost of these circuits, which are constantly being pushed by the semiconductor industry to become smaller and faster. Transferring data at higher data rates has required the communication systems to be pushed to operate at wider bandwidths. Many standards have risen to extend the limit of data transmission. USB 3.0 supports a data rate of up to 5 Gbps [1], and finalized USB 3.1 spec doubles the speed to 10 Gbps. HDMI uses a transmission rate of up to 10.2 Gbps [2], DisplayPort has a throughput of up to 21.6 Gbps [3], and Thunderbolt provides a transmission speed of up to 20 Gbps [4]. These standards push not only the data rate of wireline transmission but also the development of RF components to be compatible with these existing wireline interfaces. 4G LTE is capable of data transmission in the gigabit range. Wireless Local Area Network (WLAN) features a mid-range high-speed protocol with IEEE 802.11ad as a new generation standard, which combines the Wireless Personal Area Network (WPAN) mmW multi-gigabit capability with WLAN [5-8]. As a result of this increasing bandwidth, the cost of test equipment for characterizing such wideband and high-speed signals has increased significantly.

The analog-to-digital conversion process is one of the bottlenecks in the design of such systems. Sampling an input signal at its Nyquist rate requires that an ADC sampling

clock frequency has to be twice the input signal bandwidth. Acquiring wideband and high-speed signals increases the expense of Nyquist rate sampling. Therefore, sub-Nyquist sampling has been studied intensively. This form of sampling can be dated back as early as the eighteenth century, when Prony proposed an algorithm to estimate the parameters of a sum of complex exponentials from only a few samples. Since then, much progress has been made. Sub-Nyquist sampling has received even more attention in recent years, which has led people to start developing different sub-Nyquist signal acquisition systems. The realization of high-performance, low-cost, and robust systems requires co-designing both the hardware and the algorithms. However, few of these new systems can resolve the issues of both algorithms and hardware and put the innovations into practice. Some of the existing sub-Nyquist sampling systems with hardware implementations will be reviewed in the later sections. Further research into the design of low-cost sub-Nyquist sampling system is performed and detailed in Chapter 2.

Another way to extend system bandwidth is to use a band-interleaved scheme. This signal acquisition scheme can reduce the required sampling rate as well as the analog input bandwidth for the track-and-hold circuitry, which is placed in front of the ADC to increase the analog input bandwidth. One drawback of the band-interleaved scheme is that it requires mutual synchronization between the mixing signal and the sampling clock. In addition, performing signal time-domain waveform reconstruction requires synchronizing both the input signal and the system clock, which is used as the reference clock for the mixing signals and the sampling clocks. These required synchronization mechanisms significantly drive up the cost of such systems. Innovation is needed to bring down the cost. Chapter 3 of this dissertation presents a low-cost

waveform reconstruction system that combines sub-Nyquist sampling and the band-interleaved scheme without any of the synchronization mechanisms mentioned above.

If reliable products are to be built, all the manufactured components should be properly tested and characterized. In recent years, the development of system-on-chip (SoC) technology has put more components in ever-closer proximity. One result of this is that noise from high-speed and wideband signals easily couples to different parts of the circuitry and can cause signal integrity issues. The noise, such as jitter in digital systems, needs to be characterized properly to ensure reliability, but the time required for such characterization is the source of increased costs. The research in Chapter 4 studies methodologies of and applications for characterizing jitter, the timing noise of high-speed signals. More importantly, this thesis proposes a novel crosstalk separation technique, which dramatically reduces the required time of crosstalk jitter characterization, and thus, reduces the cost of testing. Jitter analysis techniques will be reviewed in this chapter. Further research on jitter separation is discussed in Chapter 4.

1.2 Organization

The content of this thesis is organized as follows: Section 1.3 reviews the developments of sub-Nyquist signal acquisition systems for sparse spectrum recovery. The focus of this section is the systems that have the potential to be implemented in hardware. These include multi-coset sampling, Random Sampling, Random Demodulation, Modulated Wideband Converter, and multi-rate sampling. Hardware prototypes of some of these systems have been implemented and verified. Some difficulties with and drawbacks of these hardware implementation are highlighted.

Section 1.4 reviews multiple architectures of time-domain signal measurement systems. The end applications of these measurement systems are oscilloscopes. The focus here will be on those that extend the input bandwidth with mixers, which is used in the band-interleaved scheme. Section 1.5 reviews various high-speed signal jitter analysis techniques and highlights the importance of jitter separation and characterization.

A sub-Nyquist multi-rate system is proposed as a low-cost solution for sensing signals with a sparse spectrum in Chapter 2. This work combines signal processing algorithms and low-cost hardware designs. Section 2.1 starts with the multi-rate algorithm, which is designed for low-cost implementation. The algorithm is a two-step approach, with each step illustrated in Sections 2.1.1 and 2.1.2. Section 2.2 introduces the associated multi-rate hardware design. The proposed hardware sub-Nyquist sampling scheme is compared with some schemes reviewed in Section 1.3. A hardware prototype is built and tested along with the proposed algorithms in Section 2.3. A brief summary is made in Section 2.4.

Chapter 3 develops a band-interleaved incoherent undersampling scheme, which is a combination of two techniques, as a low-cost solution for waveform reconstruction. Section 3.1 first introduces incoherent undersampling and related advancements. Section 3.2 applies the band-interleaved scheme to incoherent undersampling. However, the underlying hardware still suffers from the complications involved in synchronization. In Section 3.3, with associated back-end signal processing, all the mutual synchronization requirements are removed, and the major work of this chapter is addressed. This section details the algorithms and the hardware designs. A prototype is built, and the hardware measurement is performed to verify the concept. Section 3.4 summarizes Chapter 3.

The main contribution in Chapter 4 is crosstalk jitter separation. Section 4.1 starts this chapter by discussing characterizing periodic jitter with incoherent undersampling and its associated applications, including system characterization, diagnosis, and tuning. Section 4.2 introduces the crosstalk jitter separation technique and describes how this method can save time for characterization. In addition, the method can be directly applied to a traditional jitter characterization setup. Section 4.2 also presents a mathematical analysis, explains the limitation of this technique, and provides the hardware verifications using the incoherent undersampling or an oscilloscope from the market. Section 4.3 summarizes the chapter.

Chapter 5 is the conclusion of this work. Section 5.1 highlights the technical contributions presents the conclusions of this thesis. Potential future work is discussed in Section 5.2.

1.3 Spectrum Characterization of Sparse Multi-Band Signals with Sub-Nyquist Sampling

For signals having sparse representations in frequency domain, it is possible to recover the signals with a sub-Nyquist sampling rate. Numerous sub-Nyquist sampling schemes have been studied. These schemes can actually be traced back as early as the eighteenth century. In 1795, Gaspard de Prony proposed to estimate parameters of complex exponentials with a small number of complex samples in the presence of noise [12]. In the early 1900s, Carathéodory showed that a positive linear combination of any k sinusoids is uniquely determined by its value at t=0 and any other $2k$ points [13, 14]. If k is small and the frequency range of the sinusoids is large, it implies that far fewer

samples than the number of Nyquist-rate samples are needed to recover the k sinusoids [15]. Progress in the research of sub-sampling was also done in other fields. George, Gorodnitsky, and Rao studied sparsity in biomagnetic imaging and other contexts and generalized Carathéodory's work [16-19]. Bresley, Feng, and Venkataramani proposed a sampling scheme to recover k components with non-zero bandwidths [20-23]. Compared to the previous methods, the k components to be recovered can have certain bandwidth, instead of sinusoidal tones, but exact recovery was not guaranteed. In the early 2000s, Blu, Marziliano, and Vetterli developed sampling methods for signals that can be represented using k parameters and the associated functions [24]. They showed that these signals can be recovered with only $2k$ samples. More recently, Candes, Romberg, and Tao [25-29] and Donoho [30] showed that a signal having a sparse representation can be recovered accurately from a small set of linear non-adaptive measurements [15]. The result shows that the sparse signal can be recovered with high probability by using a few incoherent measurements.

The concept of recovering original signals with a small number of measurements has also been studied in many other fields. In this research, the particular focus is on the applications of signals having sparse representation in the frequency domain. Among a wide spectrum of sub-Nyquist sampling techniques and algorithms, some have the potential to be implemented in hardware as signal acquisition systems. These techniques are selected for further review in the following sub chapters.

1.3.1 Multi-coset Sampling

Multi-coset sampling, also known as Periodic Non-Uniform sampling, is one of the most extensively studied sub-Nyquist sampling schemes [22, 40-42].

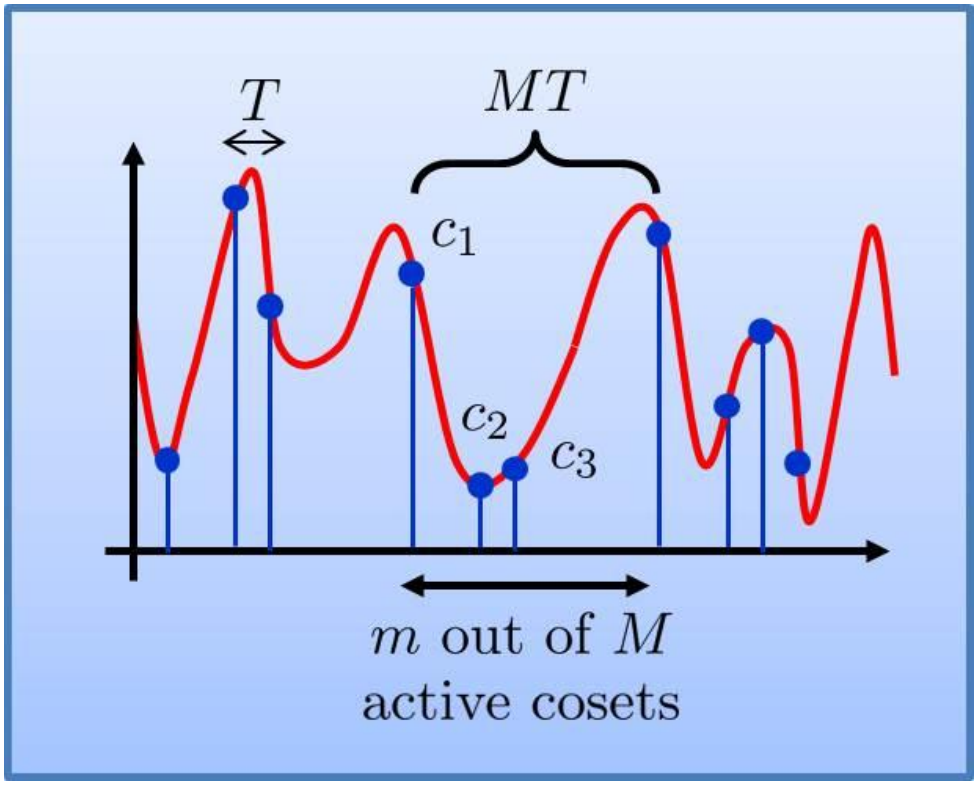

Figure 1.1. Multi-coset sampling [43]

As shown in Figure 1.1, periodic non-uniform sampling is obtained by selecting a sampling pattern of m points within an interval of length MT, where T is the Nyquist interval, and then repeating this sampling pattern on consecutive intervals of length MT. Multiple channels sample at a common relatively low sampling rate, but each channel has a different sampling offset, which is an integer multiple of reciprocal of a rate ($1/T$) that is equal to or greater than the Nyquist rate. Samples from different channels are then combined to form a periodic non-uniform sample set. A multi-channel implementation is shown as Figure 1.2 (a).

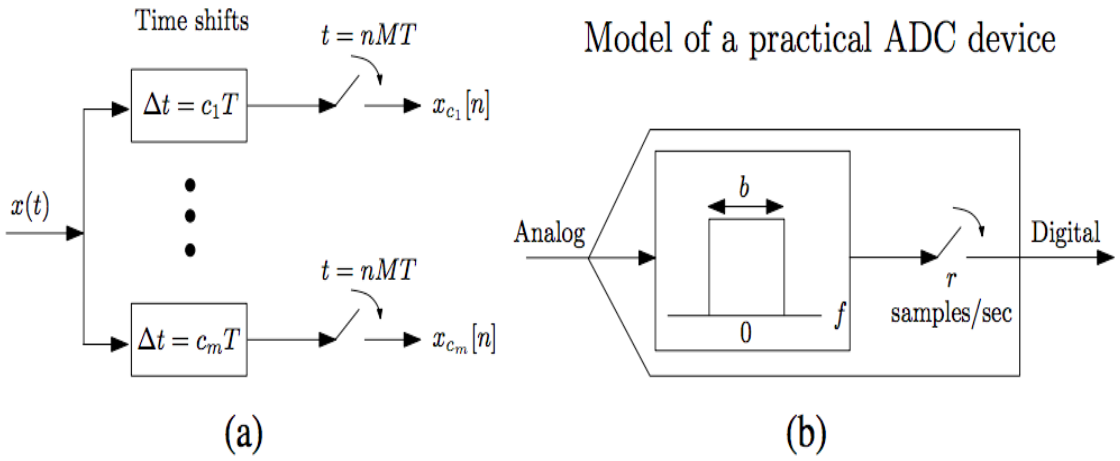

Figure 1.2. Schematic implementation of multi-coset sampling (a) requires no filtering between the time shifts and the actual sampling. However, the front-end of a practical ADC has an inherent bandwidth limitation, which is modeled in (b) as a lowpass filter preceding the uniform sampling [44]

The original signal can be obtained by solving a system of linear equations. One limitation of multi-coset sampling is that it is difficult to maintain accurate time delays between the ADCs of different cosets. This means that a multi-coset system requires intensive delay calibration and control in order to work. Maintaining accurate time delays between ADCs in the order of Nyquist interval T is difficult. Any uncertainty in these delays hobbles the recovery using the sampled sequences [45]. Algorithms have been proposed to compensate for timing mismatches with increasing substantial complexity to the receiver [46, 47]. The other limitation is that a typical multi-coset system relies on an implicit assumption that the individual samplers are exposed to the entire frequency range. This assumption prohibits current anti-aliasing low pass filter and the band-interleaved schemes.

1.3.2 Random Sampling & Non-Uniform Sampling

Random sampling (RS) and non-uniform sampling (NUS) [48, 49] are sampling schemes in which the input signals are sampled at irregularly spaced sampling time. The idea behind RS and NUS is shown as Figure 1.3.

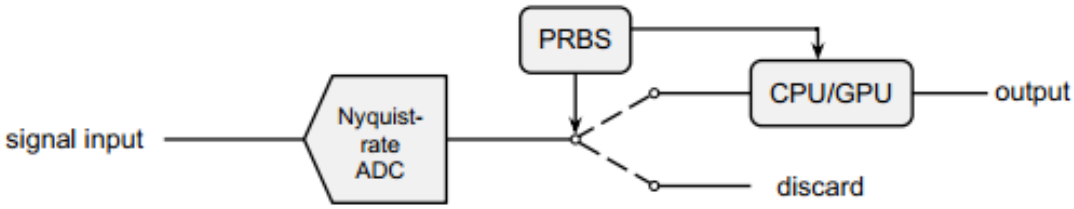

Figure 1.3. Conceptually, the NUS takes Nyquist-rate samples of the input signal and then randomly discards most of the samples [49].

Pseudo-random bit sequences, generated by a linear-feedback-shift-register (LFSR), are used as the random sampling timing. As can be seen from Figure 1.3, this hardware implementation concept is not a good fit as a solution to the problem to solve. The sampling rate is limited by the ADC sampling rate. This drawback violates the motivation of sub-Nyquist rate sampling. However, it can be a potential low-power signal acquisition solution if the back-end signal processing computation can be reduced.

Two hardware prototypes have been implemented [48, 49]. The RS hardware implementation consists of a signal acquisition unit and a digital signal processing unit. The signal acquisition unit is responsible for obtaining the required random samples according to a predetermined random sequence. The digital signal processing unit is responsible for recovering the signal from a few random samples without prior knowledge about the acquired signal except its sparsity. Sparsity, K, which is the number

of single tones included in the signal, is a measure of the signal complexity. Figure 1.4 shows a block diagram for Random Sampling hardware implementation.

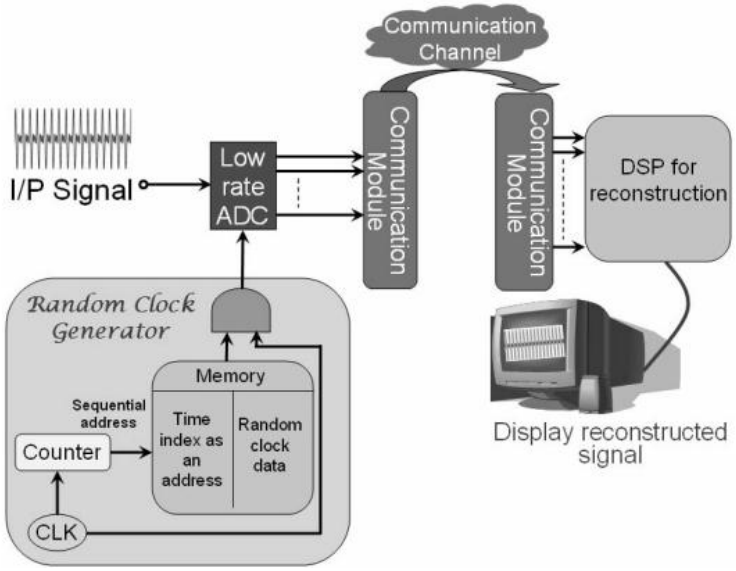

Figure 1.4. Random Sampling (RS) Architecture [48]

The signal acquisition unit consists of a random clock, which drives a traditional low-rate ADC to sample the input signal only at specific timings. As shown in Figure 1.4, the random clock is implemented on an FPGA and generates a predetermined pseudo-random sequence of pulses, which indicate the timings to sample the signal. This prototype demonstrates the concept of RS and is able to recover signals in the KHz range.

The other hardware prototype implements an NUS sampling scheme [49]. Conceptually, it is the same as shown in Figure 1.3. Customized Indium-Phosphide (InP) sample-and-hold circuitries are used to increase analog input bandwidth. A maximum sampling rate 4.4 Gsps ADC is used to acquire the input signal with the sample-and-hold circuitry in front of the ADC to increase the bandwidth to 2.4 GHz. GPU and associate parallel programing are used to reduce the computation time of the recovery algorithm.

The block diagram of the NUS system and the hardware image are shown in Figures 1.5 and 1.6.

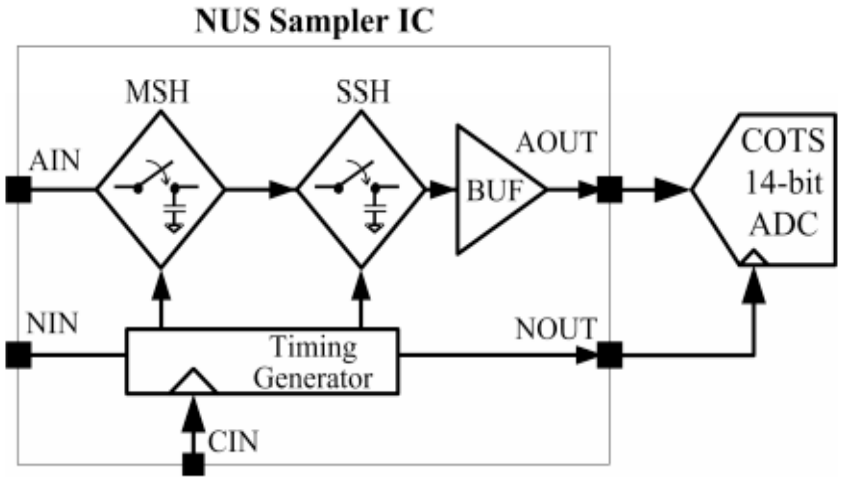

Figure 1.5. Simplified block diagram of non-uniform sampler (NUS) receiver. The NUS sampler IC (left block) was implemented with the Northrop Grumman Aerospace Systems (NGAS) InP HBT process. [49]

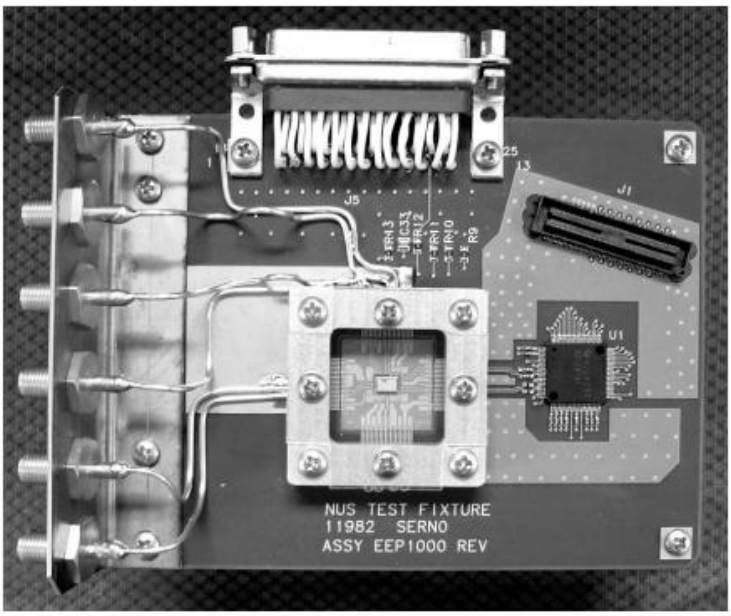

Figure 1.6. NUS test fixture. The NUS IC is mounted on a custom pallet. Also shown is the 14-bit ADC as well as various test equipment connector interfaces. [49]

1.3.3 Random Demodulation

In Random Demodulation, the input signal is mixed with a pseudo-random bipolar wave sequence using an analog multiplier to randomly modulate the input signal in the time domain [50-53]. This is followed by an integrator, which is implemented as a Gm-C based differential integrator in [52]. The bit rate of the bipolar wave sequence should be higher than the Nyquist rate of the input signal, and the integrator serves as a low-pass filter. Each measurement is digitized using a low-rate ADC and is sent to the reconstruction unit.

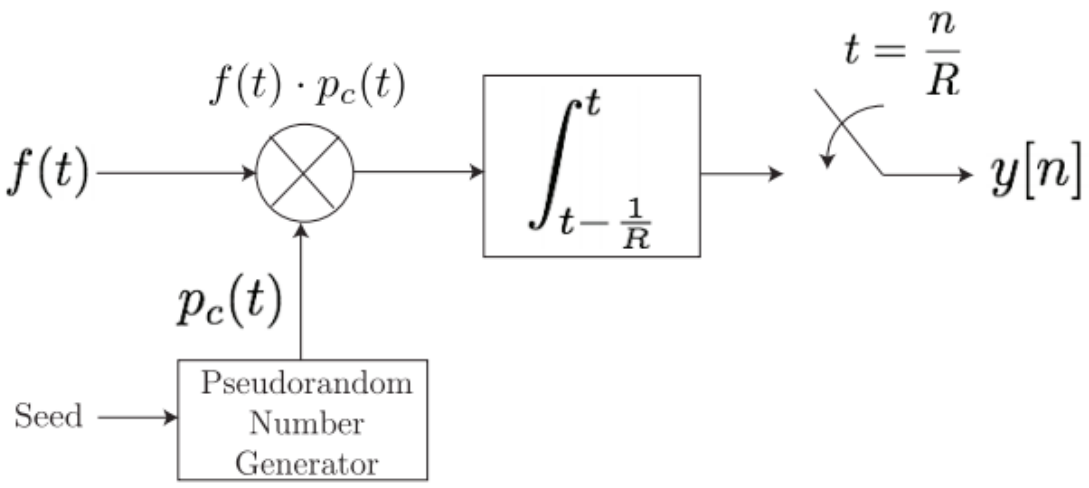

Figure 1.7. Block diagram for the random demodulator. The components include a random number generator, a mixer, an accumulator, and a sampler [51]

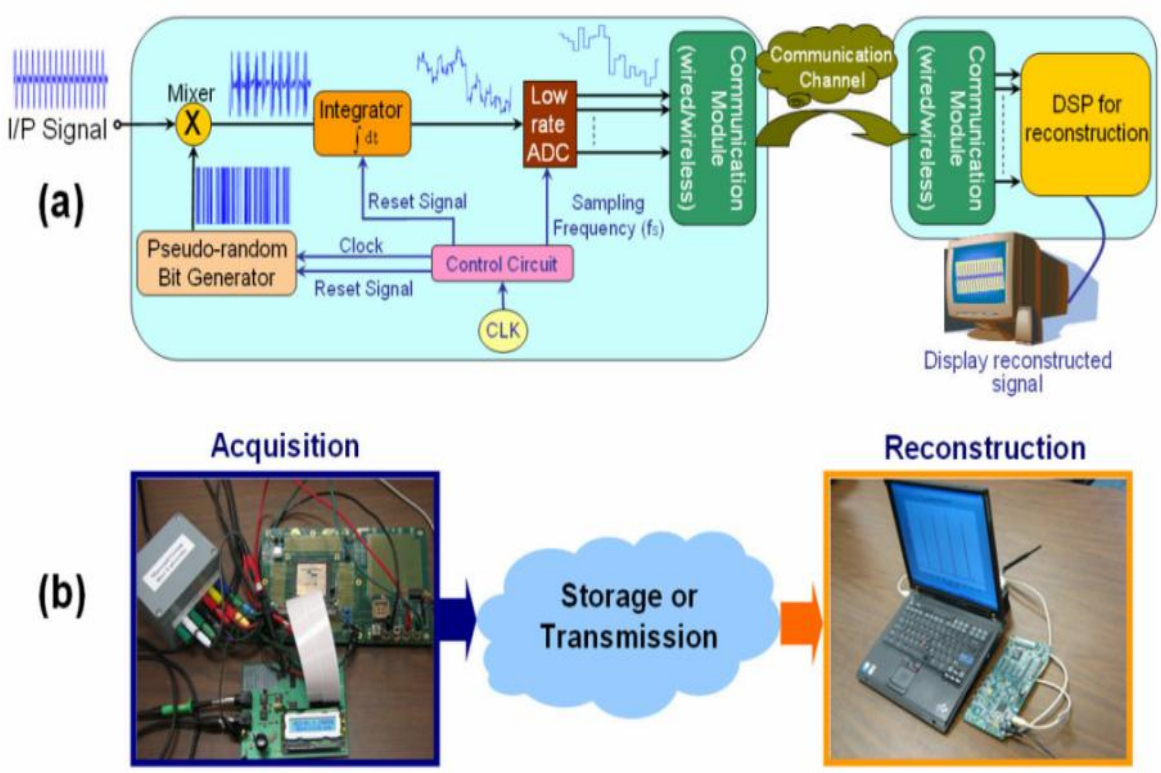

Figure 1.8. (a) The hardware block diagram for the compressive analog-to-digital converter (CADC) prototype and (b) The actual implementation of the CADC prototype [52]

The block diagram is shown as Figure 1.7. The demodulation process ensures that each tone has a distinct signature within the passband of the filter. Since there are few tones present, it is possible to identify the tones and their amplitudes from the low-rate samples. A hardware prototype is implemented in [52], and the prototype setup is shown in Figure 1.8. The limitation of random demodulation is that the system is susceptible to hardware imperfections. For example, the signal integrity of high-speed sequences is already an issue. Different types of jitter of the random bit sequence can cause non-ideality and degrade the system performance. In addition, the non-linearity and bandwidth limitation of the mixer and the integrator make it difficult to consider this system as a good answer to the problem addressed previously.

1.3.4 Modulated Wideband Converter

The input signal $x(t)$, as shown in Figure 1.9, enters a modulated wideband converter (MWC) system and is split into m different channels. [20] The signal in each channel is multiplied by a different periodic mixing function $p_i(t)$ with period T_p. After the mixing, the signal spectrum is truncated by a low-pass filter with cutoff $1/(2T_S)$, and the signal is sampled at rate $1/T_S$.

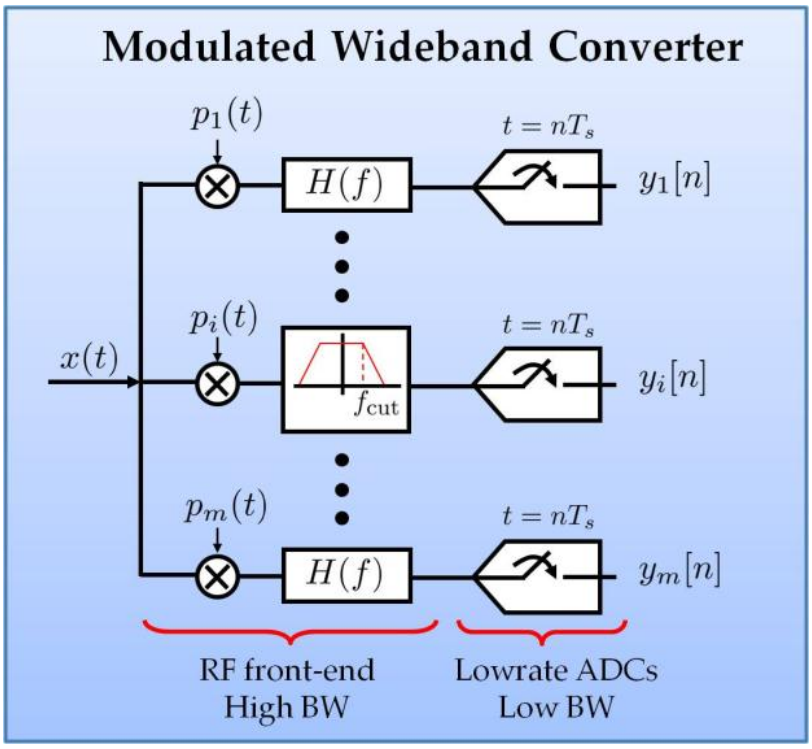

Figure 1.9. Modulated Wideband Converter [43]

The advantage of MWC over the multi-coset scheme is that the low-pass filters serve as anti-aliasing filters in conventional signal acquisition systems, which makes existing commercial ADCs available for the task. An MWC system is implemented with off-the-shelf components and verified as described in [54]. The limitation of the MWC system is that intensive system calibration is needed in different stages. In the mixing stage, the spectrum and phase of $p_i(t)$ should be characterized. The phase and the amplitude

response of the low pass filter should be characterized as well. In addition, the response of the wideband mixer should be calibrated as well. The scaling capability is also limited by the complexity of the system. The hardware implementation is shown in Figure 1.10.

Figure 1.10. MWC hardware prototype [54]

(Left) The analog board realizing four sampling channels. It consists of three stages: splitting the analog input, mixing with four input periodic waveforms (connectors on the rear), and lowpass filtering.

(Right) The digital board provides four sign-alternating periodic waveforms, which are derived from a single shift-register (SR) chain.

1.3.5 Multi-rate Sampling

Another work worth mentioning is the multi-rate sampling scheme. Asynchronous multi-rate sampling (MRS) and synchronous multi-rate sampling (SMRS) were used for reconstructing sparse multiband signals in [55] and [56], respectively. In addition, MRS has been successfully implemented in experiments using an electro-optical system with three sampling channels, as described in [57].

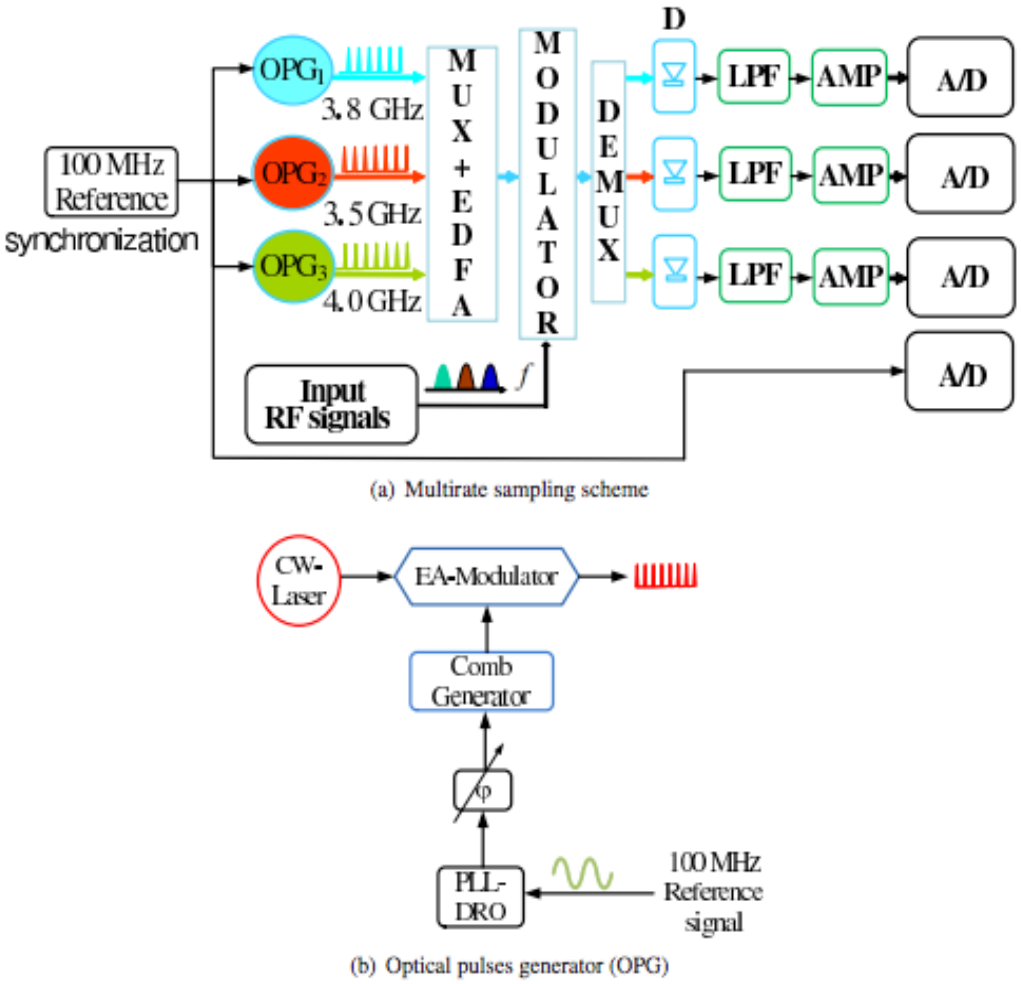

Figure 1.11. Multi-rate Sampling Scheme [57]

Both systems employ three optically pulsed sources that operate at different rates and at different wavelengths. A non-conventional ADC is designed by means of high-rate optical devices. The hybrid optic-electronic system introduces a front-end whose bandwidth reaches the wideband regime at the expense and size of an optical system. As shown in Figure 1.11, optical pulses are generated using three optical pulse generator (OPG) units. A wideband signal with an 18 GHz bandwidth is constructed by amplifying the modulated pulses , which are (then) sampled by an ADC at a constant rate of 4 GHz

in each channel. For synchronous multi-rate sampling system, one limitation is the synchronization issue across different channels. This is actually an issue for all multi-channel systems. (Multi-coset and MWC)

1.3.6 Challenges

Efforts have been made to convert sub-Nyquist sampling theories and algorithms into a hardware implementation of signal acquisition systems. Because of the gap between theories and actual implementations, more hardware-friendly algorithms and designs are still needed. Among the limited number of signal acquisition architectures, even fewer are implemented into hardware prototypes and verified. Because of imperfections in hardware design, the performance of some prototypes is very limited. Some of the performance of the designs cannot be compared to some off-the-shelf traditional ADCs. Only NUS and MWC have been successfully implemented and tested with multi GHz input signals. However, a tremendous amount of calibration is made to compensate for the system error in MWC, and the design concept of NUS contradicts any motivation to design a signal acquisition system that can go beyond the ADC sampling rate. Innovative, scalable, and low-cost algorithms and hardware designs are needed. In the next chapter, a low-cost hardware architecture is proposed based on an asynchronous multirate sampling scheme and associated algorithms. Unlike previous multi-rate work, the designed algorithm makes the hardware scalable from one channel to multiple channels with minimal calibration required. The hardware acquires input signals with different sampling frequencies, and the prototype is built using off-the-shelf electrical components.

1.4 Time Domain Signal Characterization

1.4.1 Traditional Time-Domain Signal Characterization Technique

The best way to capture fast, single-shot transient signals is with digital oscilloscope is to use a real-time scope [58]. The input signals to the real-time scope are branched into parallel channels and sampled by high-rate ADCs. The phases of the ADCs' sampling clocks are properly interleaved with precise and intensive calibration. Therefore, a wideband real-time scope can be very costly.

Another type of scopes, sampling scopes, use equivalent time sampling (ETS), which employs a fixed sampling clock and a swept delay that increases every trigger cycle to capture high-speed signals.

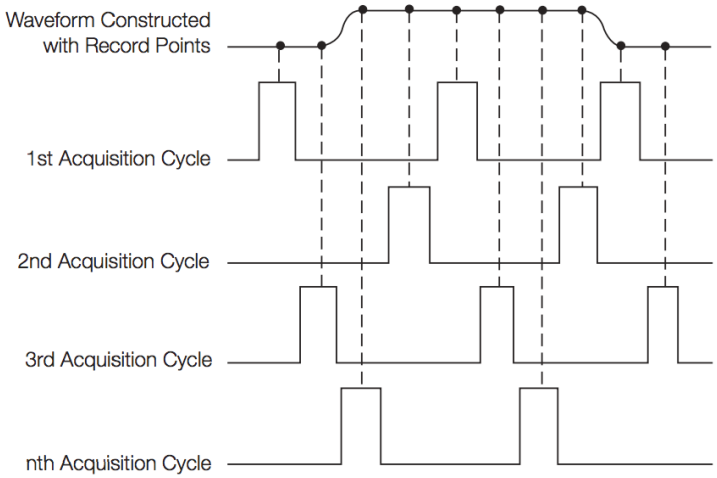

Figure 1.12. Some oscilloscopes use ETS to capture and display repetitive signals. [58]

ETS takes advantage of the fact that most naturally occurring and man-made events are repetitive. ETS constructs a picture of a repetitive signal by capturing a little bit of information from each acquisition, as shown in Figure 1.12. This allows the oscilloscope to accurately capture signals whose frequency components are much higher than the

sampling scopes' sampling rate. Samples acquired at each trigger signal are folded back into one trigger signal period to reconstruct periodic waveforms or eye diagrams. However, ETS relies heavily on the precise control of delay, and this makes the cost of the sampling scope high, although still cheaper than real-time scopes. Another drawback of sampling scopes is that the trigger signal must be clean for unbiased waveform reconstruction.

Incoherent undersampling (IUS) techniques utilize simple acquisition schemes using external unsynchronized clocks and back-end DSP to estimate the fundamental period and to reconstruct signal waveforms. Once the fundamental period is estimated, the samples can be folded back into the fundamental period and form the waveform [60-64]. One major benefit of IUS is that synchronization between the input signal and the sampling clock is not needed. The clock domain of the input signal and that of the ADC can be different. Clean measurement clocks can be provided to the ADC by the high-end clock generation equipment.

1.4.2 Extend the Bandwidth of Oscilloscopes

Band-interleaved schemes have been used to extend the bandwidth of wireless systems. However, characterizing the time-domain waveform requires precise calibration across the whole input bandwidth to preserve the signal fidelity. Compared to interleaving parallel ADCs, the cost for band-interleaved time-domain reconstruction is much higher than it was in the past. However, as data rates keep increasing, designers are now turning to the band-interleaved scheme to extend the bandwidth, but this comes at the cost of more required effort for calibration and more back-end signal processing. In [59], the digital band interleaving (DBI) oscilloscope is proposed, as shown in Figure

1.13. The asynchronous time interleaving (ATI) scheme was later proposed in [2], the advantage of which is that mixers are used in all of the paths such that the each signal path is matched. An ATI block diagram is shown in Figure 1.14. In both systems, intensive calibration and signal processing algorithms for signal compensation and combination in software are key enabling factors.

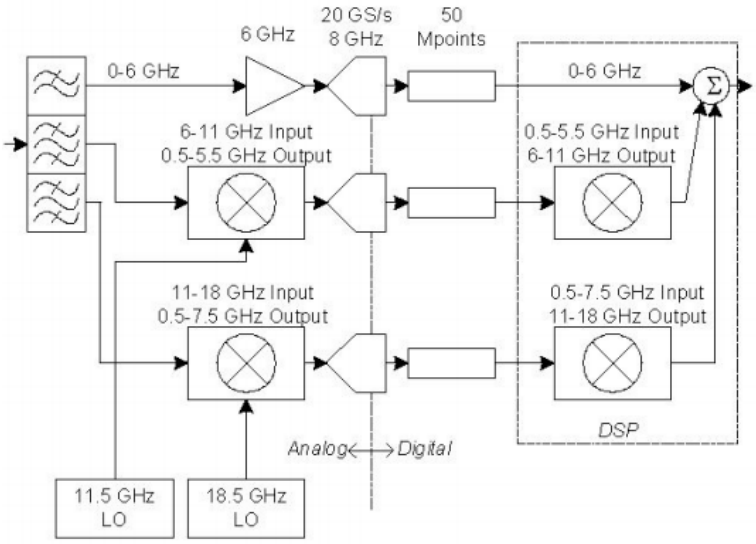

Figure 1.13. Band-interleaved real-time sampling [59]

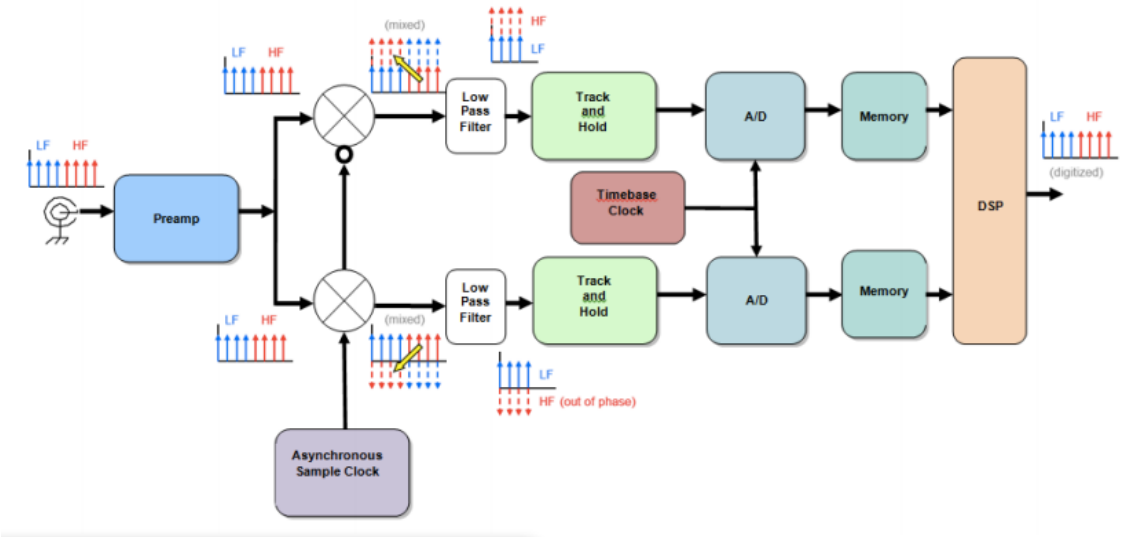

Figure 1.14. Asynchronous Time Sampling [104]

1.4.3 Challenges

In DBI or ATI, mixers are used to down-convert the high-frequency components to a lower-band such that ADCs with a lower sampling rate can be used to acquire the signal without losing any information. These systems require complicated synchronization mechanisms, which significantly increase system complexity, which is one major contribution to the total cost. Oscilloscopes using these sampling schemes are all considered to be high-end oscilloscopes, and their price can easily go up to several hundred thousand dollars, which becomes a barrier of high-speed system designs and research development in academia.

1.5 Jitter Characterization and Measurement for High-Speed Signals

1.5.1 Jitter Analysis

Jitter measurement is an essential part of testing and characterizing high-speed digital I/O and clock distribution networks. Precise jitter characterization of signals at critical internal nodes provides valuable information for hardware fault diagnosis and next generation design. One scheme of jitter classification is shown in Figure 1.15.

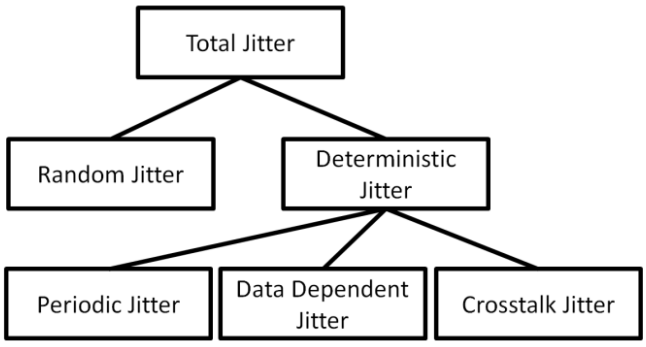

Figure 1.15. Jitter classification scheme

Jitter can be classified into two categories: random jitter (RJ) and deterministic jitter (DJ), which are also referred to as non-systematic and systematic jitter, respectively. Random jitter, caused by device noises (e.g., thermal noise and flicker noise), is unpredictable electronic timing noise. The distribution of RJ can be divided into Gaussian and non-Gaussian distributions [65]. Deterministic jitter is due to non-Gaussian events and has specific causes. It can be further categorized into periodic jitter (PJ), data-dependent jitter (DDJ), and bounded uncorrelated jitter (BUJ), also known as crosstalk jitter (CJ). Periodic jitter can be caused by multiple mechanisms. For example, power supply switching noise could couple to data or clock signal lines through the power supply network and cause periodic jitter. Data dependent jitter can be further categorized into duty cycle distortion (DCD), which is caused by asymmetry in rise time and fall time, and inter-symbol interference (ISI), which is caused by bandwidth limitation of the channel or electromagnetic reflection of the signal. In some PCB trace layouts, such as meander delay lines, ISI can also be caused by self-coupling [67]. Crosstalk jitter, also called bounded uncorrelated jitter, is caused by signals from channels (aggressors) coupling into another channel (victim). It is bounded because of the finite range coupling effect. It is uncorrelated because there is no correlation between the signal transitions of physically close links [68]. The amount of crosstalk jitter depends on aggressor the data patterns, signal power, and coupling mechanisms between the aggressor and victim channel. As the speed of data links increases, the signal with the shorter rise/fall time contains more high frequency components, which could easily leak into other leaks. This effect causes crosstalk jitter and reduces the timing margin in the high-speed link and I/O design. In recent years, the development of SoC technology has put more high-speed

channels in ever-closer proximity. In addition, to achieve an incrementally greater data rate, the emerging technologies pack more serial lanes that operate in parallel. Every channel becomes both an aggressor and a victim. Crosstalk is exacerbated by pre-emphasis and de-emphasis, which enable high-speed serial data receivers to reach a low BER (bit-error rate), even when signals are so degraded that their eye diagrams become closed. At the transmitter, pre-emphasis enhances the high-frequency content of signals, which fends off the low-pass nature of the transmission lane's frequency response. Unfortunately, that high-frequency content generates the most crosstalk. On the receiver side, two of the three standard equalization techniques, CTLE (continuous-time linear equalization) and FFE (feed-forward equalization), amplify crosstalk noise. The third technique, DFE (decision-feed-back equalization), is the only one that doesn't make it worse [69]. As a result, BUJ receives more attention in high-speed data link characterization. In [70], a method is proposed to equalize the crosstalk effect between two adjacent data links.

All different types of jitter might be present together in signals; therefore, there are different algorithms to separate and quantify them. Oscilloscopes are commonly used to visualize signal waveforms and, therefore, for jitter characterization. With a clean reference clock or trigger signals, time interval error (TIE) can be calculated as the deviation in time. TIE takes the form of instantaneous phase variations for each bit period of the waveform captured. In many measurement setups, the transmitter clock is used as the reference clock. In this case, the deterministic jitter embedded in both the transmitter clock and data will be hidden from the TIE measurement. The TIE reflects what the receiver sees from the transmitter, but information is lost from system characterization

perspective. Taking the histogram of the TIE reveals some jitter information, as shown in Figure 1.16, but typically different types of jitter present in the signal simultaneously and make a jitter histogram complicated. TIE compensation for deterministic jitter techniques can help reduce the complexity of a jitter histogram. Further discussion is presented in Chapter 3.

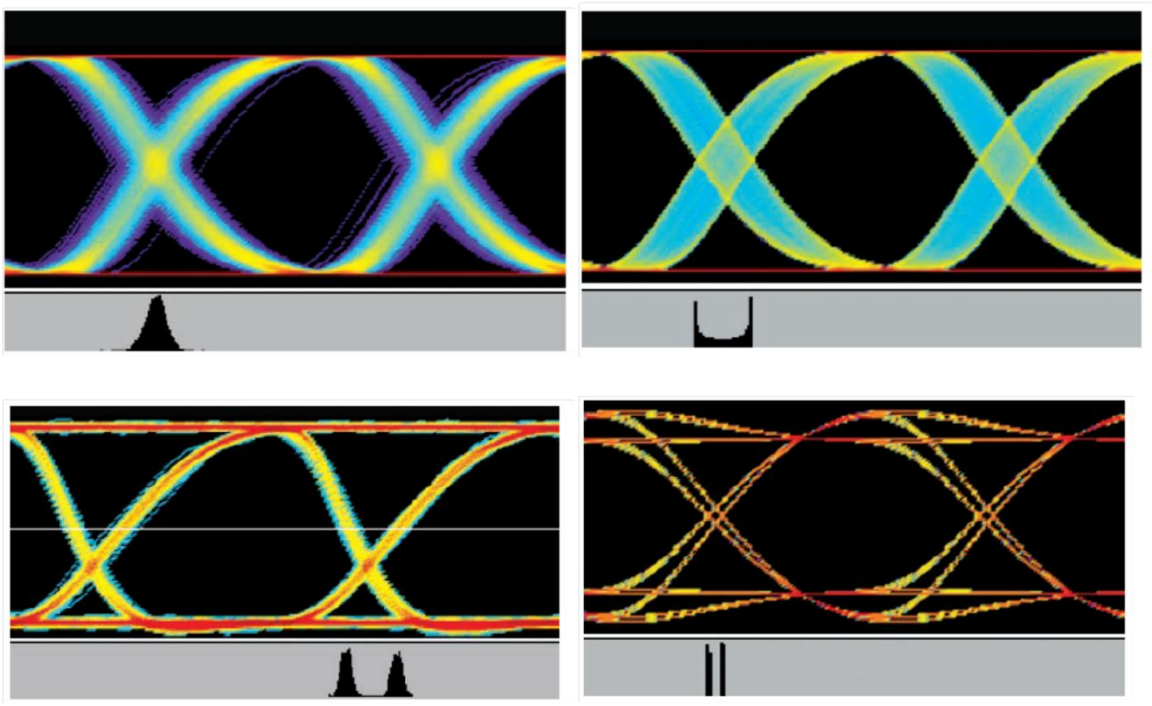

Figure 1.16. Jitter histogram of different types of jitter [72]

RJ (top left), PJ (top right), DCD (bottom left), DDJ (bottom right)

In general, RJ is assumed to be a Gaussian distribution, which is a good approximation for most practical cases. Total jitter includes the deterministic jitter and the random jitter. When multiple types of jitter simultaneously present in the signal, a tail-fitting technique is used to separate RJ and DJ [66]. This technique uses the basic assumption that only the

tails of the jitter distribution are truly Gaussian and unbounded and that all other sources are bounded and deterministic. The attributes of this scheme are shown in Figure 1.17.

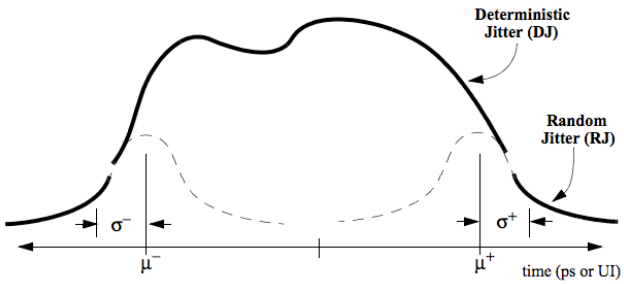

Figure 1.17. Tail-fitting for RJ [73]

Since Gaussian distribution describes RJ, qualitative analysis shows that the tails of a Gaussian distribution extend indefinitely on either side of the mean. Therefore, it is impossible to specify a peak-to-peak jitter range that bounds the jitter 100% of the time. Calculating peak-to-peak jitter is important for jitter budget analysis. It is assumed that any samples that fall outside the peak-to-peak range will cause errors. Therefore, the standard deviation (σ) of the Gaussian distribution in RJ measurement can be converted to the BER of the receiver along with the Q function using the following equation:

$$BER = 2Q\left(\frac{T}{2\sqrt{\sigma^2}}\right)$$

Where Q function is defined as

$$Q(x) = \frac{1}{\sqrt{2\pi}}\int_x^{\infty} \exp\left(-\frac{u^2}{2}\right) du$$

When high-speed links are being characterized, different analytical techniques may yield to different results. The actual signal quality may be very different at the low population levels from the appearance at high populations as seen in a typical waveform eye diagram from an oscilloscope. The waveform eyes shown in Figure 1.18 are those

that would result on a sampling oscilloscope from two different jitter distributions that have the same jitter eye opening at the 10^{-12} level.

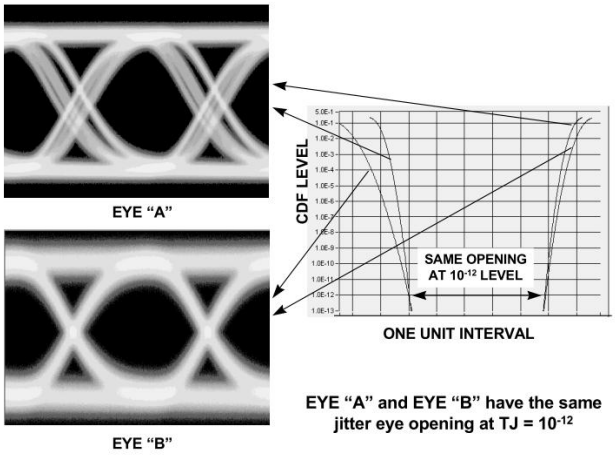

Figure 1.18. Inconsistency between eye diagram and BER [73]

The distributions are taken at the nominal switching threshold level of the signals. Notice that EYE "A" seems to be considerably worse than EYE "B" but is actually equivalent in terms of its total jitter. Therefore, jitter decomposition is needed for more precise signal integrity analysis.

The previously mentioned techniques tend to characterize the jitter in the time-domain. Jitter can also be characterized in a spectrum analyzer. Periodic jitter can be seen as two small tones right next to the clock tone on the spectrum. There is a limitation to using a spectrum of signals to separate and analyze jitter. Therefore, instead, here it is proposed that the jitter spectrum method be used [71]. A jitter spectrum is obtained by taking the FFT of the TIE. An example of a jitter spectrum is shown in Figure 1.19. As can be seen from Figure 1.19, different types of jitter can be observed, and certain types of jitter, such as DDJ and PJ, cause tones in the jitter spectrum and make them easier to

observe. However, BUJ and RJ present as the “noise floor” in the jitter spectrum and make characterization difficult.

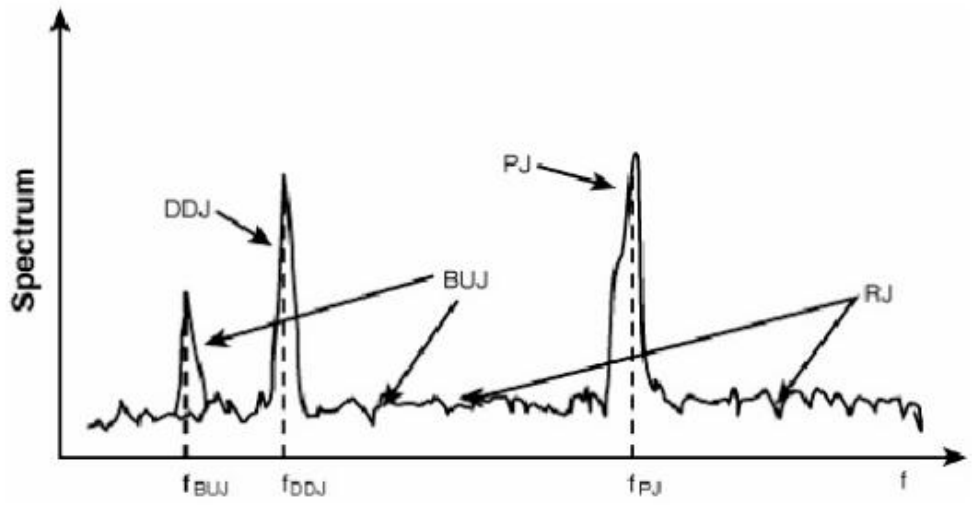

Figure 1.19. Example of a jitter spectrum [74]

One critical type of jitter is crosstalk jitter (CJ). In the previously mentioned methods of jitter characterization, CJ appears to be a difficult type of jitter to characterize. One main reason is that it is random pulse-like noise superimposed on the victim signal. From a histogram of TIE, it is hard to distinguish CJ from DDJ. From a jitter spectrum, the randomness makes the jitter spectrum of CJ a wideband spectrum, which is similar to the spectrum of RJ. CJ is caused by the coupling of physically adjacent links or coupling noise from other active links through shared power or a ground plane. As the data rate and the number of parallelized links increase, crosstalk jitter becomes more noticeable in high-speed systems. In recent years, the development of SoC technology has put more components in ever-closer proximity. In the worst case, the coupling hardware section can make the impulse of CJ out of phase with the victim

signal. This shrinks the eye margin in the vertical (voltage) direction, as shown in Figure 1.20.

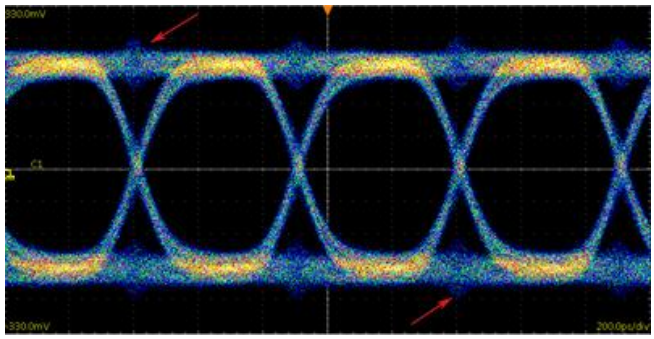

(a)

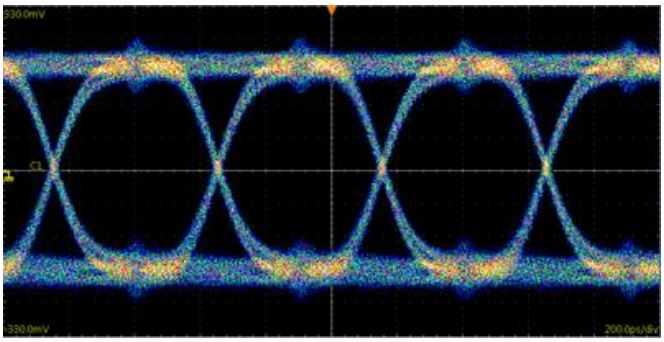

(b)

Figure 1.20. [75] These eye diagrams display the effects of different victim-aggressor phase relationships.

a) The aggressor and victim are in phase, and the crosstalk impairment is at the crossing point (two of these points are highlighted by red arrows).

b) The aggressor and victim are half a bit out of phase, and the crosstalk impairment is at the center of the eye.

A jitter separation comparison table, Figure 1.21, from [74] is another argument supporting the difficulty of BUJ or CJ separation. A time-domain CJ separation method and an associated analysis are discussed in Chapter 3.

Table 6.1. Comparison of the Capability and Performance of Different Jitter Separation Methods

	DDJ	DCD	ISI	PJ	RJ	BUJ
1. Time-domain averaging	Yes: Give the *most accurate DDJ estimation*.	Yes, if rising and falling edges are distinctive.	Yes, if rising and falling edges are distinctive.	No	No	No
2. Frequency-domain Fourier spectrum (FS)	Yes, but may contain PJ if its frequency meets certain conditions.	Yes, if rising and falling edges are distinctive.	Yes, if rising and falling edges are distinctive.	Yes: Magnitude, frequency, and phase are possible, but PJ may be misidentified as DDJ. FFT and interpolation are needed.	Yes: Not accurate, because exact PSD is not possible from FS. FFT and interpolation are needed.	Maybe: Broadband BUJ is difficult to separate from RJ in FS in general, unless it can be controlled.
3. Frequency-domain power spectrum density (PSD)	Yes, if method 1 is used.	Yes, if rising and falling edges are distinctive.	Yes, if rising and falling edges are distinctive.	Yes: Only magnitude and frequency, not phase, are possible. FFT and interpolation are needed.	Yes: *Most accurate RJ estimation.* FFT and interpolation are needed.	Maybe: Broadband BUJ is difficult to separate from RJ in FS in general, unless it can be controlled.
4. Time-domain variance function	No	No	No	Yes: FFT and interpolation are not needed, only magnitude and frequency, no phase.	Yes: FFT and interpolation are not needed.	Maybe: Broadband BUJ is difficult to separate from RJ in FS in general, unless it can be controlled.

Figure 1.21 Comparison table of different jitter separation methods [74]

1.5.2 Challenge

In high-speed digital system design, various forms of jitter and channel defects degrade the signal integrity and limit the data rate. In almost all cases, different types of jitter present at the same time. This makes analyzing high-speed I/O systems more difficult. Many jitter separation methods have been studied. However, crosstalk jitter separation needs further investigation. In addition, increasing parallel channels in the SoC designs increases the time of characterization and testing, and, thus, drives up the total cost.

CHAPTER 2

LOW-COST SPARSE MULTIBAND SIGNAL CHARACTERIZATION USING ASYNCHRONOUS MULTI-RATE SAMPLING: ALGORITHMS AND HARDWARE

To transfer data at higher data rates, RF and digital signals are pushed to operate across wider bandwidths. In many measurement systems, characterizing the spectral content of these wideband signals with ADCs is critical for assessing the performance of the underlying electronics but becomes difficult as well as expensive for multi-GHz signals at Nyquist sampling rates. Signals having sparse representations in the frequency domain can be recovered with sub-Nyquist sampling. Numerous sub-Nyquist sampling schemes have been studied and applied to sparse wideband spectrum characterization. In the past, compressive sensing algorithms have been used to recover signals with fewer samples [30, 27, 76]. The Modulated Wideband Converter (MWC) [44, 54] and Random Demodulation [78, 79, 80] involve mixing wideband input signals with a multi-tone signal containing spectral components across the entire input bandwidth. Mixer non-linearity creates additional tones that reduce the spectrum sparsity and can degrade the reconstruction performance. Mixing with a wideband multi-tone signal generates more intermodulation products and exacerbates the problem. What is needed is extensive calibration of the signal phase and amplitude of the mixer, but this increases the overall cost of the system. Calibration plays even more important roles in synchronous multi-channel systems. For example, MWCs and multi-coset sampling [20, 23, 41, 42] require precise delay synchronization across multiple channels and are susceptible to delay and

sampling frequency variations. Uncertainties in these delays degrade the recovery performance of the associated algorithms [45]. Other algorithms have been proposed to compensate timing mismatches, but these substantially increase the complexity of the receiver [46, 47]. Non-uniform sampling [49] and random sampling [77, 48] are techniques that use a custom designed ADC to collect fewer samples for signal reconstruction. However, they cannot operate beyond the maximum sampling rate of the designed ADCs, which limits the usability of the method for high-frequency signals. In [55-57, 82-85], algorithms and hardware for acquiring signals using optical modulation and constant rate sampling are described. The proposed hardware has the effect of multi-rate sampling but is difficult to implement at low cost.

This chapter introduces a low-cost asynchronous multi-rate sub-Nyquist sampling framework and characterizes signals that have a sparse spectrum. Multi-rate sampling can be subcategorized into asynchronous and synchronous multi-rate sampling. Compared to synchronous sampling, asynchronous multi-rate sampling does not require phase synchronization of different channels, which relaxes the associated hardware design cost and reduces the calibration effort. The designed system is scalable in the sense that it can be implemented with a single channel or with multiple channels. In addition to the hardware design, associated algorithms are proposed to deal with the discrete spectrum and spectral grid mismatch. The Fast-Fourier Transform (FFT) is commonly used to convert time-domain samples into a vector in the frequency domain. However, when different sampling frequencies are used, the spectral grids of the vectors are not aligned, which makes it difficult to compare spectra from different sample sets, which correspond to a different sampling rate. A hardware prototype is built with all off-the-shelf electrical

components, and measurements are taken to verify the architecture and algorithms proposed in this work. This chapter is organized as follows: Section 2.1 addresses the proposed spectrum sensing algorithms. Section 2.2 proposes the hardware design of the associated algorithms. Section 2.3 presents the hardware measurement and verification results. Section 2.4 presents a brief conclusion.

2.1 Multi-rate Spectrum Characterization

The designed multi-rate sensing algorithm for wideband spectrum characterization is a two-step approach. The first step is to detect the input active bands, which are defined as the frequency bands containing a significant energy level compared to that of the noise floor. High-resolution estimation of the frequency of active bands is not required in this step; therefore, fewer samples are used to reduce the computational cost. The second step is to characterize the spectra of the detected active bands; thus, more samples are used in this step to achieve higher resolution.

2.1.1 Active Band Detection with Multi-rate sampling

Suppose a signal, band-limited to B, contains two active bands and is undersampled with two different sampling frequencies, F_{S1} and F_{S2}, as shown in Figure 2.1. Because the sampling frequencies are different, each sample set has a different aliasing spectrum. By concatenating and comparing the aliasing spectra, one can determine the location of the active bands. The proposed active band detection algorithm is based on the concept of spectra comparison.

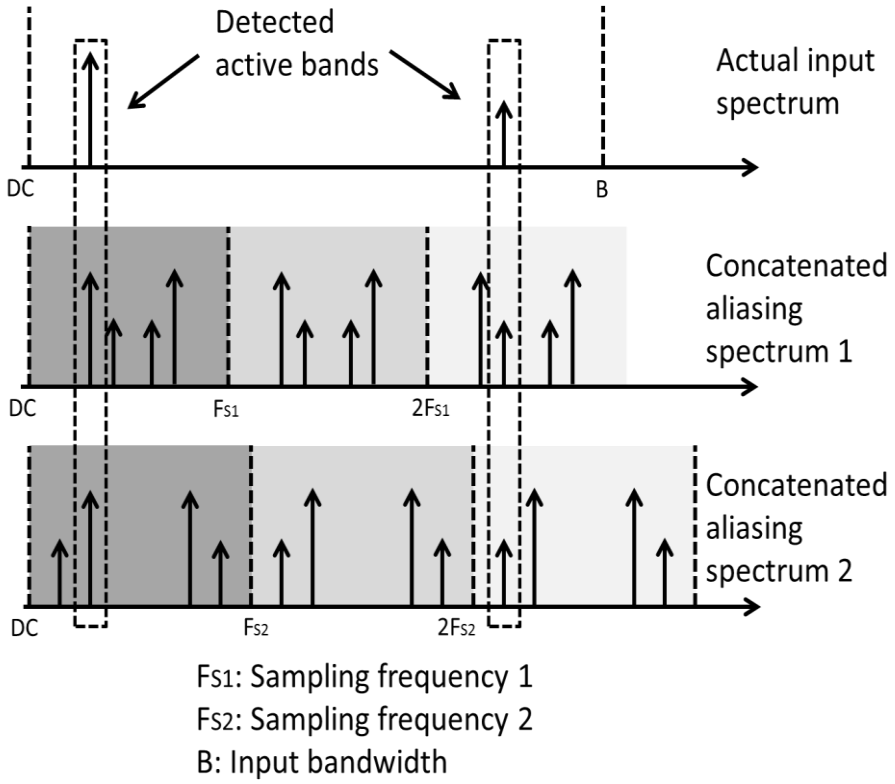

Figure 2.1 Detecting active bands by comparing the aliasing spectra

Since the sampling frequencies are different, one problem immediately found in comparing the spectra is that the spectral grids of the FFT are different. A common frequency grid is needed to compare the aliasing spectra. As shown in Figure 2.2, a signal is sampled with two sampling frequencies F_{S1} and F_{S2}. M samples are collected, and two sample sets, $\overrightarrow{y_1}$ and $\overrightarrow{y_2}$, are formed. The FFT spectral grid spacing for sample sets 1 and 2 are F_{S1}/M and F_{S2}/M, which are not aligned. Forming a common spectral grid requires that the input bandwidth B be divided into N equally spaced spectral grids, which are (then) used to form one sensing matrix for each sample set. The sensing matrices, A_1 and A_2, serve effectively as the Inverse Discrete Fourier Transform (IDFT) matrices. The

aliasing spectra, as shown in Figure 2.1, can be calculated by ${A_1}^H\overrightarrow{y_1}$ and ${A_2}^H\overrightarrow{y_2}$, where H represents the Hermitian transpose.

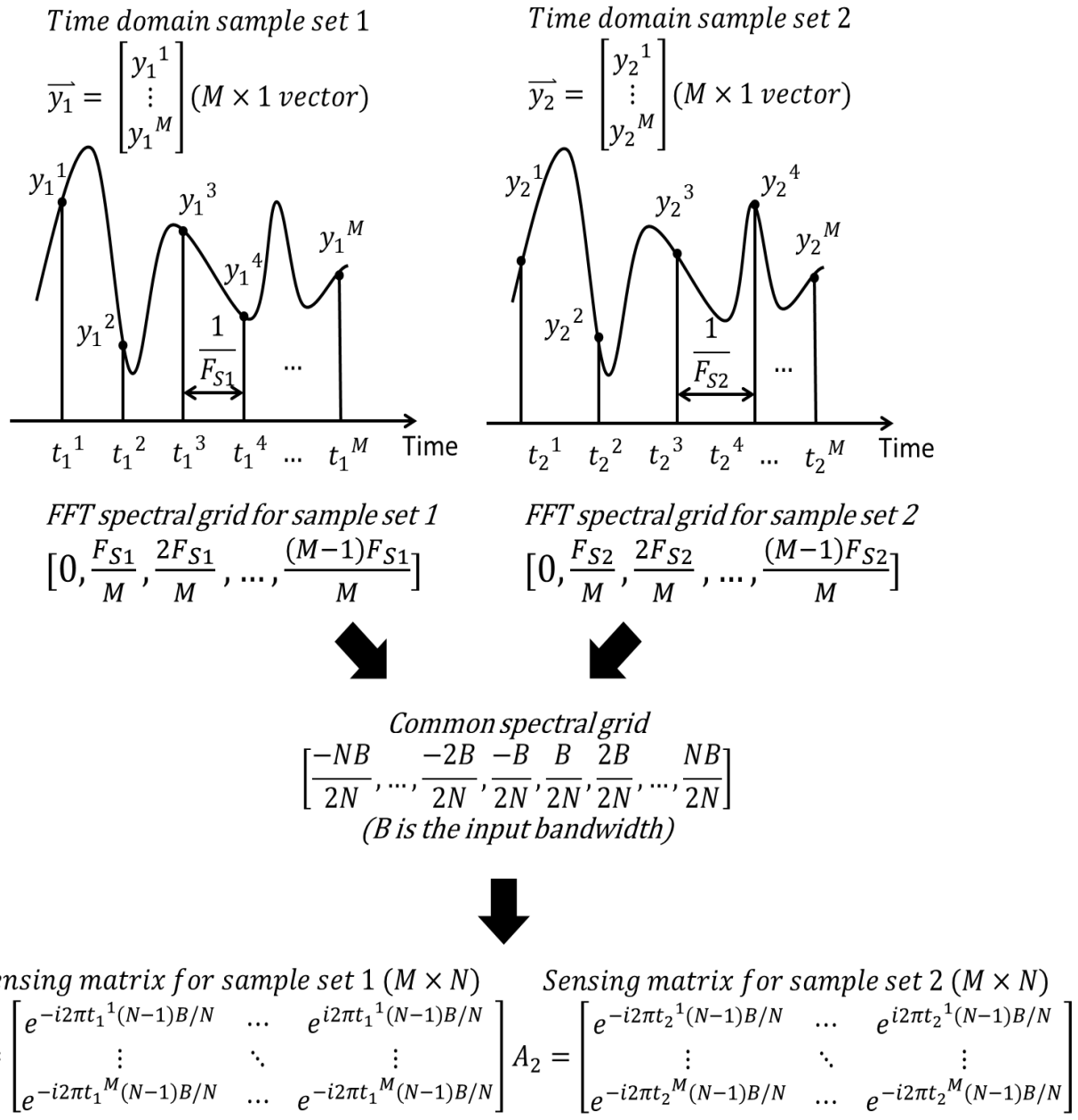

Figure 2.2 Constructing a sensing matrix for each sample set using a common spectral grid (common frequency supports)

The following example is used to illustrate the proposed active band detection algorithm. As in Figure 2.3, a two-tone signal is sampled with two different frequencies. The two aliasing spectra are shown in the first two spectra in Figure 2.4.

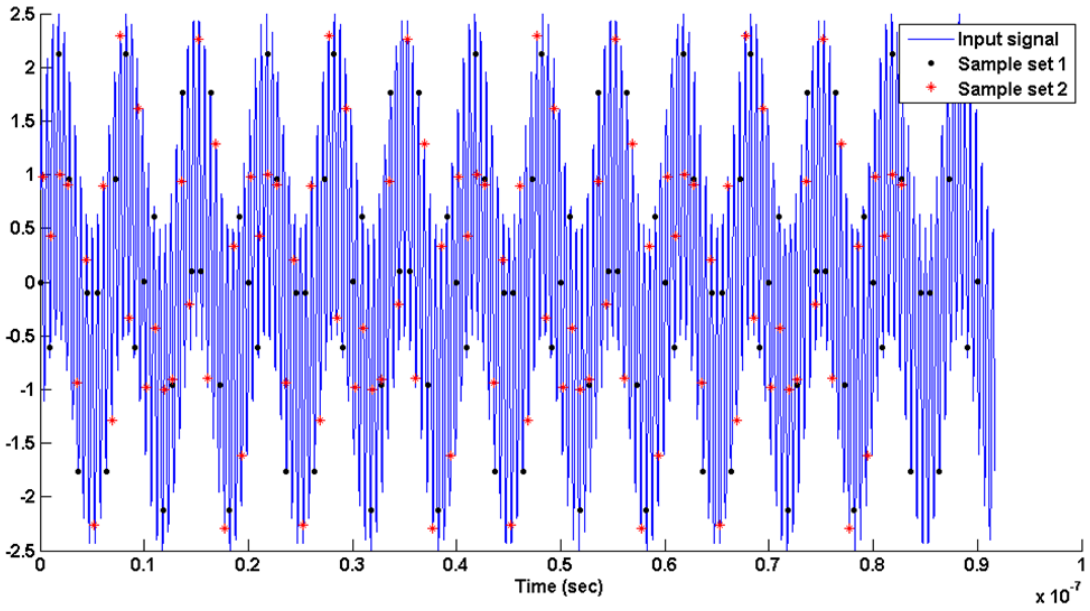

Figure 2.3 Two tone signal sampled with two different sampling frequencies

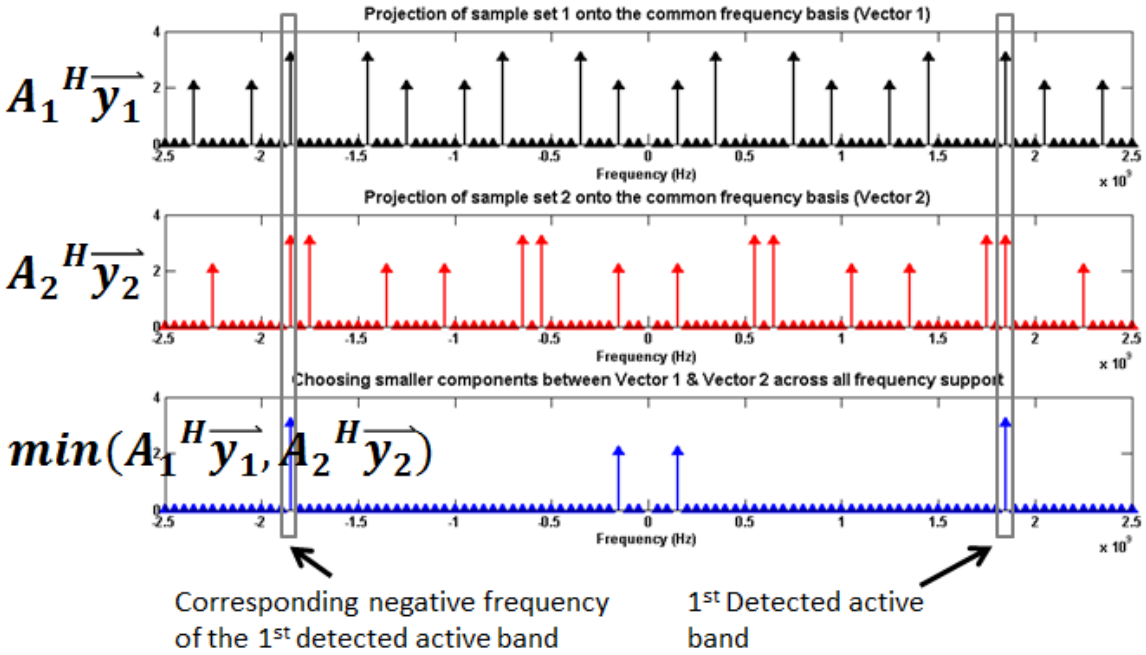

Figure 2.4 Comparing two aliasing spectra to detect the active band (1st iteration)

After the aliasing spectra are compared, the frequency support containing the highest energy level in both spectra can then be chosen to be the first active band. The components at the frequency supports and the corresponding negative frequency of the active bands are then subtracted from the two time domain sample sets. The remaining waveforms are called the residual waveforms, $\overrightarrow{r_1}$ and $\overrightarrow{r_2}$, as shown in Figure 2.5. ${A_1}^H\overrightarrow{r_1}$ and ${A_2}^H\overrightarrow{r_2}$ are then calculated to form the aliasing spectra of the residual waveform, as shown in Figure 2.6. The frequency supports of the second active band can be detected by comparing the spectra. After the component of the second active band is subtracted from the residual waveforms after first iteration, the residual waveform after the second iteration is close to zero, as shown in Figure 2.7.

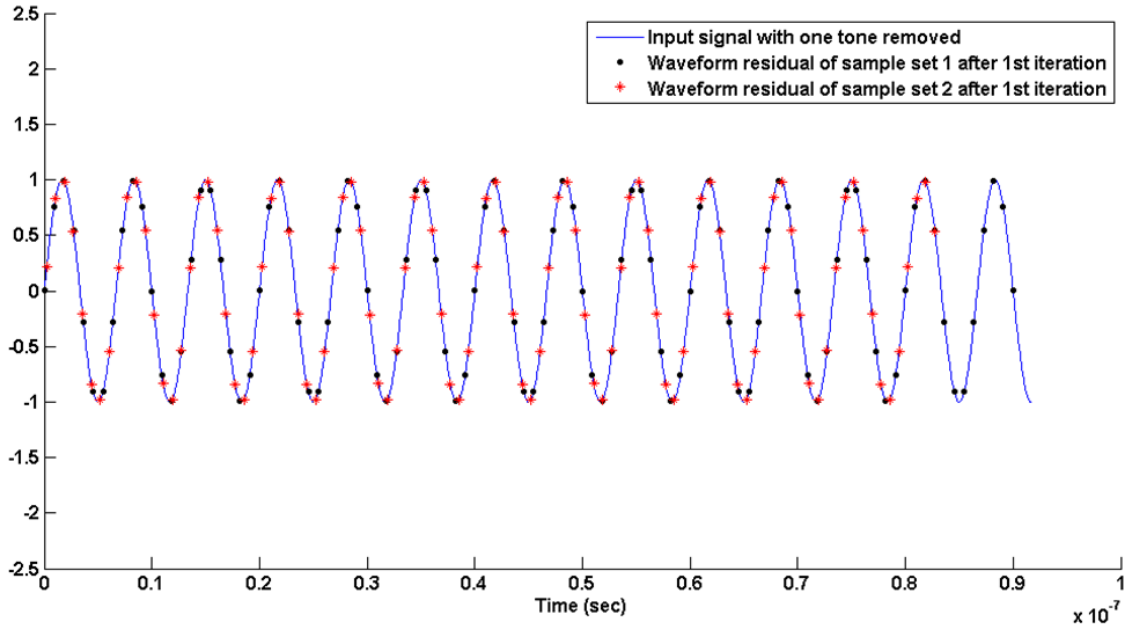

Figure 2.5 Residual waveform after 1st iteration

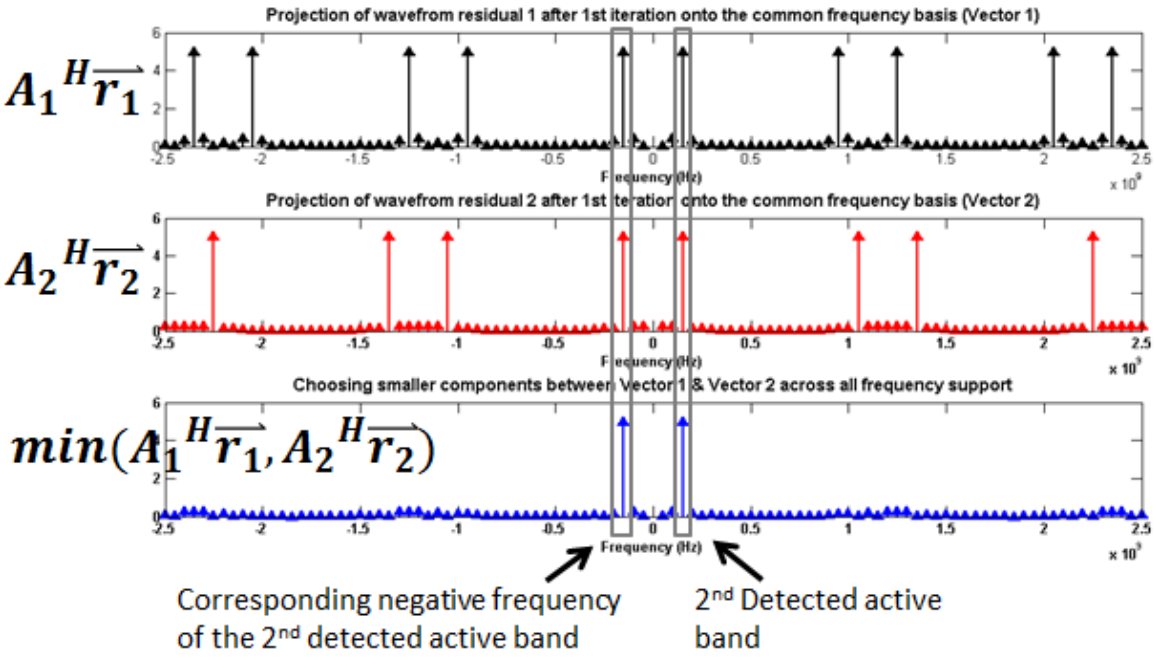

Figure 2.6 Comparing two aliasing spectra to detect the active band (2nd iteration)

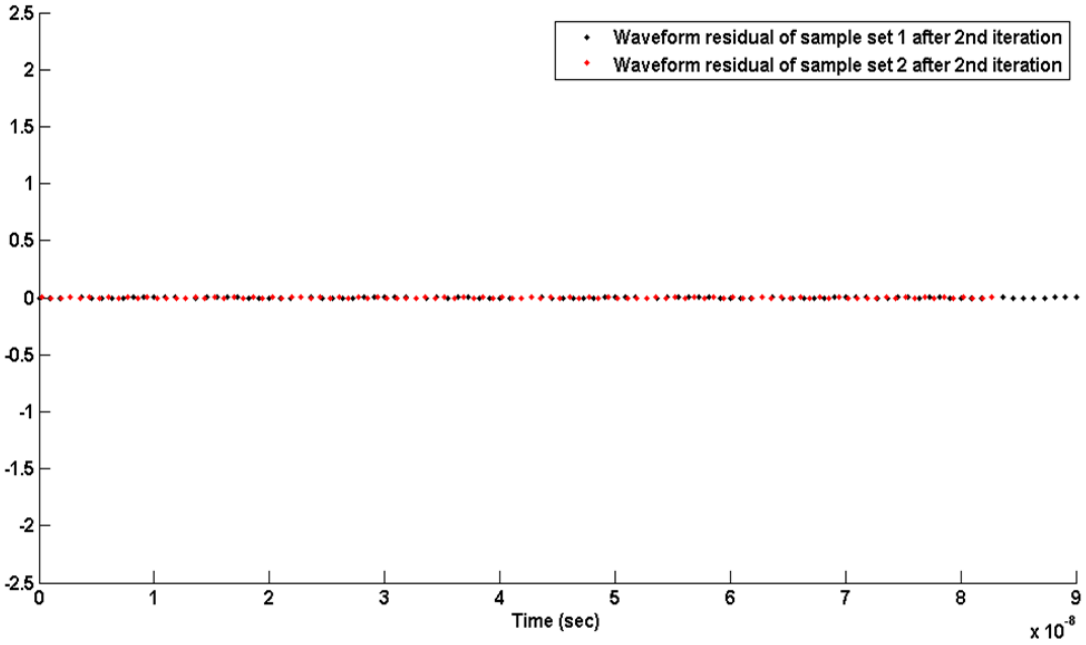

Figure 2.7 Residual waveform after 2nd iteration

The proposed algorithm processes the samples and extracts the active bands iteratively. The stopping criteria of the algorithm is when the iteration reaches the number of the active bands (if the number of active bands is known), or when the energy of the residual waveform is below some pre-defined level.

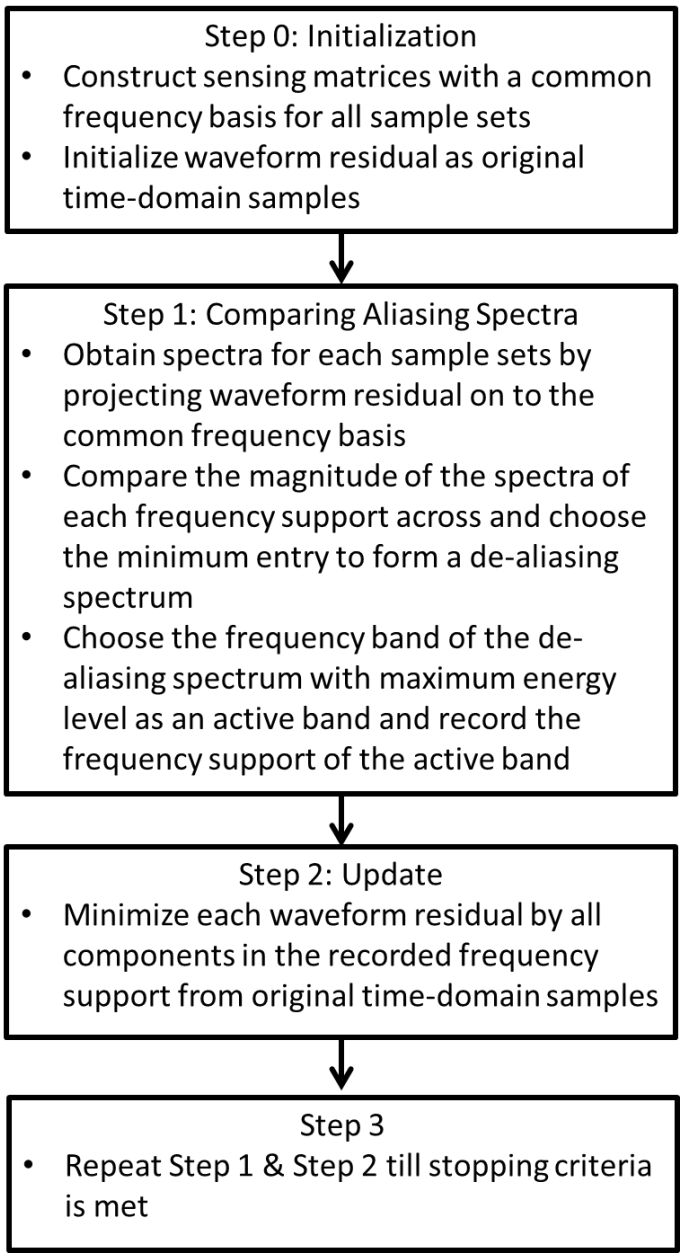

Figure 2.8 Flow chart of the proposed active band detection algorithm

It is important to note that when the active band components are subtracted from the time domain waveform, this is done so for each sample set individually instead of jointly, which makes the relative delays across different channels not needed; therefore, the proposed algorithm becomes an asynchronous algorithm, which reduces the effort needed for calibration and increases the robustness of the system. The proposed algorithm is based on the Orthogonal Matching Pursuit (OMP) algorithm [86]. A flow chart of the proposed active band detection algorithm is shown in Figure 2.8. As can be expected, if two active bands fall onto the same frequency support in the aliasing spectra, the algorithm may fail. Therefore, an analysis is performed in simulation to determine the reconstruction performance in terms of the probability of successful detection of multiple randomly selected active bands. In the previous example, a two-tone signal and two-rate asynchronous sampling are used to explain the proposed algorithm. With the asynchronous scheme, the system can be easily scaled to multi-rate sampling. As more frequencies are used to sample the input signal, more sample sets are acquired. As can be seen from Figures 2.9 (a) to Figure 2.9 (c), as the number of sample sets is increased from 2 to 5, the number of successful detections in 100 runs increases. The other parameter in Figure 2.9 is the input bandwidth. The proposed method relies on comparing the aliasing spectra. As the input bandwidth gets wider, it is necessary to extending the aliasing spectra to cover the entire input bandwidth, which, thus, increases the probability of wrong detection. Therefore, the number of successful detections decreases, as shown in Figure 2.9. The other parameter that affects the performance of reconstruction is the number of samples used in the detection. The number of samples used is related to the resolution of the spectra. Spectra with higher resolution give better reconstruction

performance. As can be seen in Figure 2.10, the number of successful detections can be increased at the cost of increasing computation.

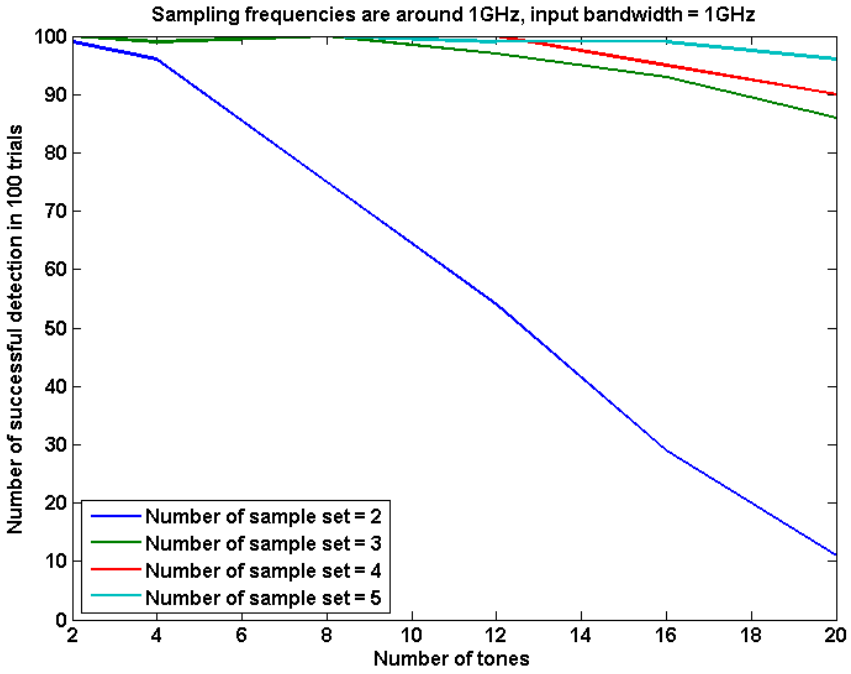

Figure 2.9 (a) Reconstruction performance with 1GHz input bandwidth

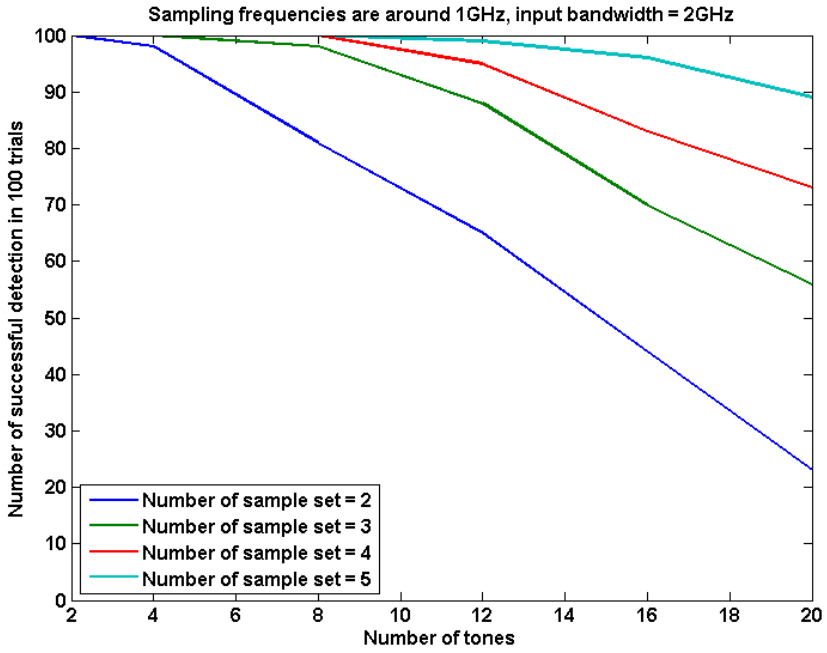

Figure 2.9 (b) Reconstruction performance with 2GHz input bandwidth

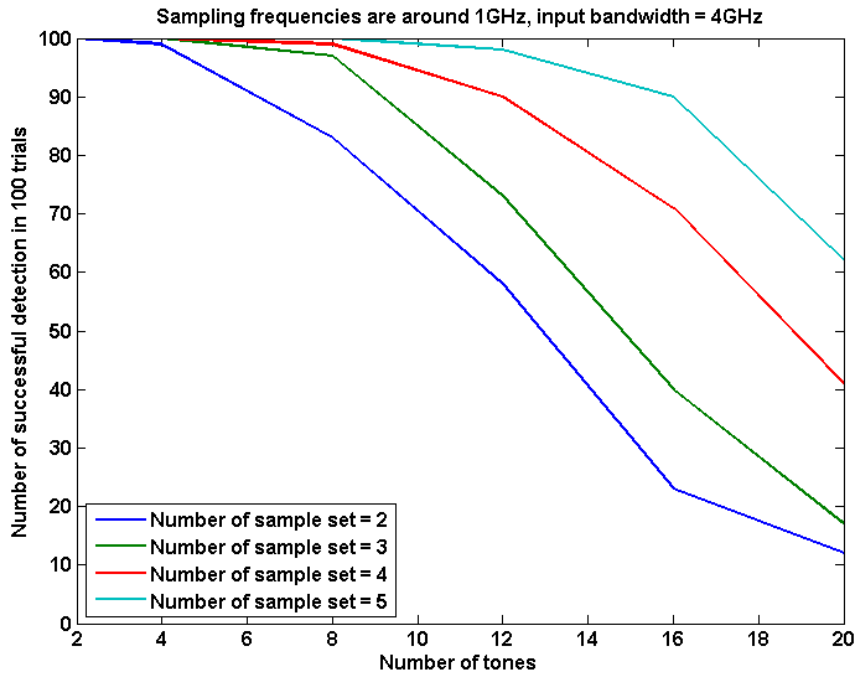

Figure 2.9 (c) Reconstruction performance with 4GHz input bandwidth

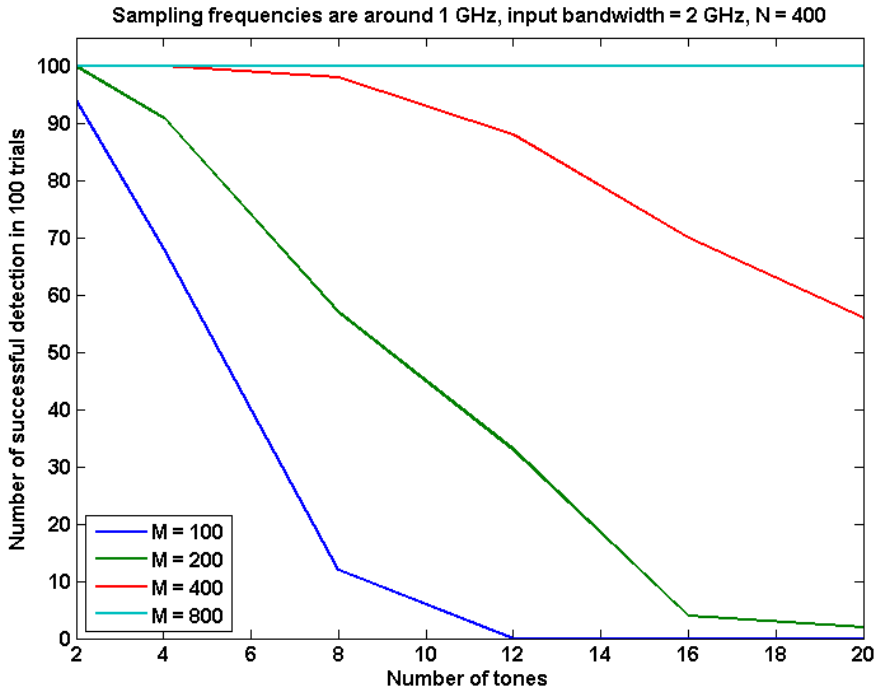

Figure 2.10 The number of success detection increases as the number of samples used in active band detection increases.

2.1.2 Active Band Spectrum Characterization

In the previous section, only relatively fewer samples, typically a few hundred samples are used for detecting active bands. However, spectral resolution is directly related to the number of samples used for characterization; therefore, in the spectrum characterization step, all the acquired samples are used. Since in the proposed algorithm, only the frequency supports around the active bands are characterized, the computational cost is not as high.

Even with correct detection of the frequency supports of the active bands, overlapping of active bands might occur in some sample sets. Therefore, an algorithm is needed to select only one sample set for the characterization of each detected active band. The proposed spectrum characterization algorithm will be explained with the following example. Suppose three 30-MHz bandwidth channels are chosen randomly from the 5GHz band to form the input signal. In this simulation, the randomly chosen center frequencies of each active channel are 2.643 GHz, 0.843 GHz, and 0.997 GHz. The input signal is acquired with 4 different sample frequencies, and the average sampling rate is around 1Gsps. The aliased spectrum is shown in Figure 2.11. 400 samples and the algorithm proposed in the last section are used to detect the frequency supports of the three active bands. Figure 2.12 shows the mean-subtracted and normalized spectra of each sample set around the frequency supports of the first detected active band, which has a center frequency at 0.843 GHz. As can be seen, the spectra of sample sets 1 and 2 have multiple active bands overlapping, while sample sets 3 and 4 have the correct spectra. Cross-correlation of the spectra of different sample sets is used to identify the correct spectra. The correct spectra will have higher correlation, while the spectra with

multiple active bands overlapping will have different shapes and lower correlation with all the other spectra. Therefore, the two sample sets with highest spectra cross-correlation are chosen as the correct sample sets to use for characterization.

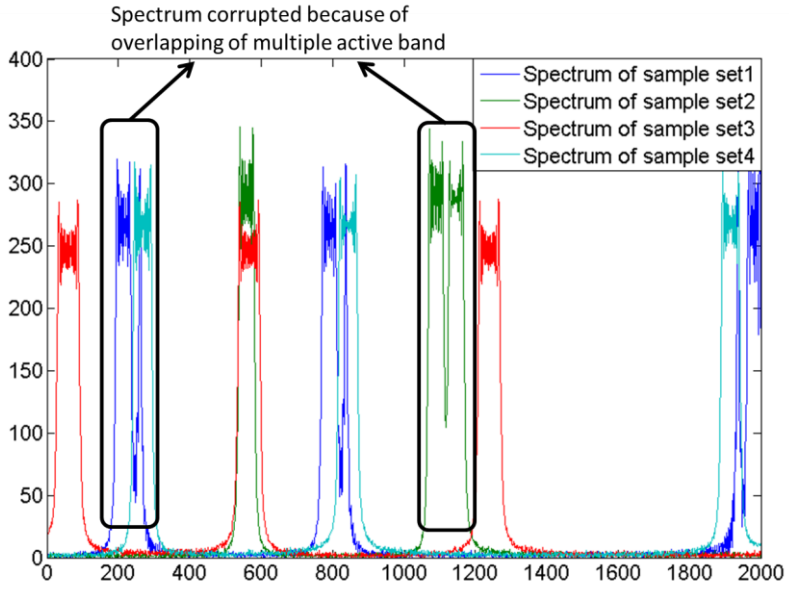

Figure 2.11. Aliased spectrum of 4 different sampling sets.

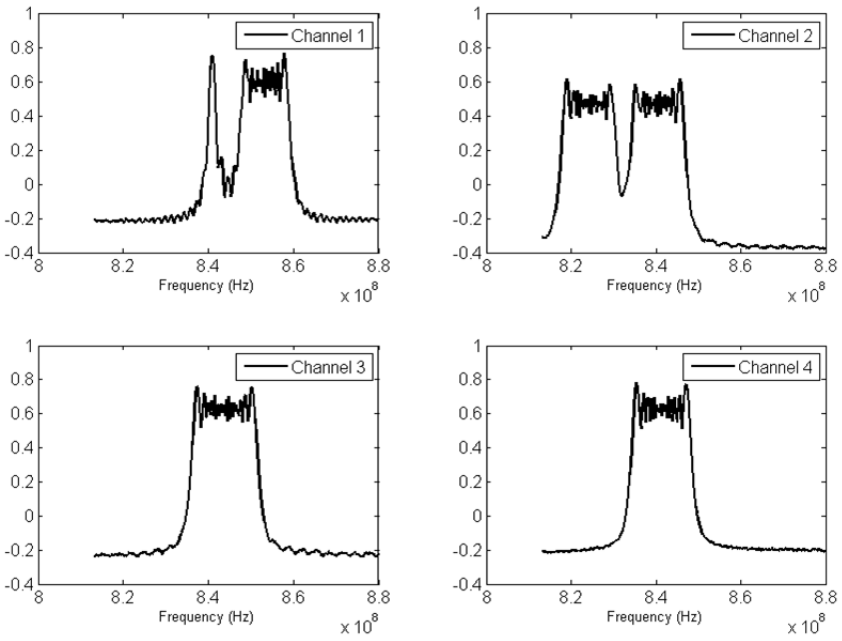

Figure 2.12. Aliasing Spectra of different sets for the first active band

Table 1 shows the cross-correlation of the spectra of the first active band. Samples 3 and 4 have the highest cross-correlation, as shown in the colored box. Further choosing one sample set between sample set 3 and 4, requires that total variation (TV) be used as a metric [102] to choose the smoother spectrum for characterization. The total variation of the spectrum of each sample set is shown in Table 2. Between sample sets 3 and 4, sample set 3 has the smoother spectrum, and thus, the smaller total variation. Choosing the metric is a design choice. For example, in [55], the total energy of the frequency supports is used as the metric. Once a sample set is identified, instead of the common frequency grid, an orthogonal spectral basis, corresponding to the sampling frequency can be used to reconstruct the spectrum of the active band. For each active band, the same method is used to identify two correct spectra and choose the one with a total variation metric for characterization. The spectra reconstructions of different active bands are shown in Figure 2.13.

Active band 1	Sample set 1	Sample set 2	Sample set 3	Sample set 4
Sample set 1	X	-5.65	13.65	6.20
Sample set 2	-5.65	X	13.37	18.01
Sample set 3	13.65	13.37	X	25.58
Sample set 4	6.20	18.01	25.58	X

Table 2.1. Spectrum Correlation Matrix of the first active band in Figure 2.12

Active band 1	Sample set 1	Sample set 2	Sample set 3	Sample set 4
TV	8.3640	8.8831	6.0089	5.8462

Table 2.2. Total variation of spectrum feature of active band 1 in Figure 2.12

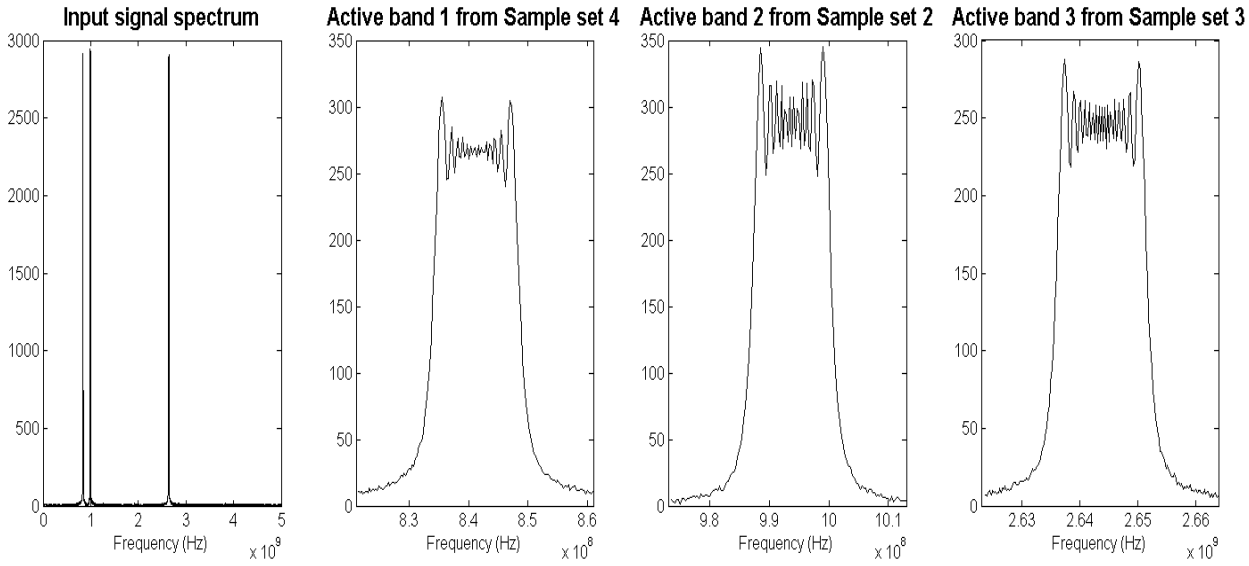

Figure 2.13. The Input signal (Left), which contains 3 active bands, and 3 corresponding recovered active bands

2.2 Hardware Architecture Design

2.2.1 Hardware Design

The hardware design goal is to develop a low-cost, low-complexity, and scalable design to support the proposed multi-rate algorithms. The options of sampling frequencies are given by the programmable fractional frequency synthesizers. As shown in Figure 2.14, a single multi-rate sampling module is capable of obtaining samples collected with different sampling frequencies. The single module can be scaled to multiple modules, as in Figure 2.15 using less signal acquisition time. The programmable frequency synthesizers in a multiple-module scheme can be different in order to increase the diversity of the sampling rates. The input signal is divided and fed into the wideband track-and-hold (T/H) amplifiers and digitized by identical analog-to-digital converters

(ADCs). Since the hardware is intended to subsample wideband signals, the T/H amplifiers must have an input bandwidth that can support the bands to be sensed. The programmable frequency synthesizers in multiple module scheme can be different to increase the diversity of the sampling rates. The input signal is divided into separate input channels and fed into the wideband track-and-hold (T/H) amplifiers and digitized by identical analog-to-digital converters (ADCs). Since the hardware design is intended to subsample wideband signals, the T/H amplifiers must have the input bandwidth that can support the bands to be sensed.

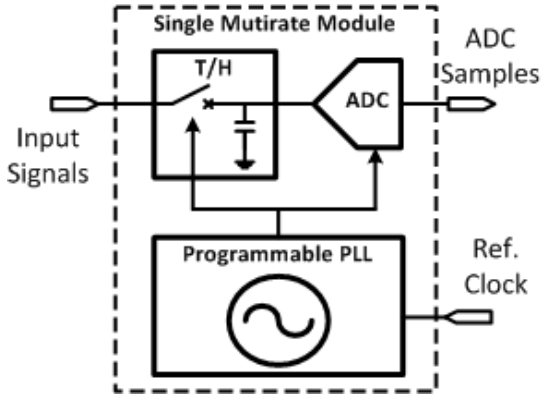

Figure 2.14. Single Multirate Module

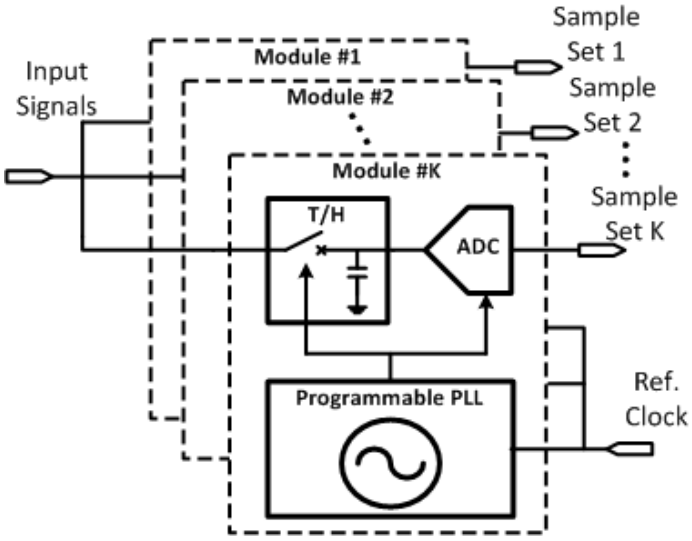

Figure 2.15. Parallel Multirate Module

Multiple sampling frequencies generated by a common clock base, and typically a clean and low-frequency source, are used to be the clock base. The low frequency source is generated and fed into the second level PLLs, which generate different sampling clocks for ADCs and T/H amplifiers. The sampling phase of ADCs relative to the T/H amplifiers should be adjusted such that the data acquisition timing is aligned with the hold phase of the T/H amplifier. The configuration for delay adjustment can be obtained by performing a one-time calibration. The calibration is performed by sending a high-frequency tone as an input signal and sweeping the phase difference between the ADC and the T/H amplifier. The ideal phase difference should be the one with the smallest attenuation. When the frequencies of the sampling clocks are changed, the phase difference should be adjusted. The delay configuration for different sampling frequencies can be obtained by a one-time calibration, and the configuration can be stored and applied when the sampling clock is changed.

2.2.2 Choosing Sampling Frequencies

A very commonly asked question is how to select the sampling frequencies in a multi-rate system. In general, choosing high sampling frequencies can reduce the chance of active band overlapping and increase the algorithm performance. In addition, if one sampling frequency is an integer multiple of another sampling frequency, there will be no benefit. For example, a sample set with a sampling frequency of 500 MHz does not contribute any information if there is already another sample set with a sampling frequency of 1 GHz. Experiments have shown that for similar sampling frequencies, the performance in terms of the recovery success rate does not vary much. In fact, the limitation here comes from the hardware implementation. Current high-end signal

generators can generate single-tone signals accurately up to very high frequencies with good resolution. The signals can serve as clean sampling clocks in multi-rate systems. However, it is not practical for a low-cost programmable PLL to be capable of such performance. In our hardware prototype, TI LMX2541 Frequency Synthesizers are used to generate the sampling clock. The option of generated output frequency depends on the two frequency dividers. Generating frequencies within a similar range (around 1GHz) requires the use of two devices from the LMX2541 family (but with different part numbers) to increase the diversity of options of the sampling frequency. The option of generated output frequency depends on the two frequency dividers, as shown in Figure 2.16, the functional block diagram of the PLL. Generating frequencies within a similar range (around 1GHz) in the later experiment required using the following sampling frequencies: 1.1GHz, 1.2GHz, 1.15GHz, 1.167GHz, 1.2GHz, and 1.25GHz.

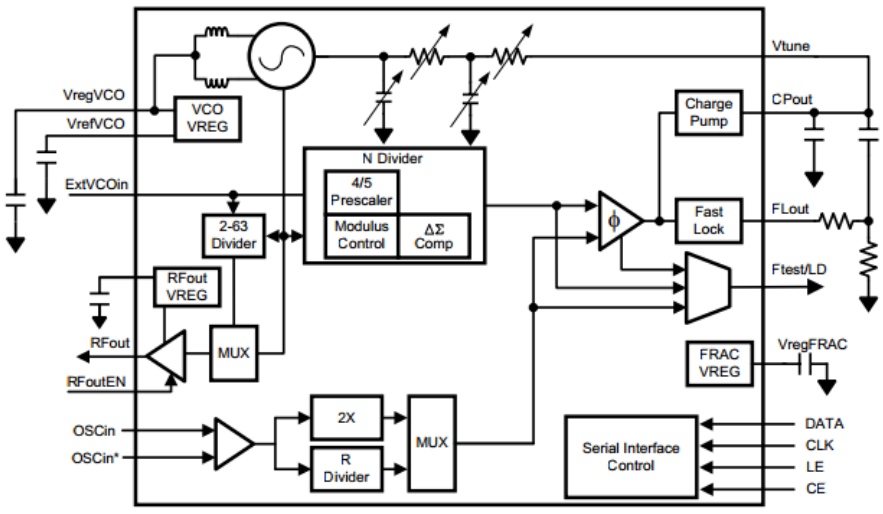

Figure 2.16 LMX2541 PLL functional diagram [88]

2.2.3 Comparison with Other Sub-Nyquist Sampling Schemes

The calibration requirements and system imperfections caused by hardware non-

ideality and variations are reduced in this hardware scheme if it is compared to other sub-Nyquist sampling schemes.. There are two required calibration steps in this work. The first, as with other signal acquisition systems, is to calibrate each channel's path loss. Second is to calibrate the delay calibration between the track-and-hold circuitry and the ADC at different sampling frequencies to ensure the integrity of the sampled signal. A comparison table of the hardware implementation and calibration between this work and other approaches is shown in Table 3. The advantage of the proposed approach is that the effort required for calibration is relatively low compared to the effort required with other synchronous and mixer-based systems. A hardware prototype can be implemented using all off-the-shelf components. Optical components or custom designed circuitry is not needed.

	[54]	[42]	[40]	[49]	This work
Scheme	Modulated wideband converter	Multi-coset sampling (Periodic non-uniform)	Asychrnous Multirate sampling	Non-uniform sampling	Asynchronous multirate sampling
Hardware prototype	All electrical	N/A	Electrical and optical	All-electrical	All electrical
Input bandwidth	2 GHz	N/A	18 GHz	2GHz	18 GHz
Scalability	Low	Low	Low (requires redesigning the optical components)	Low	High
Calibration & Comment	• Gain loss • Phase and amplitude of tones of periodic digital sequence • Low-pass filter characterization • Mixer characterization and calibration • Delay synchronization across different channels	• Gain loss • Delay synchronization across different channels • Delay between T/H and ADC (if T/H is used to increase ADC input bandwidth)	• Gain loss • Optical components are used to modulate and multiplex signals	• Gain loss • Delay between T/H and ADC • Sampling rate limited by ADC sampling rate. (Sampling rate may exceed ADC sampling rate with multi-channel scheme.)	• Gain loss • Delay between T/H and ADC

Table 2.3. Hardware implementation comparison

2.3 Hardware Measurement

A multi-rate system with electrical components is built based on the architecture proposed in Section III to serve as a prototype. Although it is difficult to scale up a synchronous multi-rate system, both synchronous and asynchronous algorithms can run on a synchronous multi-rate sampling scheme. Therefore, a synchronous multi-rate system is built for verification purposes. All the components were purchased off-the-shelf. As shown in Figure 19, input signals branch into two channels and are directly fed to a Hittite 18 GHz wideband track-and-hold amplifier (HMC5640BLC4B) and a Hittite 5 GHz wideband track-and-hold amplifier (HMC5641BLC4B). As mentioned in the previous section, these two track-and-hold amplifiers are used to increase the input bandwidth of ADCs for subsampling purposes. Since the two paths are different, any gain difference between these two paths needs to be compensated with a one-time frequency sweeping calibration. In addition, for an input bandwidth greater than 5 GHz, only the channel with the 18 GHz T/H amplifier can be used. Two ADC12D1800 ADCs are used to digitize signals after the 5 GHz and 18 GHz T/H amplifiers. The samples are then captured with a Xilinx Vertex-6 field programmable gate array for further processing.

Clock generation is critical in a multi-rate system. The system clock is fed to a clock conditioner (LMK04033) to generate a clean low-frequency clock base. Texas Instruments LMX2541 synthesizers use this clock base to further generate the two different clocks for each channel. The track-and-hold and ADC of each channel takes its clock source from one of the two frequency synthesizers to acquire the data. The ADC's internal programmable aperture delay is set so the ADC samples at the hold phase of the track-and-hold amplifier. Since it is a synchronous multi-rate system, additional digital

delay chips are required to adjust the delay between these two channels. Another Xilinx FPGA Spartan-6 is used to program and control all the components, including the ADCs, digital delays, and frequency synthesizers.

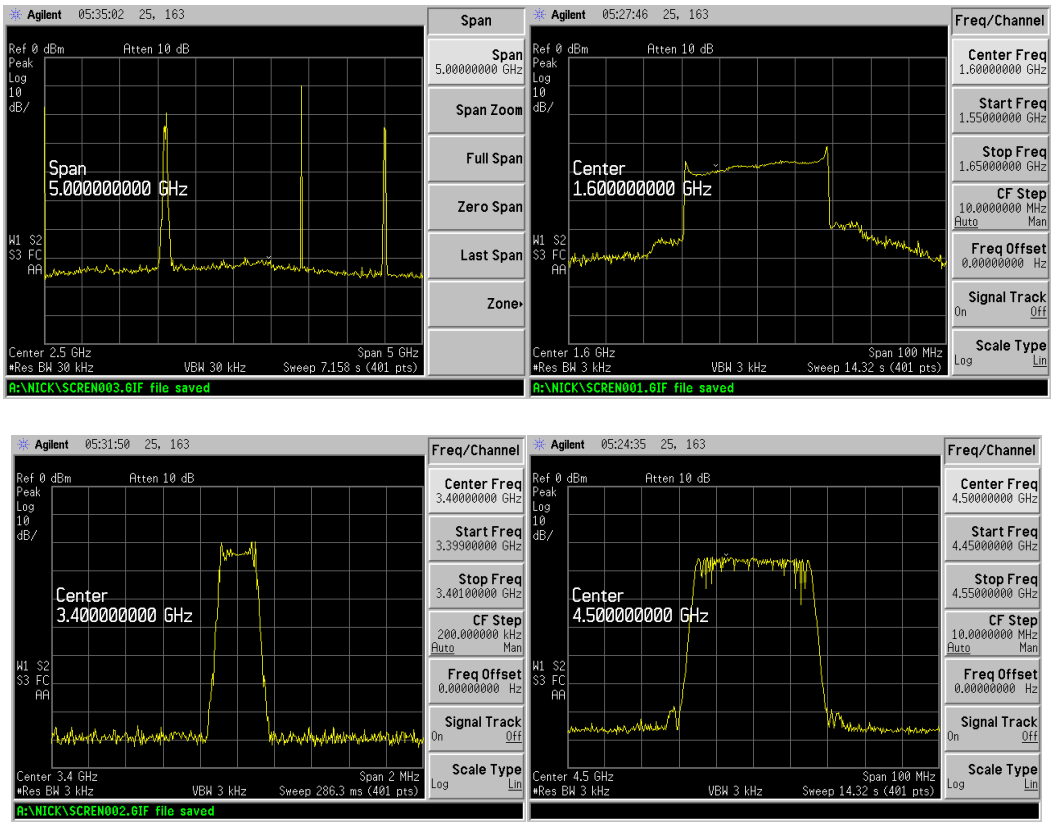

Figure 2.17. The spectrums of the input signal

Agilent E4423B, HP 8648D, and Agilent E8257D signal generators are used to generate three frequency-modulated signals, which are combined as the input to the signal acquisition system. The center frequencies of the three frequency modulated signals are 1.6 GHz, 3.4 GHz, and 4.5 GHz, and the bandwidths are 60 MHz, 4 MHz, and 50 MHz respectively. The signals are then combined and fed into the AMRS system. The overall spectrum and the spectra of these three active bands are shown in Figure 2.17. Four different sampling frequencies (1.15GHz, 1.167GHz, 1.2GHz, and 1.25GHz) are

used to capture the input signal. 16384 samples are acquired. The first 400 samples are used for active band detection. ($M = 400, N = 3000, B = 5\,GHz$) Therefore, the spectral resolution with 400 samples should be around 12.5 MHz. (5 GHz / 400). Since the actual bandwidth is greater (60MHz > 12.5MHz), a window of 60 MHz is used to convolve with the spectra to find the center of the active band in the algorithm. After the active bands have been correctly detected, the correlation matrix and the total variation metric are used to select the most representative spectrum of each active band and to characterize the spectrum. Comparing the spectral shape of the active bands requires higher resolution. Therefore, 16384 samples are used to perform spectrum classification and characterization. The reconstructed spectra are shown in Figure 2.18. Sample set 1 is selected to characterize active band 1 and active band 3. Sample set 2 is selected to characterize sample set 2. Orthogonal Fourier matrices are constructed with the sampling frequency of the selected sample set and used for characterization. Active band 2 has a very narrow bandwidth (2 MHz); apparently, 16384 samples do not provide enough resolution for characterization.

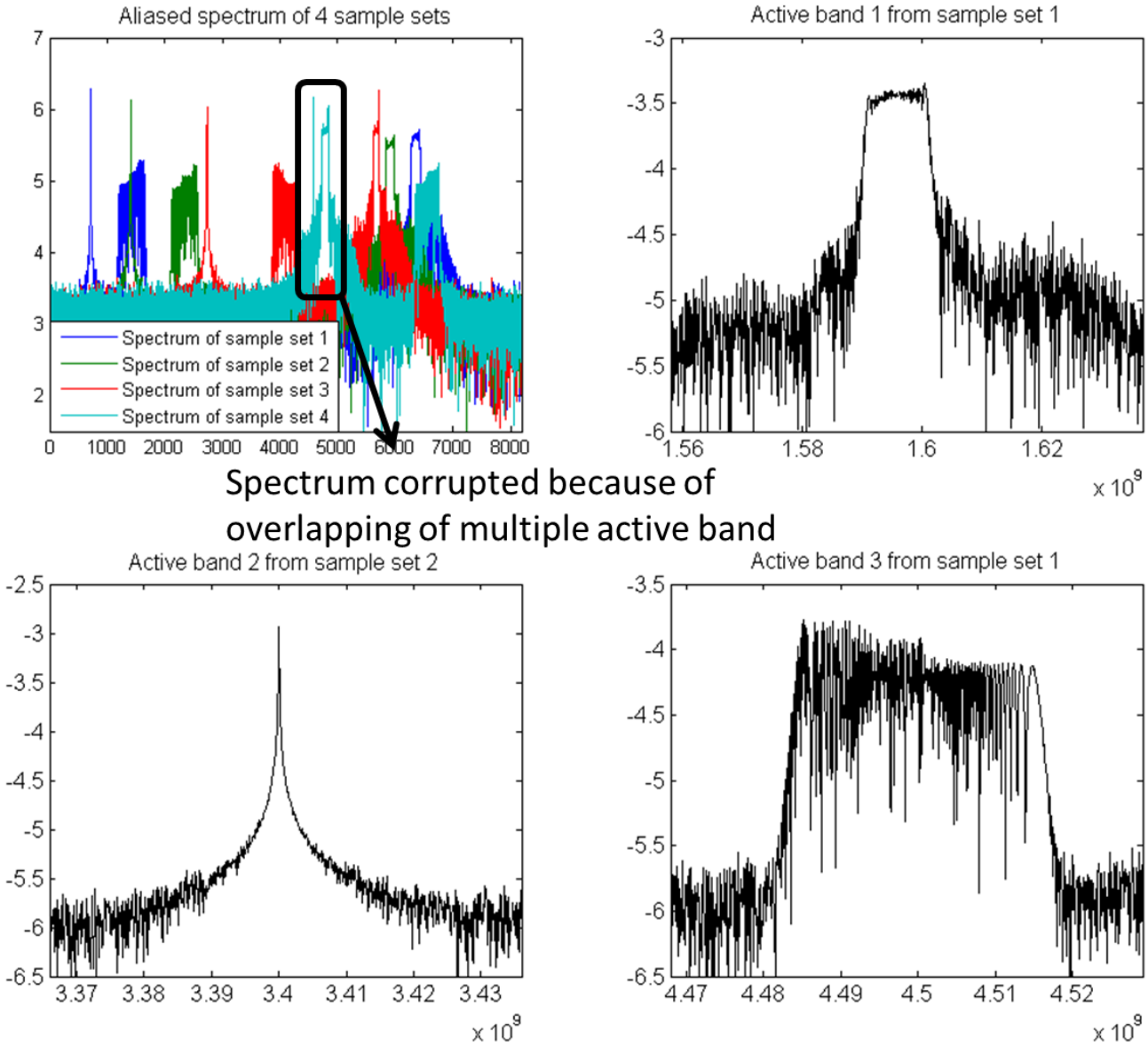

Figure 2.18. Aliased spectrum of 4 different sampling sets (Top left) and the recovered spectrums

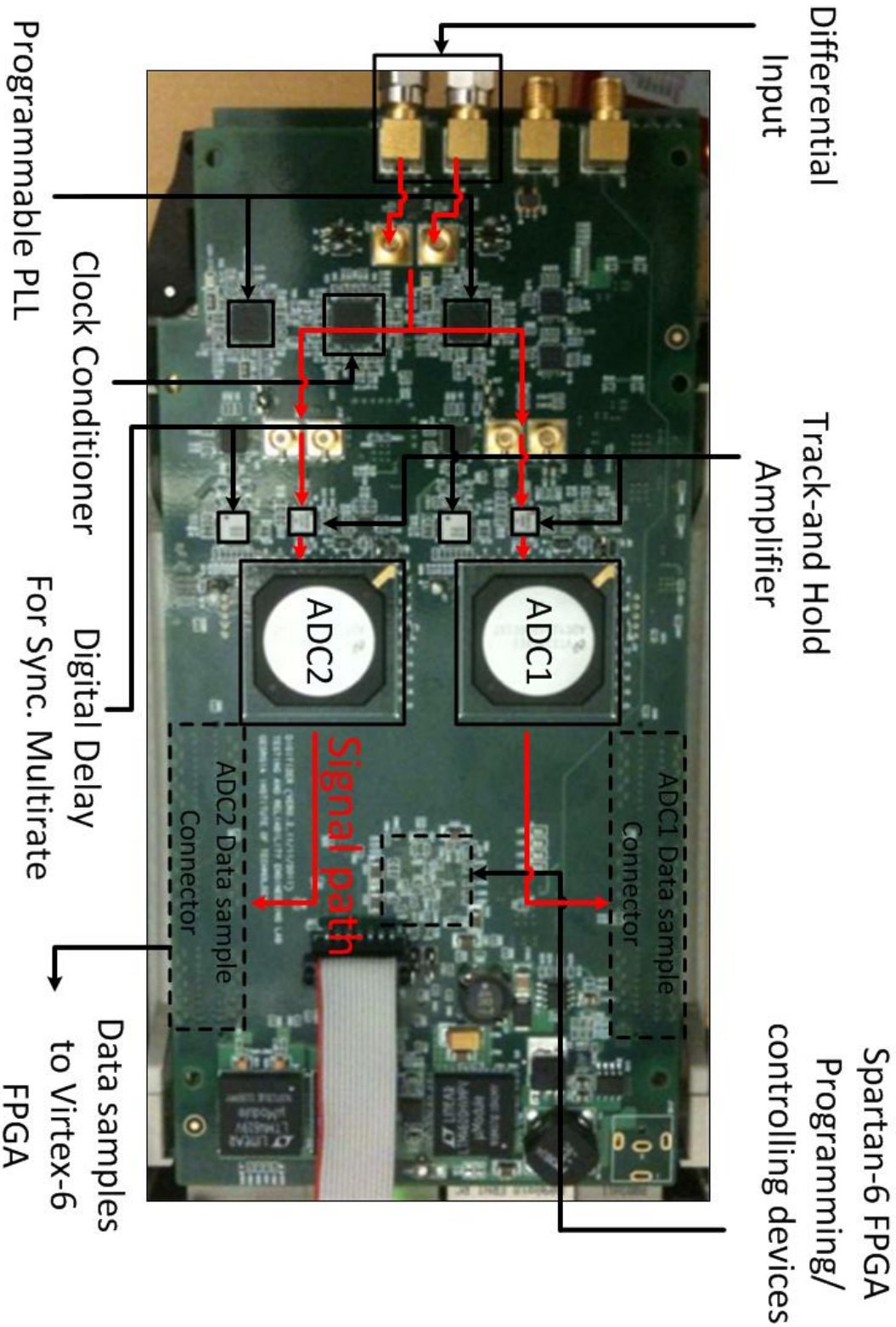

Figure **2.19. Hardware prototype of the proposed design**

2.4 Summary

In this work a low-cost and low-complexity sub-Nyquist signal acquisition hardware architecture and associated algorithms are proposed for spectrum characterization of sparse wideband signals. The proposed scheme is based on an asynchronous multi-rate sampling scheme. Compared with other sub-Nyquist sampling methods, the proposed work has low system complexity and requires minimum effort for calibration. Because it has the advantage of low-complexity, the proposed system can be implemented with one or multiple channels without complicated synchronization mechanisms, which makes sub-Nyquist spectrum sensing achievable at low-cost. The proposed sampling scheme and algorithms are verified with a hardware prototype implemented with all off-the-shelf components.

CHAPTER 3

LOW-COST WAVEFORM RECONSTRUCTION USING BAND-INTERLEAVED INCOHERENT UNDERSAMPLING

This chapter introduces a low-cost time-domain waveform reconstruction technique, which combines incoherent undersampling and the band-interleaved technique. With the back-end signal processing algorithm, it does not require any mutual synchronization between the input signal, the mixing signal and the sampling clock. Section 3.1 starts this chapter by introducing some advancement in incoherent undersampling. Section 3.2 introduces a band-interleaved undersampling technique, which still requires synchronization between the mixing signal and the input signal. The major contribution is in Section 3.3, in which the band-interleaved incoherent undersampling without any mutual synchronization is proposed.

3.1 Incoherent Undersampling

Reconstruction of periodic digital waveforms is utilized for testing high-speed systems. Even with multiple parallel ADCs, Nyquist rate sampling is very difficult to implement at high data rates and is susceptible to distortion due to a small amount of mismatch between the parallel paths. Various undersampling techniques are used to overcome the sampling rate bottleneck and reconstruct the signal waveforms. Increasing the effective sampling rate by using equivalent time sampling (ETS) to employ a fixed sampling clock and a sweeping delay, which increases in every trigger cycle. In source-

synchronous design, capturing the noise information is if the reference clock provided to the device under test (DUT) is relatively clean. If the trigger signal provided by the DUT is already noisy, it is difficult to precisely characterize the signal integrity of the system. Incoherent undersampling (IUS) techniques utilize external uncorrelated clock and back-end DSP processing to reconstruct signal waveforms [64, 81]. One major benefit of IUS is that it does not require synchronization between the DUT clock and the sampling clock. The hardware acquisition does not require a trigger signal or synchronization between the data clock and the sampling clock. Signal processing algorithms are used to estimate the period of the input periodic signal and fold the samples into the estimated period to form a whole-period waveform. Clean measurement clocks can be provided to the ADC by precise clock generation equipment. Therefore, the DUT can be characterized with minimal bias. As shown in Figure 3.1, a periodic signal with period, T_{f_0}, is incoherently sampled with sampling frequency $1/T_S$, which does not need to be higher than the Nyquist rate of the input signal. The samples are folded into the period T_{f_0} to form the whole-period waveform.

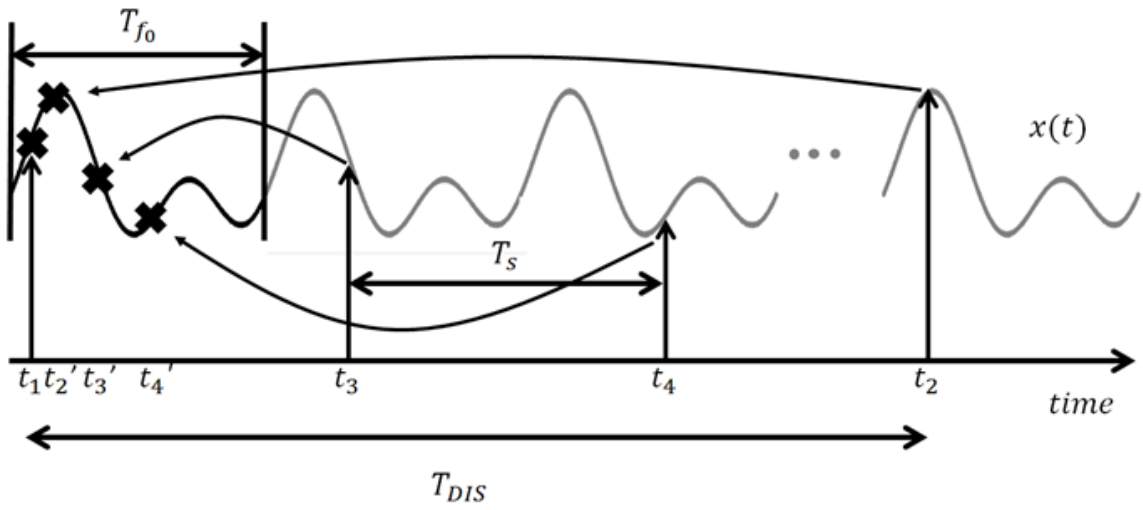

Figure 3.1 Incoherent Undersampling

3.1.1 Fundamental Frequency Estimation with Total Variation

Different methods for fundamental period estimation for incoherent undersampling have been studied [64, 81]. The following paragraph provides another metric for estimating the fundamental period of a signal. Compared to previous methods, it requires less computation and has more accurate estimation results.

The fundamental period T_{f_0} is estimated by minimizing the total variation of the folded samples. Let $x(t)$ be a periodic signal with fundamental period T_{f_0}. $x(t)$ is sampled with sampling period T_S. Suppose the samples are folded into an estimated period, $\tilde{T}$, that is close to T_{f_0}. Then,

$$t' = mod(t, \tilde{T})$$

Where t' is the new timing for the samples within the period. Let X be the sample set ordered with t'. As shown in Figure 3.1, when the period $\tilde{T}$ is equivalent to the actual fundamental period T_{f_0}, the waveform of the input periodic signal can be recovered. However, as the difference between $\tilde{T}$ and T_{f_0} increases, the folded waveform becomes fuzzy and scattered across all the plots eventually, as shown in Figure 3.1.

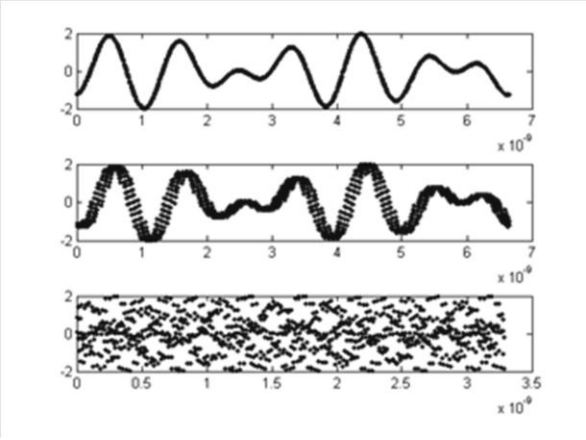

Figure 3.1 Folding samples of a periodic signal into a period $\tilde{T}$.

The phenomenon is similar to incorrect triggering in a trigger-based oscilloscope. The metric that can be used to estimate the correctness of the estimation is total variation. The calculation of the total variation of a folded sample set X is

$$TV(X, \tilde{T}) = \sum_{i=2}^{N} |x[i] - x[i-1]|,$$

Where N is the number of samples, and $x[i]$ represents the ith samples after folding into period $\tilde{T}$. When the period $\tilde{T}$ is *not* close to the fundamental period, T_0, the absolute value of the difference between the adjacent sampling points is relatively large since the samples are scattered across the whole range randomly. When the estimated period $\tilde{T}$ is close to the fundamental period, T_{f_0}, the folded samples form a smooth whole period waveform, and the total variation is small. Given a roughly known fundamental period, the estimated fundamental period can be obtained by sweeping around the given period and choosing the one that gives the minimum total variation of the folded samples.

Determining the minimum sweeping step, Δf, an assumption is made that after folding, the average space between two adjacent samples is $\frac{T_{f_0}}{N}$. This is the case when all folded samples are equally spaced. For this reason, it is necessary to find the minimum frequency step Δf that will make the samples reorder. Suppose the real time distance of two adjacent samples before the folding operation is T_{DIS} , as shown in Figure 3.1. For two different periods T_f and $T_{f'}$, the T_{DIS} can be expressed as follows:

$$T_{DIS} = \left\lfloor \frac{T_{DIS}}{T_f} \right\rfloor T_f + r$$

$$T_{DIS} = \left\lfloor \frac{T_{DIS}}{T_{f'}} \right\rfloor T_{f'} + r'$$

Subtracting these two equations results in

$$\Delta = b(T_f - T_{f'}) = b\left(\frac{1}{f} - \frac{1}{f'}\right) = b\left(\frac{\Delta f}{f\,f'}\right).$$

Since these are two adjacent points,

$$\left\lfloor \frac{T_{DIS}}{T_f} \right\rfloor = \left\lfloor \frac{T_{DIS}}{T_{f'}} \right\rfloor = b.$$

Reordering the samples requires that the shift of the samples after modulus Δ be greater than the average sample space between two adjacent samples. That is,

$$\Delta > \frac{T_f}{N} \approx \frac{T_{f'}}{N}.$$

Therefore,

$$b\left(\frac{\Delta f}{f\,f'}\right) > \frac{T_f}{N}.$$

Substituting b using $\frac{T_{DIS}}{T_{f'}}$ results in

$$\Delta f > \frac{1}{T_{DIS}N}.$$

It can now be assumed that the average T_{DIS} is of the order $O(NT_S)$. Thus,

$$\Delta f > O\left(\frac{F_S}{N^2}\right).$$

This means that the sweeping step can be reduced for this time-domain folding technique as the number of samples increases. However, even though the sweeping step can be small, in reality, it is not realistic to achieve very fine resolution due to the computational cost. In addition, there will be estimation errors due to the discrete sweeping steps. Performing a time interval error (TIE) analysis reveals that there will be a constant drift of the TIE, which needs to be compensated to achieve a more precise characterization.

The proposed signal waveform reconstruction technique is tested with a real hardware setup. The proposed method is verified with the construction of a 127-bit 4Gbps PRBS

signal, as shown in Figure 3.3. The eye diagram and the associated cost function is shown in Figures 3.4 and 3.5.

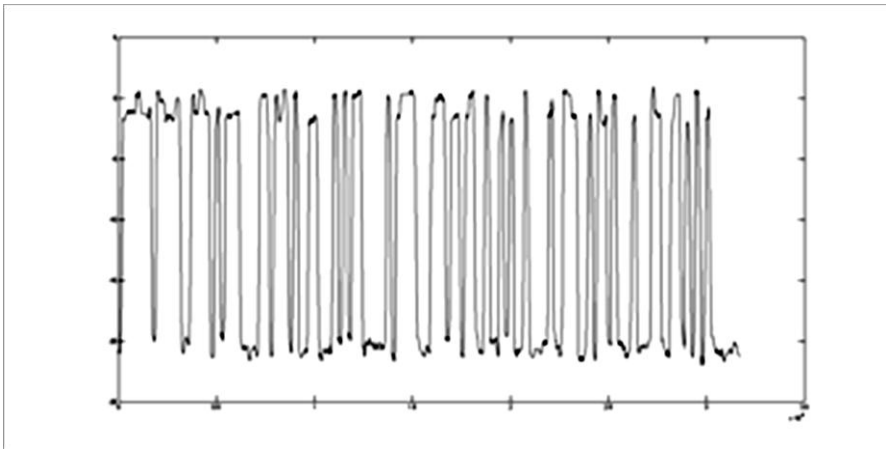

Figure 3.3. Hardware Measurement – 127 bit, 4Gbps PRBS Signal Reconstruction

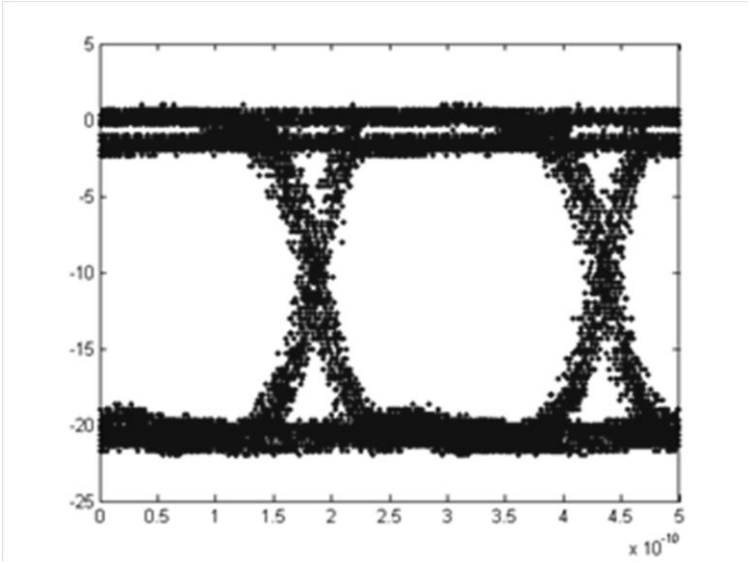

Figure 3.4. Hardware Measurement – Eye Diagram of127 bit, 4Gbps PRBS Signal

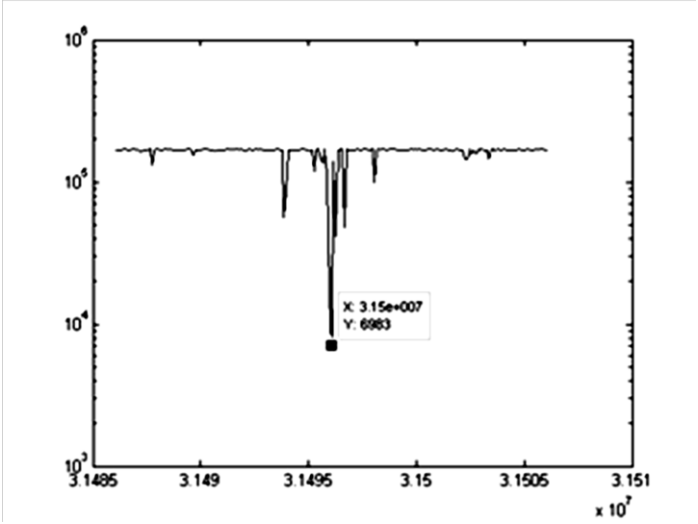

Figure 3.5 Hardware Measurement – Cost Function of127 bit, 4Gbps PRBS Signal

Time-domain visualization usually requires signals to be periodic or have periodic properties in the time domain. For example, a random bit pattern is not a periodic signal and does not have a fundamental period, but the eye diagram can still be recovered by triggering oscilloscopes with integer multiples of bit periods. In this case, the metric mentioned earlier would fail. To recover the eye diagram of random digital sequences with IUS, we propose another metric for estimating the bit period of random digital signals.

Similar to the observation in Figure 3.1, if a folding time period is close to the real bit period, the folded sample points will yield the maximum eye opening. If the folding period is not close to the bit period, the sampling points will be scattered across all the plots. Based on this observation, another metric is designed to sense the eye opening. The plot is partitioned into many rectangular boxes. The resolution of the boxes is much coarser compared to the waveform of the image. If the folding period is very close to the real bit period, the sampling points after the folding operation will reside in fewer boxes. A binary image is used to indicate whether there are sample points that fall into each

rectangular box after folding. “1” indicates that there is at least one sample that falls into the corresponding box. “0” indicates that there is no sample that falls into the corresponding box. When the sampling points are scattered, the sum of the binary image is large. For condensed sampling points, the sum of the binary image will be small. This metric is used to reconstruct a random bit sequence. The plot is partitioned into a 30x30 binary image. The reconstruction result of the hardware measurement is shown in Figure 3.6.

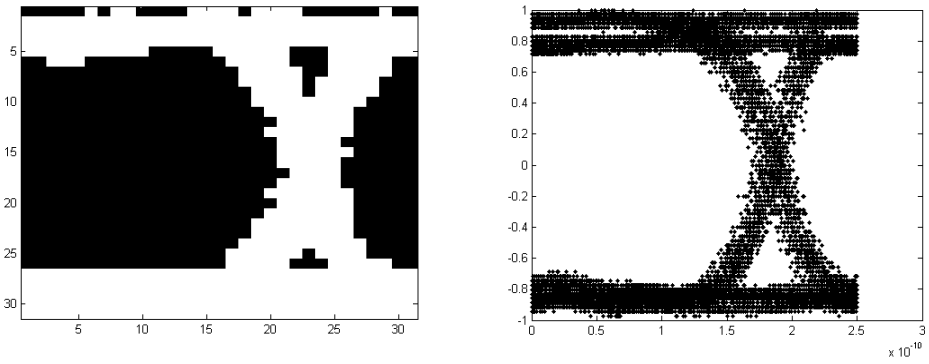

Figure 3.6 Hardware Measurement
(Left) Binary image for estimating the bit period of a 4Gbps random bit pattern
(right) Recovered eye diagram

3.1.2 Uncorrelated Signal Separation

Incoherent undersampling requires the input signal to be periodic. The spectra of periodic signals consist of multiple tones. However, multi-tone signals are not necessarily periodic. Consider a very simple case below. Let

$$f(t) = \sin t + \sin 2t$$

$$g(t) = \sin \sqrt{2}t + \sin 5\sqrt{2}t$$

$$h(t) = \sin\sqrt{2}t + \sin 5\sqrt{2}t$$

$f(t)$ and $g(t)$ are two zero-mean periodic signals and let the period be T_f and T_g respectively. $h(t)$ is not a periodic signal since the periods of the two signals are relatively irrational. It is not possible to reconstruct the signal $h(t)$ by folding the waveform into the period of $f(t)$ or the period of $g(t)$. However, it is still possible to reconstruct the waveform of $f(t)$ and $g(t)$ separately with incoherent undersampling. Suppose the samples are folded into the period of $f(t)$, T_f

$$t' = mod(t, T_f),$$

Let t_0 be phase within $0 \le t_0 \le T_f$. Let sample set H_{t_0} contains folded samples falling into an interval Δt ($\Delta t \ll T_f$) centered at t_0.

$$H_{t_0} = \left\{h(t_h)\ where\ t_0 - \frac{1}{2}\Delta t \le mod(t_h, T_f) \le t_0 + \frac{1}{2}\Delta t\right\},$$

where t_h is the sampling time of samples in H_{t_0} before folding. Since Δt is small, we know that

$$t_h \approx kT_f + t_0, \qquad k \in \mathbb{N}^+(positive\ integers)$$

Therefore, for the samples in H_{t_0},

$$h(t_h) = h\left(kT_f + t_0\right) = f\left(kT_f + t_0\right) + g(t_h) = f(t_0) + g(t_h).$$

If we average N number of samples in H_{t_0}, we have

$$\frac{1}{N}\sum_h h(t_h) = \frac{1}{N}(Nf(t_0) + \sum_h g(t_h)).$$

Because $f(t)$ and $g(t)$ are uncorrelated, sample $g(t)$ at time $kT_f + t_0$ is very likely to sample $g(t)$ at random points. We have made the assumption that the mean of $g(t)$ and

$f(t)$ are zero. Therefore, the second term of the equation above is close to zero when N is big. That is, the average of the samples in set H_{t_0} can be expressed as

$$averge\ of\ samples\ in\ H_{t_0} = \frac{1}{N}\sum_h h(t_h) \approx f(t_0).$$

This implies that each periodic component can be obtained by folding all samples into a (their) corresponding period and taking the average within the small time intervals. Other uncorrelated components are averaged to zero. If samples of $h(t)$ are collected and folded into periods T_f and T_g, the periodic components $f(t)$ and $g(t)$ can be constructed. The proposed methodology for CJ separation is similar to the technique presented in this section. However, superposition of periodic digital sequences with the same bit period is always correlated and periodic. The period is the least common multiple (LCM) of different bit periods. Therefore, using this requires more constraints on bit periods of the sequences. This implies that each periodic component can be obtained by folding all samples into corresponding periods and taking the average within small time intervals. Other uncorrelated components are averaged to zero. If samples of $h(t)$ are collected and folded into periods T_f and T_g, the periodic components $f(t)$ and $g(t)$ can be constructed, as shown in Figure 3.7.

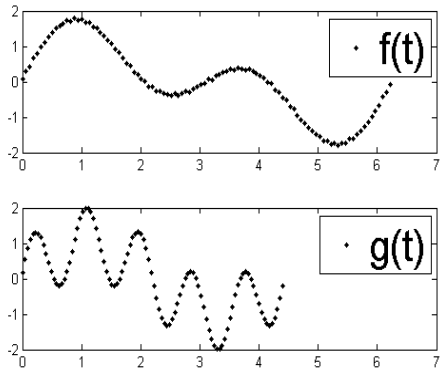

Figure 3.7 Reconstruction of two uncorrelated periodic components $f(t)$ and $g(t)$

3.2 Band-interleaved Incoherent Undersampling: Preserving Periodicity of Upper-band Signals

Track-and-hold circuitry is used to increase ADC input bandwidth. To extend the bandwidth of the track-and-hold circuitry, band-interleaved architecture is used in some modern oscilloscopes [59]. However, within each band, Nyquist rate sampling is still used in each band. Undersampling has been proved to be capable of reconstructing periodic waveforms with low sampling rates. However, periodic signals in the upper-band after down-conversion may no longer be periodic, and this makes the reconstruction difficult. In Sections 3.2 and 3.3, two band-interleaved undersampling methods for time-domain signal reconstruction are proposed. In Section 3.2, the proposed method maintains the periodicity of the upper-band signal for reconstruction, while the method in Section 3.3 uses a free-running mixing signal and sampling clocks and back-end signal processing to compensate the lack of synchronization.

In order to make the down-converted waveform periodic, one can choose the down-mixing frequency LO to be the integer multiple of the fundamental frequency of the input periodic signals. In this scheme, first, the fundamental frequency of the baseband signals is estimated. Once the fundamental frequency f_0 is obtained, the higher frequency bands are down-converted with integer multiples of f_0. Since the frequencies of the tones in the higher frequency bands are also integer multiples of the fundamental frequency, the down-converted tones will still be integer multiples of the fundamental frequency and, hence, periodic. (Figure 3.8)

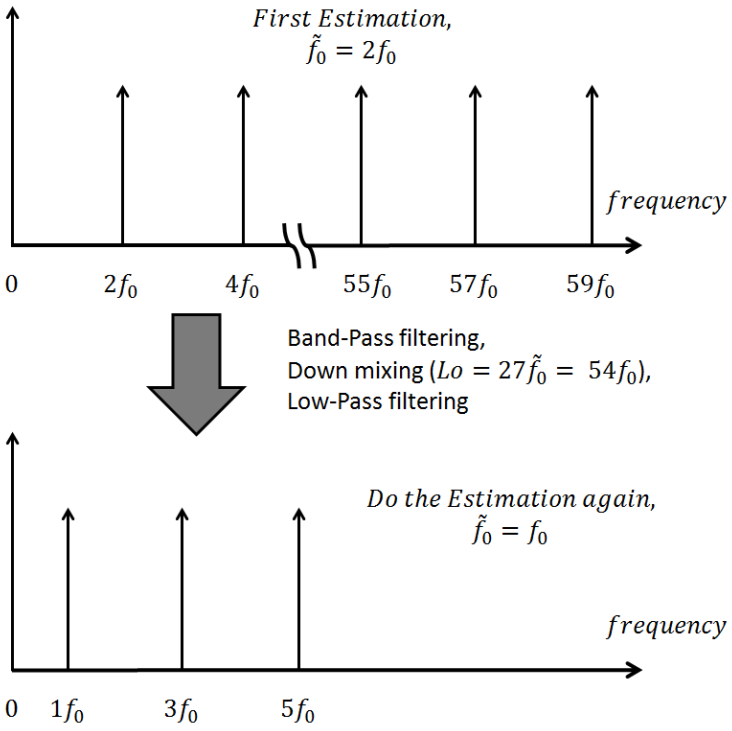

Figure 3.8 Periodic Multi-tone Signal Down-Conversion

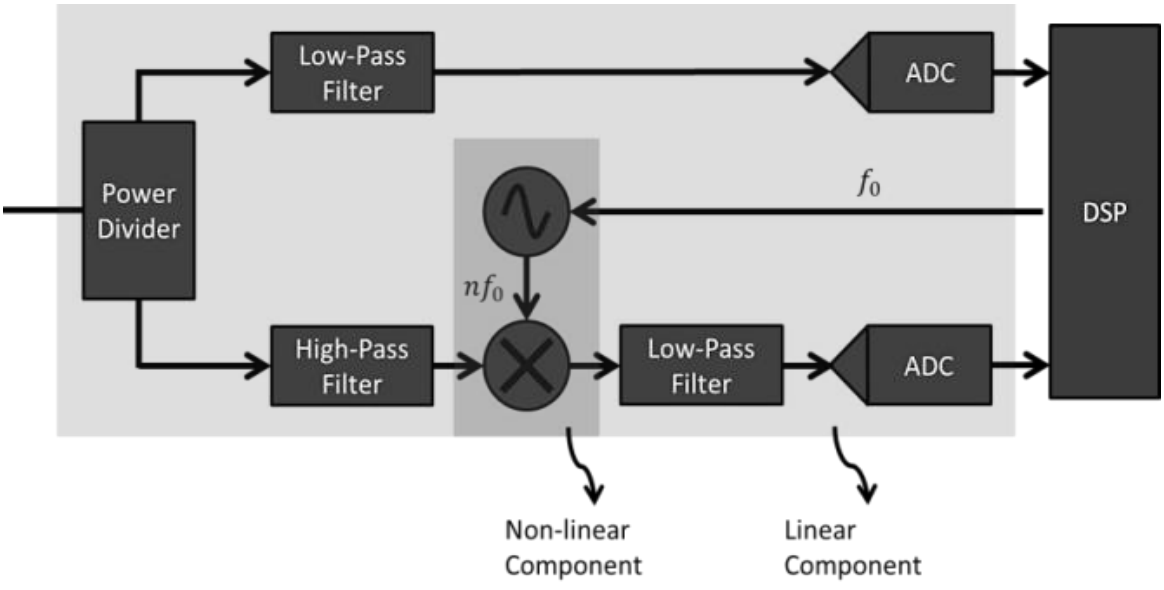

Figure 3.9 Band-interleaved undersampling block diagram.

The system is shown as Figure 3.9. One thing that should be noted is that $f_0$may be an integer multiple of the real fundamental frequency. Since the down-converted signal is periodic, it can be reconstructed in the same way as the lower frequency band signal, by using incoherent undersampling. To prevent aliasing, a high pass filter is needed in the high frequency path before the mixer. However, proper reconconstruction of the wide band signal requires intensive calibration of the phase and amplitude distortion introduced by the hardware in each signal path. A 2-channel incoherent undersampling system is simulated to prove the concept proposed in this band-interleaved scheme. As shown in Figure 3.10, a 4-tone wideband periodic signal is split into two channels, a baseband and a high-frequency band. The fundamental period / frequency is estimated in the baseband channel. Once the fundamental frequency is estimated, integer multiples of the estimated fundamental frequency is used to down-convert the upper-band signal. Therefore, the upper-band signal remains periodic even after down mixing. The baseband and the upper-band signal can be reconstructed using IUS or ETS. Then, the reconstruction of two channels can be combined to form the periodic input signal.

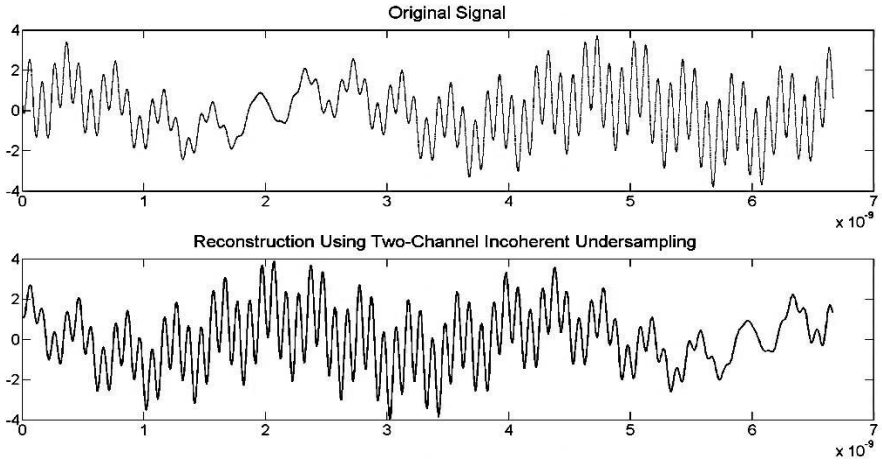

Figure 3.10. Multi-tone Periodic Signal Reconstruction Using Two-channel Incoherent Undersampling

3.3 Bandwidth Interleaved Signal Acquisition Using Free Running Undersampling Clocks and Mixing Signals

Time-domain measurement is essential for characterizing high-speed signals. The cost of waveform measurement instruments is driven up by the requirement of high-sampling rate and the wide input bandwidth. As systems being scaled to multi-GHz frequencies, mutual synchronization of input signal, sampling clocks, and the mixing signal in band-interleaved schemes has significantly increased the cost and complexity of hardware designs.

Waveform Reconstruction Technique	Direct sampling (no signal mixing)			Signal mixing involved				
	Real-time scope	Sampling scope (equivalent time sampling)	Incoherent undersampling [64]	Asynchronous Time Interleaving [104]	Digital Band Interleaving [103]	[102]	[105]	This work
Sampling rate reduction	No	Yes	Yes	Yes	Yes	Yes	Yes	Yes
Extending Track-and-hold bandwidth	No	No	No	Yes	Yes	Yes	Yes	Yes
Input signal synchronization with sampling clock	Yes	Yes	No	Yes	Yes	No	No	No
Mixing signal synchronization with sampling clock	N/A	N/A	N/A	Yes	Yes	Yes	Yes	No
Description	Nyquist rate sampling	Require precise delay control	Back-end signal processing for signal period estimation	Matched symmetrical paths	Extend bandwidth with band-interleaving	Require precise mixing signal generation	Require phase synchronization between mixing signal and sampling clock	No synchronization required
Hardware complexity	High	High	Low	High	High	Low	Low	Lowest among these works

Table 3.1. Comparison of waveform reconstruction techniques

A comparison of different waveform reconstruction techniques is shown in Table 1. Equivalent time sampling is used to reconstruct waveforms using low sampling rates. Incoherent undrsampling [60-64] is later proposed to remove the constraint of synchronization between input signal and the sampling clock. These direct sampling

techniques use track-and-hold circuitry to increase the analog front-end bandwidth. To further extend the performance of the track-and-hold circuitry and reducing the sampling rate are made possible with the use of band-interleaved schemes. Digital Band Interleaved (DBI) [103] architecture increases the analog input bandwidth and reduces the required sampling rate with the band-interleaved method. Asynchronous Time Interleaving (ATI) [104] places mixers in all channels to extend bandwidth and form symmetric paths. Both methods use mixers to increase analog bandwidth, however, the total effective sampling rates from all channels are still higher than the Nyquist rate of the input bandwidth. In addition, synchronization between input signal and the sampling clocks is still required. To remove the synchronization requirement and still extend the bandwidth with mixers, band-interleaved incoherent undersampling techniques [102, 105] are proposed. However, these techniques still require frequency and phase synchronization between the mixing signals and the sampling clocks.

This chapter proposes an algorithm to combine the incoherent undersampling and the band-interleaved scheme without any mutual synchronization between the input signal, the mixing signals, and the sampling clocks. The proposed method relies completely on back-end spectrum analysis and signal processing to compensate the lack of synchronization and to reconstruct the upper-band signal. Without the synchronization constraint, the proposed method can be easily scaled to multi-GHz frequencies. Since no sophisticated synchronization hardware scheme is needed, different components, such as mixers and ADCs, can be built as independent modules, and the system can be assembled for a minimum cost, which is mainly the total cost of the independent modules. It is estimated that a multi-GHz signal acquisition system using the proposed scheme can be

assembled in a lab for less than ten thousand dollars. The contribution of this work is listed as follows:

- A band-interleaved undersampling scheme is proposed without any signal synchronization and with minimized hardware complexity.
- Without the requirement of synchronization, this work can be easily scaled to multi-GHz frequencies and can be built for a minimum cost.
- Associated back-end signal processing algorithms are proposed to compensate the lack of synchronization.

3.3.1 Band-Interleaved Undersampling Architecture

The proposed band-interleaved incoherent undersampling architecture is shown in Figure 3.11. The input signal is passed through a low-pass filter, which represents the total system input bandwidth, and then is divided into two channels: a baseband channel and an upper-band channel. The baseband channel uses a low-pass filter to remove the signal in the upper band and capture the information within the lower band. The signal in the baseband is incoherently sampled and reconstructed using the incoherent undersampling technique. The estimated fundamental frequency during the reconstruction process is later used for the upper-band reconstruction algorithm. Similarly, the upper-band channel uses a high-pass filter to remove the signal in the baseband channel and down-convert the upper-band signal with a mixer. The low-pass filter after the mixer is used to remove the undesired high-frequency tones from the mixing and the local oscillator (LO) feed-through. The signal is then sampled incoherently at the same rate as for the baseband. It is important to note that there is no synchronization between any of the signals. Since the mixing frequency can be chosen

arbitrarily, the down-converted signal may not be periodic at the mixer output. In the following section, an algorithm is proposed to address this issue and reconstruct the upper-band time-domain waveform.

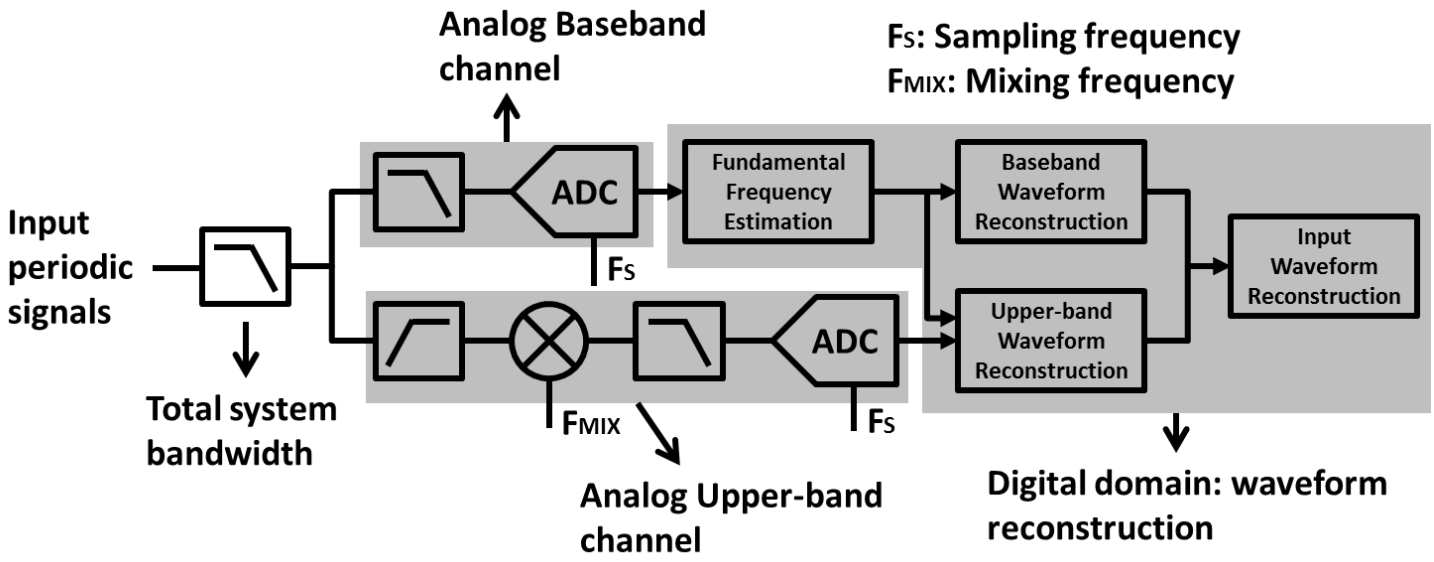

Figure 3.11. Proposed band-interleaved incoherent undersampling architecture

3.3.2 Upper-Band Signal Reconstruction Overview

If a periodic signal can be directly sampled without bandwidth limitations, it can be reconstructed with phase remapping as used in equivalent time sampling and incoherent undersampling techniques. However, with a mixer used for down-mixing in the upper-band channel, the signal at the output of the mixer may not be periodic. The goal of the proposed upper-band reconstruction algorithm is to process the upper-band samples such that they look as if they were acquired by directly sampling the upper-band signal without the mixer. Once the samples are processed, phase remapping can be applied to reconstruct the time-domain waveform of the upper-band signal.

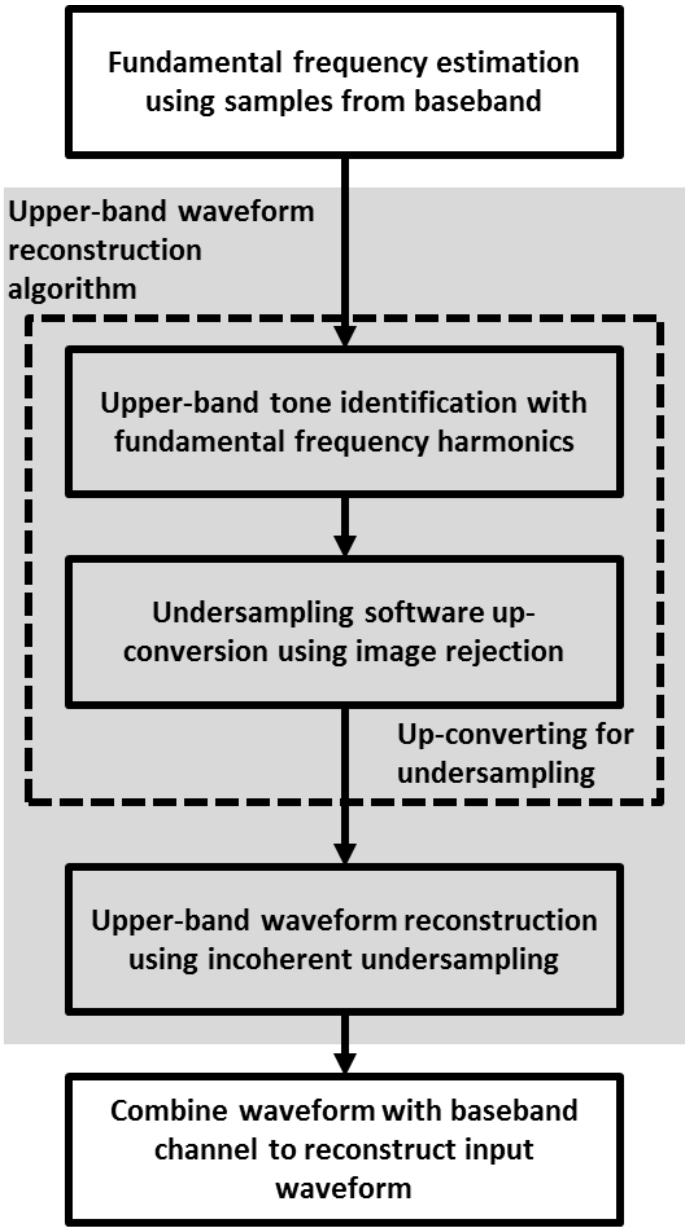

Figure 3.12. Upper-band reconstruction algorithm flow. The proposed upper-band reconstruction algorithm is a 3-step approach, as shown in the colored box. The first two steps of the three are the up-converting algorithm, as shown in the dashed box.

The proposed upper-band waveform reconstruction algorithm is a three-step approach, and the flow is shown in Figure 3.12. The first two steps are used to up-convert the signal, as shown in the dashed box in Figure 3.12. With oversampled signals, in the absence of aliasing, the signals can be up-converted in the digital domain by sample-

point-wise multiplication of the samples with samples of the sinusoidal mixing signal. However, since in this case, the signal is acquired with undersampling, the up-converting technique has to be modified for the undersampling scheme. The first step is to identify the upper-band signal with the harmonics of the fundamental frequencies in the frequency domain. The second step is to shift the identified tones to the proper position and use the image rejection technique to remove the undesired images. These two steps remove the tone-shifting effect from the down-mixing operation and make the spectrum look as if the upper-band signal had been directly sampled. The steps are illustrated in sub-sections II B and II C, respectively.

3.3.3 Upper-Band Signal Reconstruction Step 1: Upper-Band Tone Identification

An upper-band tone after down-mixing and undersampling with sampling frequency F_S can fall into DC to $1/2F_S$, as in Figure 3.13(a), or into $1/2F_S$ to F_S, as in Figure 3.13(b). In either case, a symmetric conjugate tone also appears in the other half of the spectrum; therefore, a method is needed to identify the actual aliased tone. Identifying the tone requires calculating the harmonic frequencies of the estimated fundamental frequency in the upper-band. Typically, these tones are integer multiples of the estimated fundamental frequency in the baseband. Let these frequencies be F_H. Then,

$$F_0 = mod(F_H - F_{MIX}, F_S).$$

F_0 represents the possible frequencies that F_H may reside in in the aliased spectrum. By comparing the spectrum of the samples with F_0, as shown in Figure 3.14, one can determine whether the upper-band tones fall within interval DC to $1/2F_S$ or interval $1/2F_S$ to F_S. Figure 3.14 (a) and Figure 3.14 (b) show how two different upper-band

tones can yield the same spectrum of the acquired samples and how the proposed identification method is performed.

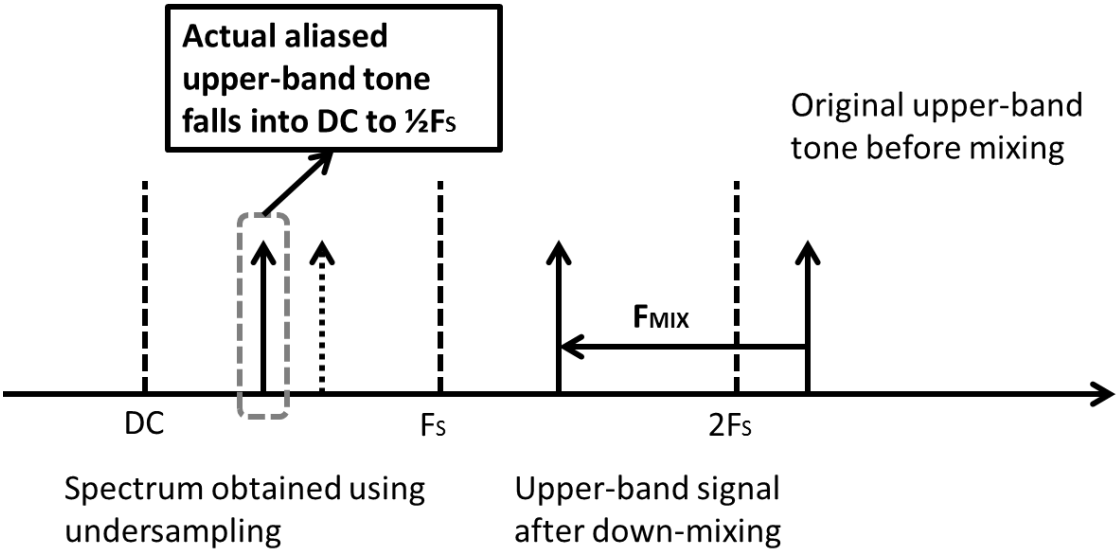

Figure 3.13 (a). An upper-band tone falls into DC to $1/2F_S$

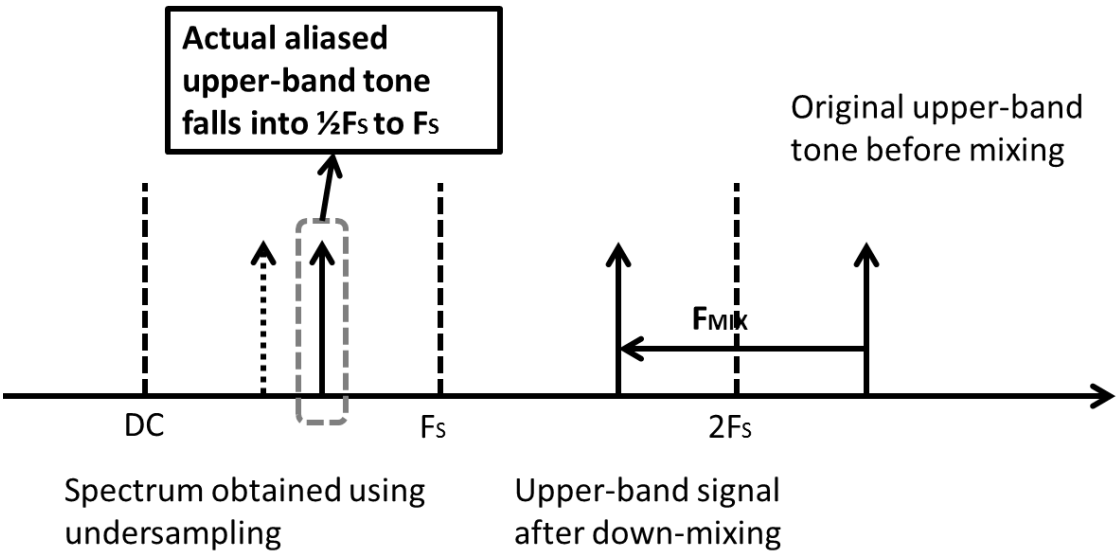

Figure 3.13 (b). An upper-band tone falls into $1/2F_S$ to F_S

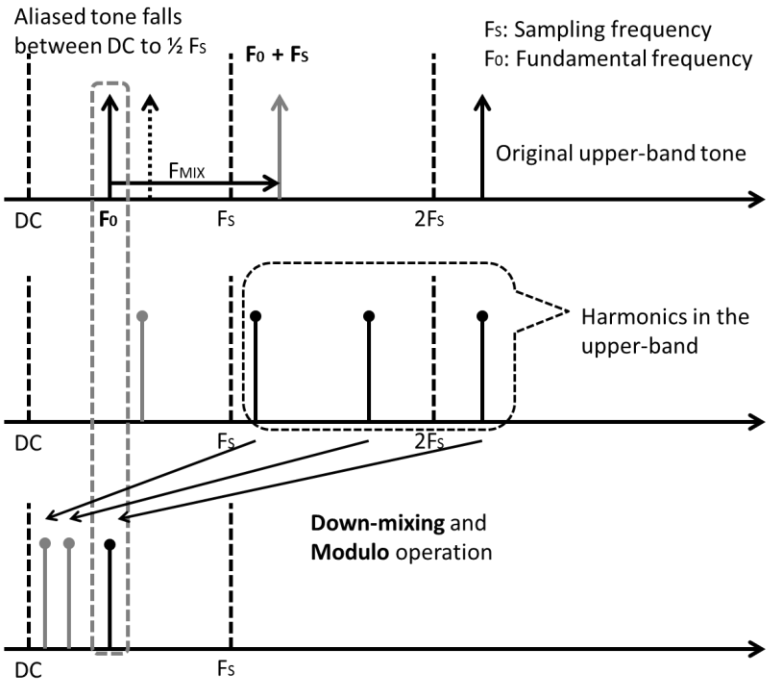

Figure 3.14 (a). An upper-band tone falls into DC to $1/2F_S$ - harmonics in the upper-band are used to identify the correct tone

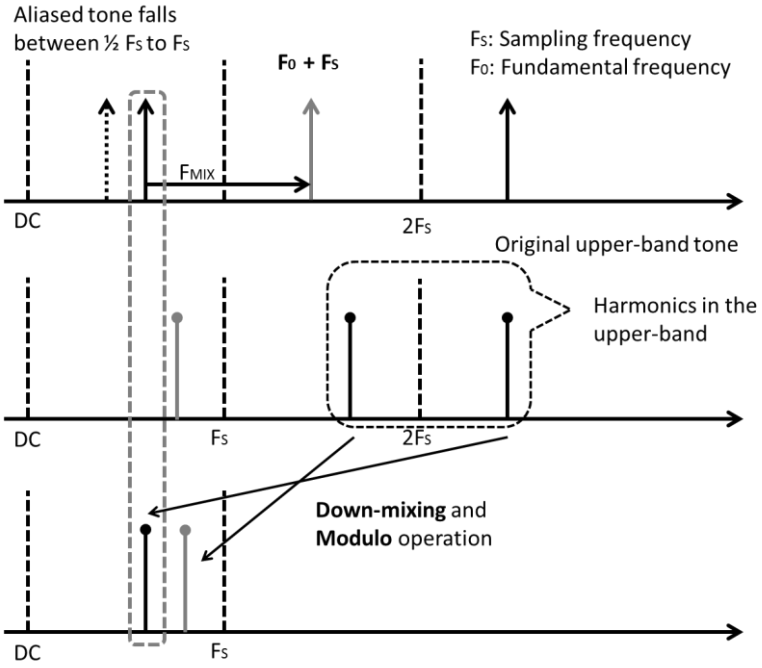

Figure 3.14 (b). An upper-band tone falls into $1/2F_S$ to F_S, - harmonics in the upper-band are used to identify the correct tone

Figure 3.14 (a) and Figure4 (b) show how two different tones from the upper-band can yield the same spectrum of the acquired samples.

3.3.4 Upper-Band Signal Reconstruction Step 2: Up-Converting with Image Rejection

Once the upper-band tones are identified as described in the last section, the tones need to be shifted and the effect of the mixing process removed. Shifting a tone is done by multiplying the samples with a sinusoid. Suppose the samples have a tone at F_0. When the samples are multiplied by a sinusoid of frequency F_{MIX}, two tones will be created: $mod(F_0 + F_{MIX}, F_S)$ and $mod(F_0 - F_{MIX}, F_S)$. F_S is the sampling frequency, and the modulo operation is applied because of undersampling. If the samples were oversampled, the image tone at $mod(F_0 - F_{MIX}, F_S)$ could be removed by linear filtering in the digital domain. However, since the samples are acquired through undersampling, a high-pass filter or low-pass filter cannot correctly remove all the undesired images when upper-band signal consists of multiple tones. Therefore, the image rejection technique, which is widely adopted in mixer design, is used to cancel the undesired images. The process is described in the following paragraph.

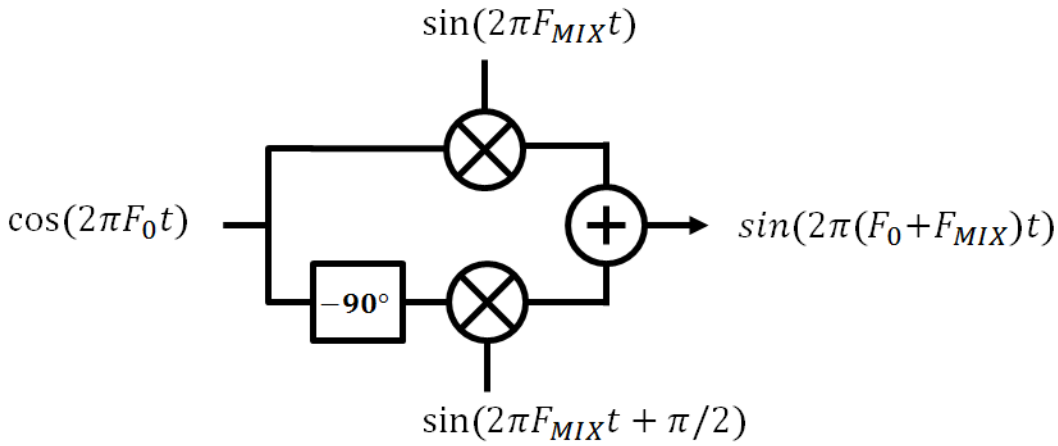

Figure 3.15. Image rejection method for up-conversion

The concept used in the digital domain is shown in Figure 3.15. Suppose the spectrum of the samples has a tone at F_0, and that obtaining a tone at frequency $F_0 + F_{MIX}$ and rejecting the tone at $F_0 - F_{MIX}$ can be done by superimposing two signals. One signal is obtained by multiplying input samples by samples of a sinusoid, $\sin(2\pi F_{MIX} t)$. The other signal is obtained by rotating the input signal by 90° and multiplying it with $\sin(2\pi F_{MIX} t + \pi/2)$. After these two signals have been superimposed, a tone at frequency $F_0 + F_{MIX}$ can be obtained. The mathematical operation in Figure 5 is shown as below:

$$\cos(2\pi F_0 t)\sin(2\pi F_{MIX} t)$$

$$= \frac{1}{2}\sin(2\pi(F_0 + F_{MIX})t) - \frac{1}{2}\sin(2\pi(F_0 - F_{MIX})t) \quad (Eq.1)$$

$$\cos(2\pi F_0 t - \pi/2)\sin(2\pi F_{MIX} t + \pi/2)$$

$$= \frac{1}{2}\sin(2\pi(F_0 + F_{MIX})t) + \frac{1}{2}\sin(2\pi(F_0 - F_{MIX})t) \quad (Eq.2)$$

$$Eq.1 + Eq.2 = \sin(2\pi(F_0 + F_{MIX})t)$$

$\cos(2\pi F_0 t)$ represents a tone of the input samples. Delaying a tone by $\pi/2$, as in Eq. 2, is done by multiplying the FFT vector around the frequency F_0 by $-1j$ and multiplying its symmetric conjugate frequency $F_S - F_0$ by $1j$, where F_S is the sampling frequency.

For each identified tone of the acquired samples, the image rejection method is applied and the tone is shifted to the position such that the spectrum looks as if the upper-band signal had been directly sampled without a mixer. The incoherent undersampling is then used to reconstruct the upper-band waveform in the time-domain. Since the mixing signal and the sampling clock are not synchronized, as the tones are up-converted, one

can sweep around the roughly known mixing frequency to find the frequency that gives the smoothest reconstruction waveform.

After reconstruction of the baseband and upper-band waveform, if the delay is calibrated properly, these two sample sets can be added, the superposition waveform can be folded into the fundamental period, and the input waveform can be reconstructed. Calibrating the delay requires a one-time delay calibration between the two channels.

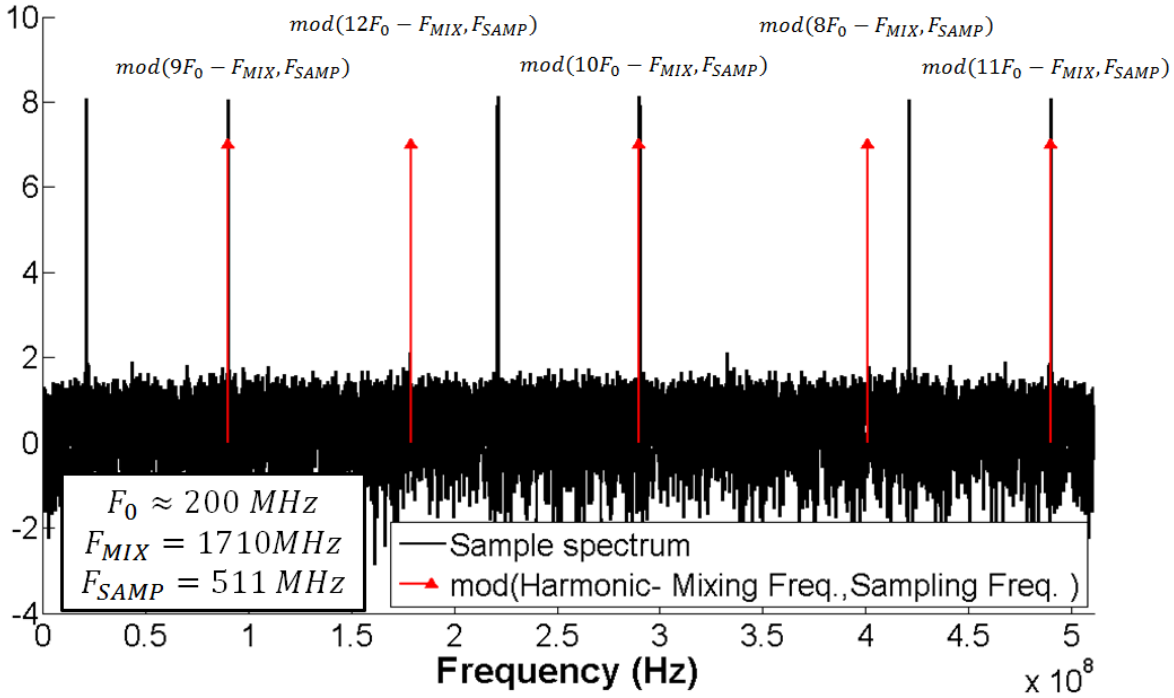

Fig 3.16. Identifying the upper-band tone. (Simulation) Three tones are identified: $9F_0, 10F_0, 11F_0$

3.3.5 Upper-Band Signal Reconstruction - Simulation

Here, a simulation of upper-band waveform reconstruction is provided to verify the proposed method. Suppose the upper-band signal consists of 3 tones, 1.8GHz, 2GHz, and 2.2GHz. The upper-band signal is down-mixed with a 1.71 GHz signal. First, the upper-band signal is identified with the method described in Section II C, as shown in

Figure 6. The red tones are the harmonics after down-mixing and the modulo operation, and the black spectrum is the spectrum of the samples acquired at 511 MHz. From Figure 3.16, the three tones are identified as the upper-band tones, $9F_0, 10F_0, 11F_0$, where F_0 is the fundamental frequency, 200 MHz. The tones and their symmetric conjugate tones are then rotated properly, as shown in Figure 3.17. The image rejection method proposed in Section II D is then used to shift the tones and to remove the mixer effect. After these two steps, the spectrum looks as if it had been acquired by directly undersampling the upper-band signal, as shown in Figure 3.18. Now, the incoherent undersampling technique can be applied to reconstruct the upper-band waveform, as shown in Figure 3.19. It is important to note that if the filtering method is used instead of the image rejection method, a specially designed filter is needed, shown as the red-dashed line in Figure 10 to filter out the undesired images.

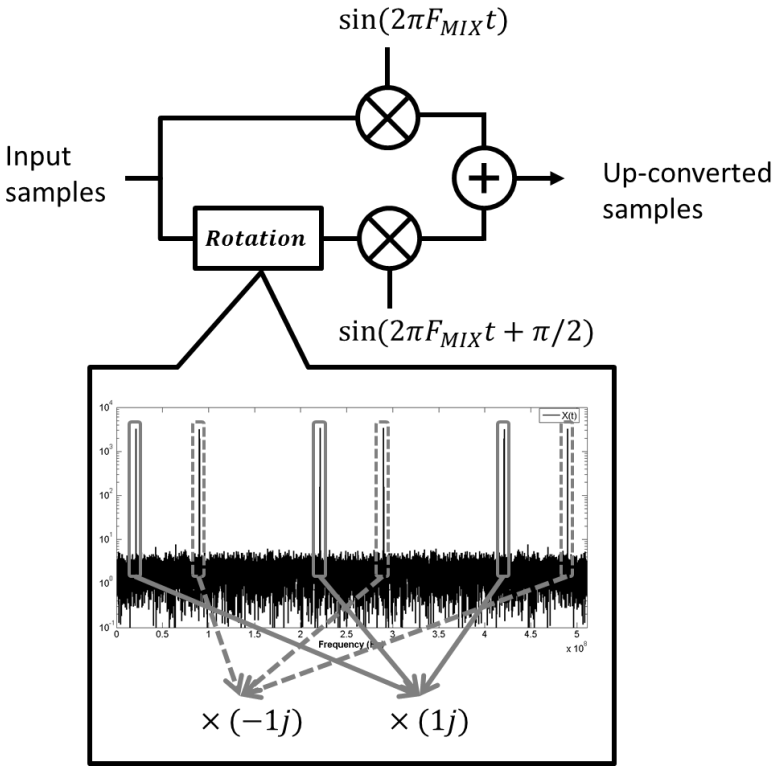

Figure 3.17. Image rejection (Simulation)

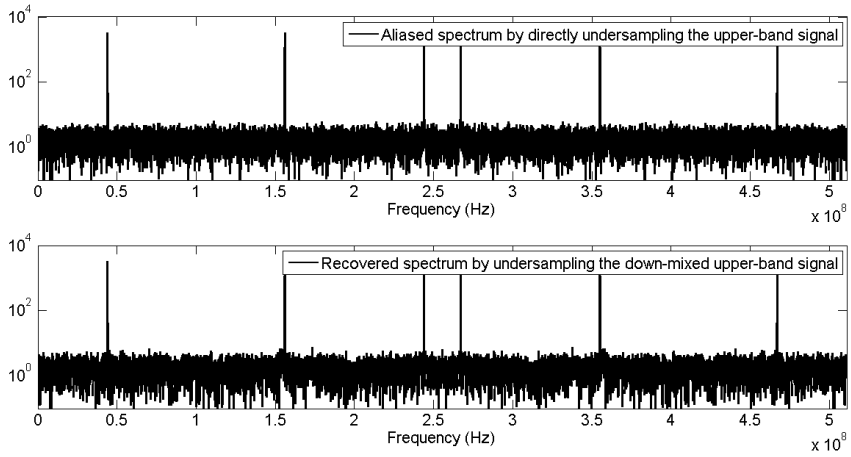

Figure 3.18. Upper-band spectrum by direct undersampling vs. reconstructed upper-band spectrum.

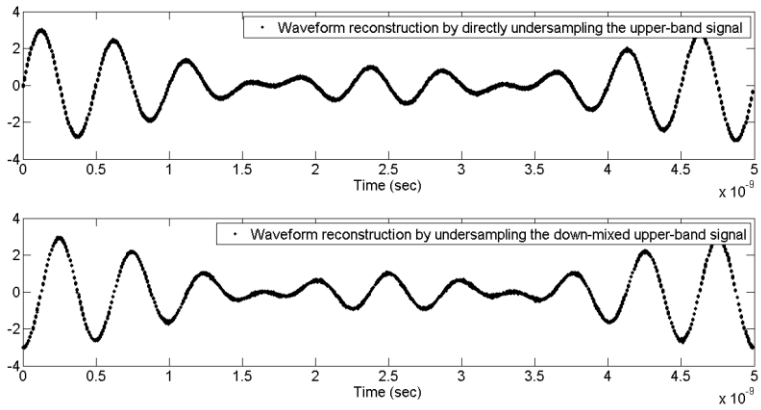

Figure 3.19. Waveform by direct undersampling vs. reconstructed upper-band waveform.

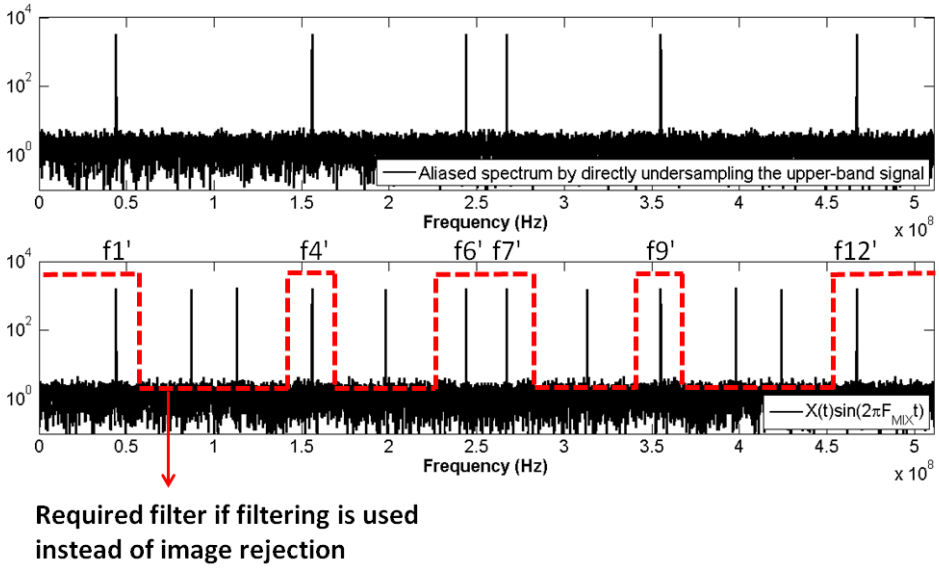

Figure 3.20. Required filter if filtering is used

3.3.6 Hardware Measurement

Next, hardware measurement is used to verify the proposed method. The hardware setup is shown in Figure 3.21. Five synchronized signal generators are used to generate 5 tones, which are 400 MHz, 600 MHz, 1.8 GHz, 2.0 GHz, and 2.2 GHz, to form a periodic input signal. The fundamental period of these five tones is 1/200MHz. They are sampled by the proposed band-interleaved signal acquisition system, which is in a different clock domain. The sampling clock is 511 MHz, and the mixing signal, which is in another clock domain, for the upper-band channel is 1.71 GHz. The baseband and upper-band signals are sampled by the I channel and Q channel of the ADC12D1800 reference board. The baseband signal contains 2 tones, 400 MHz and 600 MHz. The Nyquist rate sampling for this signal is at least 1.2 GHz, while a 511 MHz clock is used to incoherently sample it. The reconstructed baseband waveform is shown in Figure 3.22. We show the effectiveness of our algorithm by comparing the reconstruction waveforms against the waveforms acquired by a 50 GHz bandwidth oscilloscope. The 5 signal generators are synchronized with the 10 MHz reference ports on the back panel. As our measurement setup is switched from the oscilloscope to our measurement system, the phases of signals from different signal generators may drift. This makes the reconstructed baseband waveform slightly different from the waveform acquired by the oscilloscope in Figure 3.22.

The upper-band signal contains three tones, 1.8 GHz, 2.0 GHz, and 2.2 GHz. After they are down-mixed with a 1.71 GHz signal, they become around 90 MHz, 290 MHz, and 490 M Hz. It is necessary to use the word “around” because the input signal and the mixing signal are in different clock domains. Therefore, the down-mixing signal

may not be periodic. The Nyquist sampling rate for the down-mixing upper-band signal is at least 980 MHz, while 511 MHz is used to incoherently sample it. If the method described in Section II is used, the tones can be shifted, and the time domain waveform of the upper-band signal can be reconstructed, as shown in Figure 3.23. An oscilloscope is used to acquire the upper-band signal *before* the mixer, which is a periodic signal with a period 1/200MHz. The waveform is shown in Figure 3.23. As can be seen from the figure, the two waveforms are almost identical. However, the proposed band-interleaved system requires a lower ADC analog input bandwidth and a lower ADC sampling rate. Finally, the reconstructed baseband waveform and the upper-band waveform are combined to form the input waveform and compare the reconstruction with the waveform acquired by the oscilloscope, as shown in Figure 3.24.

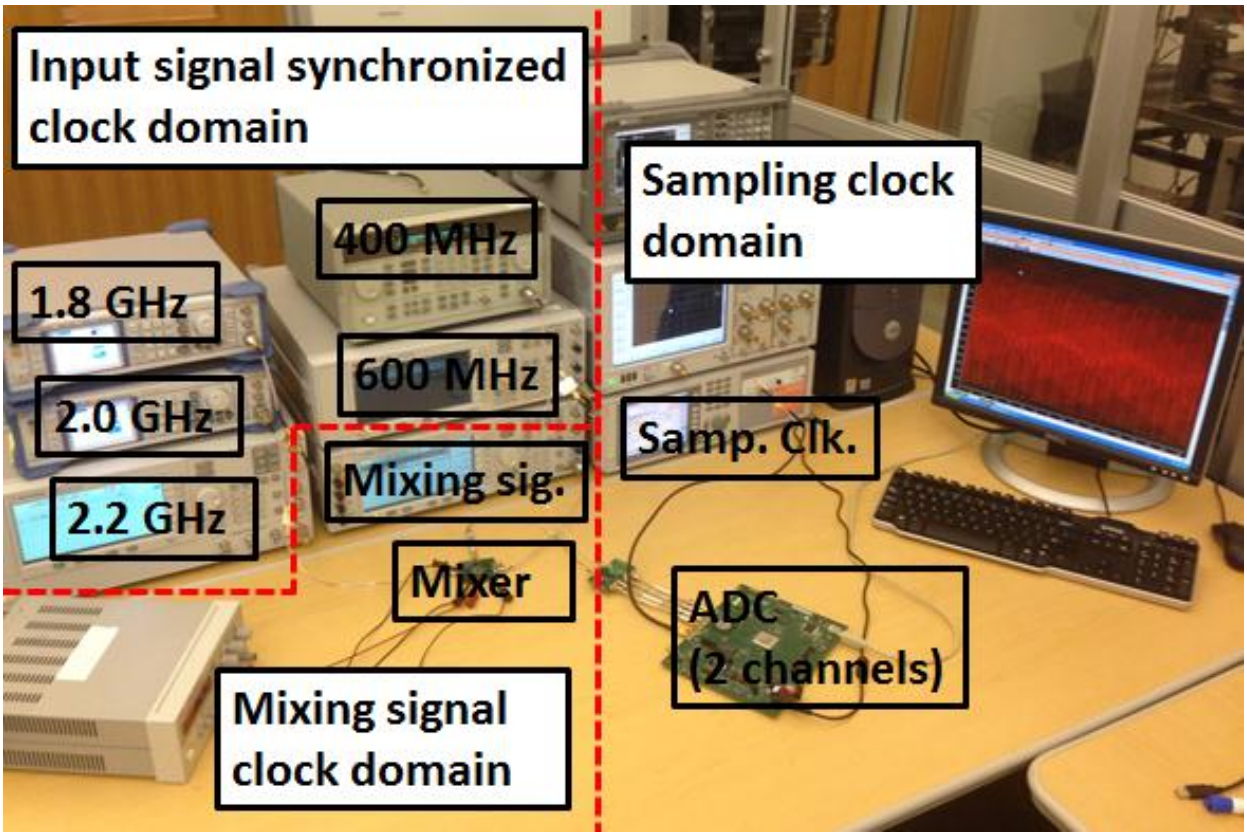

Fig 3.21. Hardware setup

In this hardware measurement setup, an ADC12D1800 reference board is used as the ADC module, and a MAX2039 evaluation board is used as the mixer module. Two high-end signal generators are used to generate the mixing signal and the sampling clocks. These two signal generators can be replaced with two much cheaper modules. For example, two oscillators, which can generate a single frequency tone around 1.7 GHz (mixing signal) and 500 MHz (sampling clock), can well serve the purpose. If the signal generators are replaced, the system can be implemented with total cost under five thousand dollars, which represents mainly the total cost of the different modules.

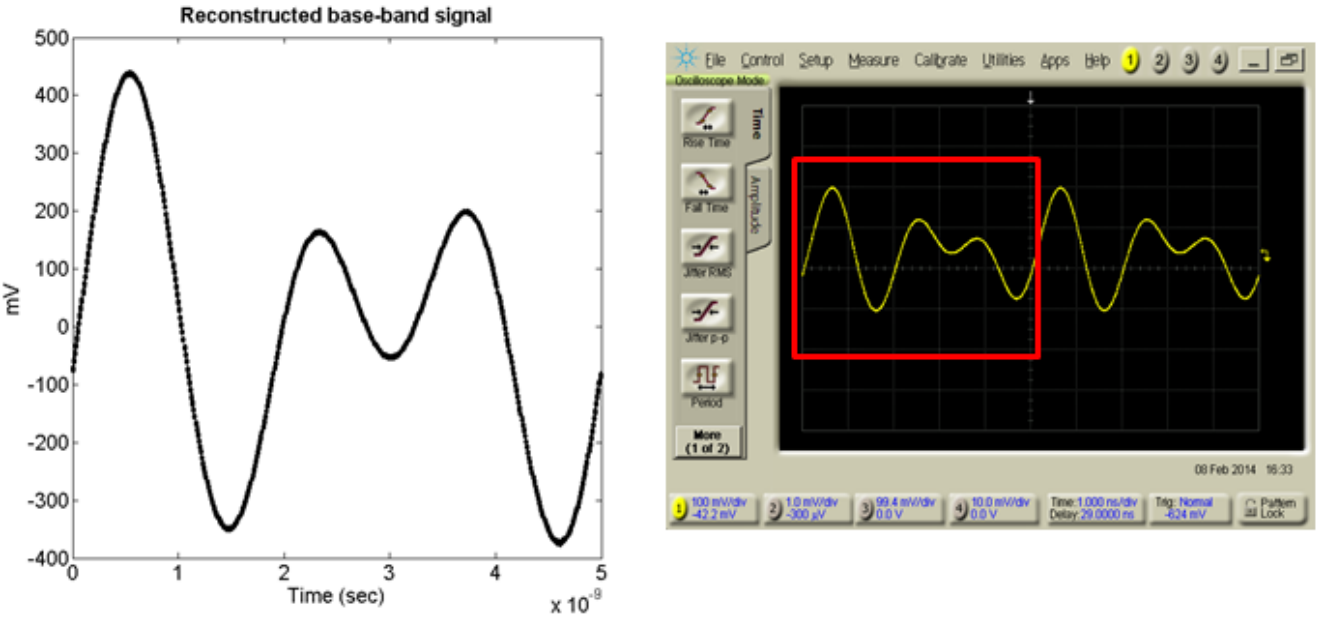

Figure 3.22. Baseband waveform reconstruction (left) vs. Baseband signal acquired with a 50 GHz bandwidth oscilloscope

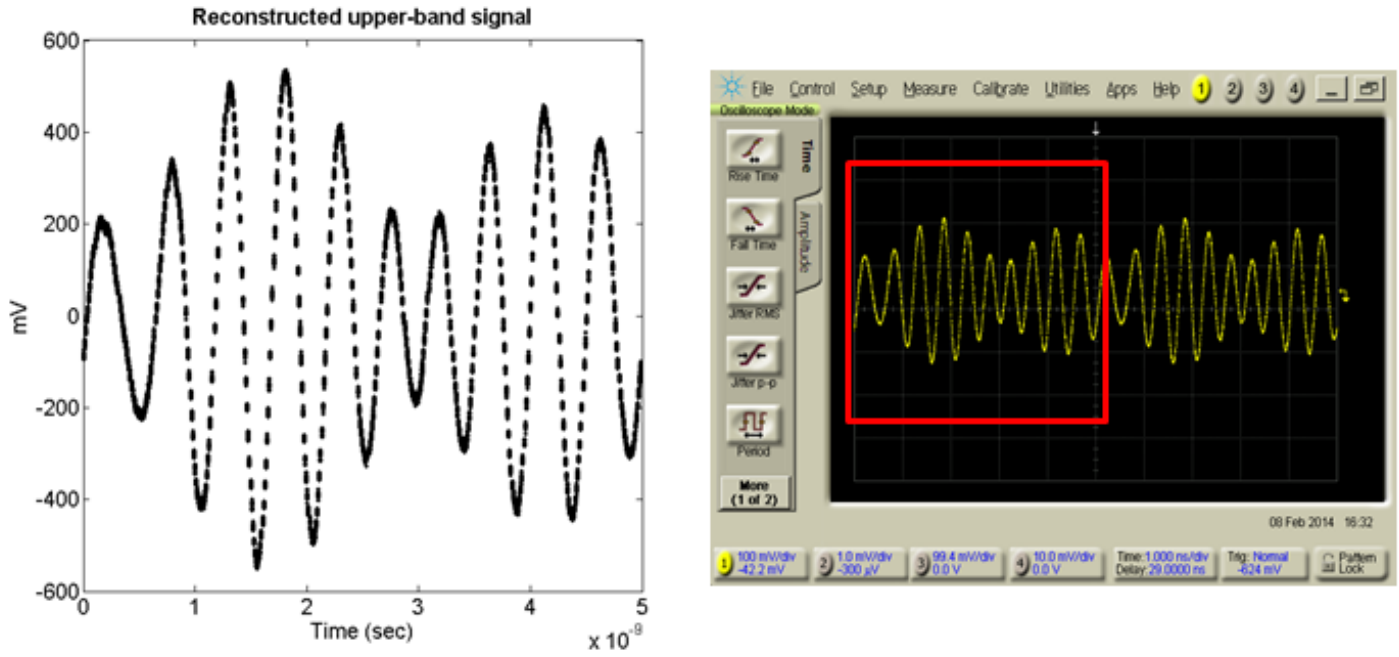

Figure 3.23. Upper-band waveform reconstruction (left) vs. Upper-band signal before mixer acquired with a 50 GHz bandwidth oscilloscope

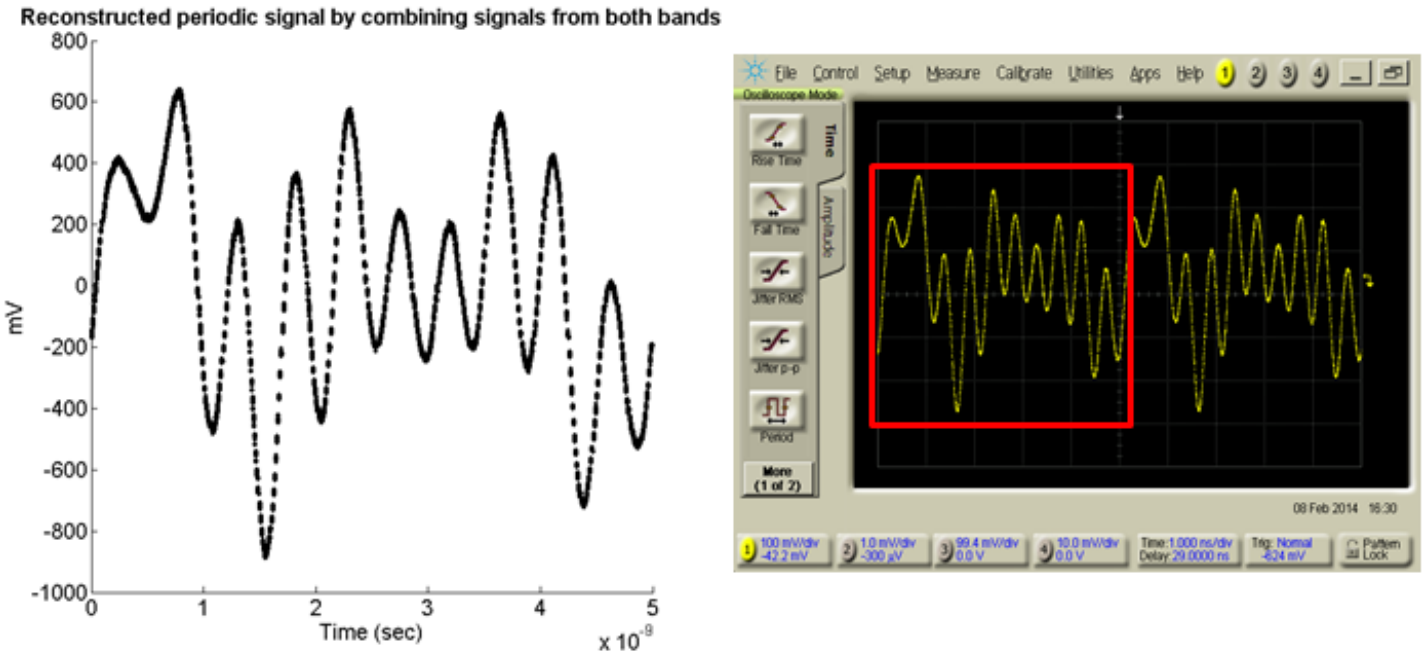

Figure 3.24. Input waveform reconstruction by combining baseband reconstruction and upper-band reconstruction

3.4 Summary

This chapter introduces low-cost time-domain waveform reconstruction techniques. Back-end signal processing techniques can reduce the hardware complexity by removing the required synchronization mechanism in traditional coherent measurement systems. Total variation is proposed and used to estimate the fundamental period for incoherent undersampling. Band-interleaved technique is later combined with the incoherent undersampling to further extend the input bandwidth. As the mixer is used in the band-interleaved system, associated signal processing algorithms are designed to enable the whole system. With band-interleaved technique to extend the input bandwidth and undersampling to reduce the sampling rate, the proposed system can be a low-cost solution for periodic signal waveform reconstruction.

CHAPTER 4

HIGH-SPEED SIGNAL JITTER MEASUREMENT AND CHARACTERIZATION

Jitter measurement is essential in high-speed signal characterization and input/output (IO) circuit testing. Periodic jitter measurement, separation, and characterization for circuit tuning are discussed in Section 4.1. Section 4.2 discusses crosstalk jitter separation in time-domain, which is the main contribution of this chapter.

4.1 Periodic Jitter Characterization and PLL Circuit Tuning with Incoherent Undersampling

Time interval error (TIE) analysis plays an important role in time-domain jitter analysis. In this section, TIE analysis is combined with incoherent undersampling. Three examples are used to show that characterizing and compensating for the periodic jitter can be used to improve the measurement result of incoherent undersampling.

4.1.1 Periodic Jitter Separation and Compensation for Digital Bit Sequences

The following example shows that compensating for the TIE of periodic jitter in digital bit sequences acquired by incoherent undersampling can result in better characterization for different types of jitter. In this hardware setup, an Agilent 81133A is used to generate a 2.5Gbps data pattern, and a 1MHz sine wave is applied to the output delay control as the periodic jitter. The eye diagram of the jittered input signal is shown in Figure 4.1. The period estimation error of incoherent undersampling can be calculated

by the slope of the regression line shown in Figure 4.2. The periodic jitter is extracted using the sinusoidal fitting, and the deterministic component of each sample is then compensated. After the jitter is compensated for, the whole-period PRBS is shown as in Figure 4.3. The eye diagrams at different steps are shown in Figure 4.4. The real jittered eye diagram is the eye diagram before compensation. Compensating out the periodic jitter makes it possible to measure the histogram of the random jitter and the peak-to-peak value of the periodic jitter separately. In addition, the potential gain in timing margin can be measured if additional circuitry is added to filter out the periodic jitter.

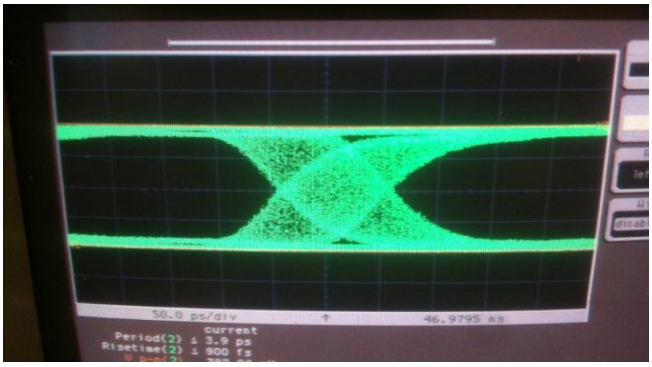

Figure 4.1. Eye Diagram of the input jittered PRBS signal

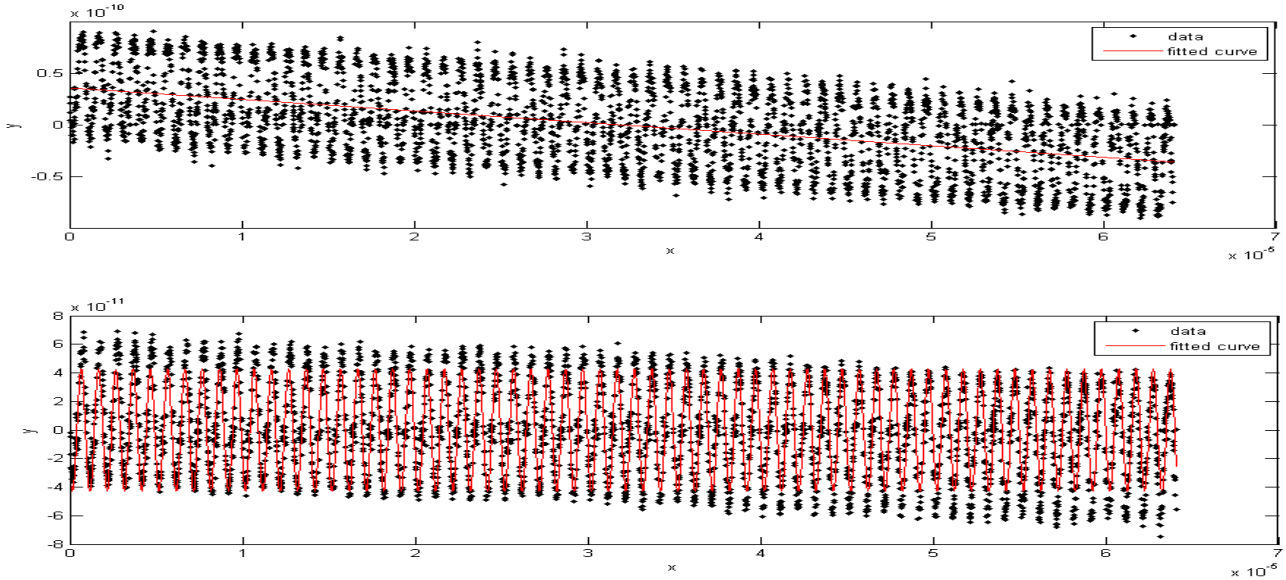

Figure4.2. Timing deviation and compensation of the input jittered PRBS signal

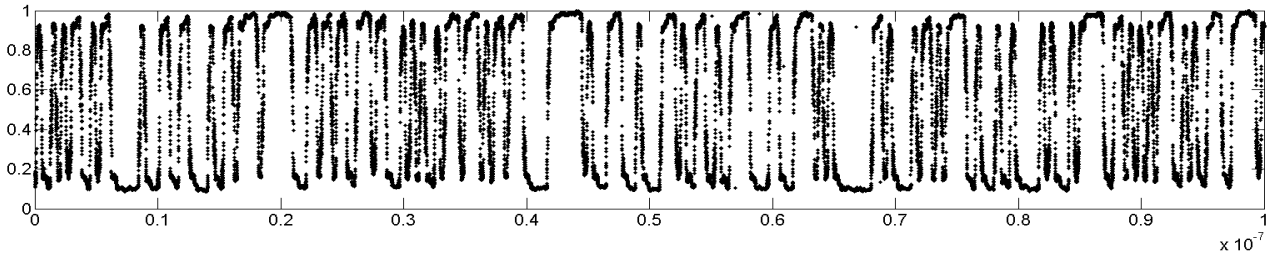

Figure 4.3. Reconstruction of the jitter compensated PRBS signal

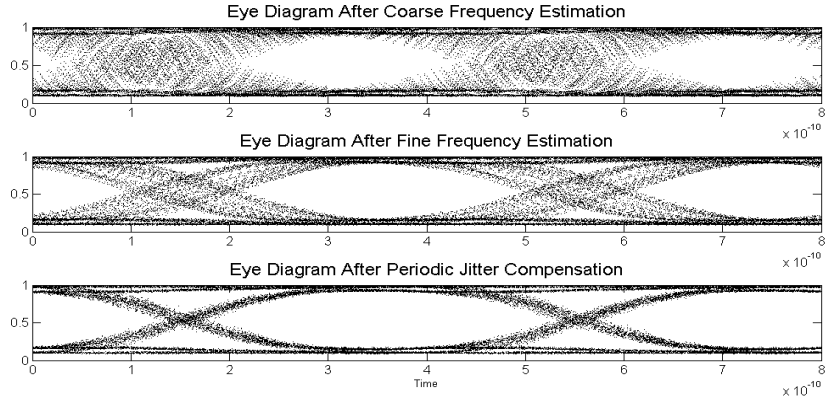

Figure 4.4. Reconstructed Eye Diagram in different stages

4.1.2 PLL Periodic Jitter Tolerance and Characterization Analysis

In this section, TIE analysis for incoherent undersampling is applied in order to test off-the-shelf PLL circuitry and explore the impact of two different noise sources on the PLL output signal. An LMX2531LQ1146E is used as the DUT in this test setup. The first noise source is a 20 KHz 100mv peak-to-peak sinusoid power supply noise, which is injected through the power supply. The frequency of the extracted periodic jitter is 20.441KHz. The jitter histogram before and after jitter compensation can be seen in Figure 4.5.

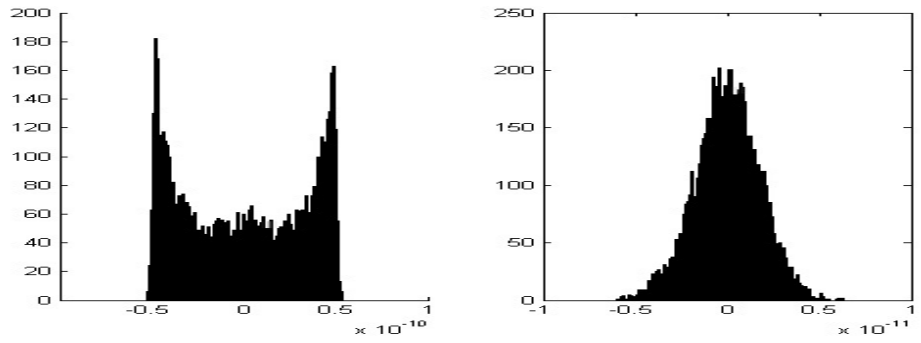

Figure 4.5. Jitter histogram before and after jitter separation. The noise is injected from the power supply.

The second external noise is injected through the reference clock port. In this experiment, the input reference clock is modulated with 0.1 rad and 50 KHz sinusoid. The frequency of the measured periodic jitter is 51.103 KHz. The jitter histogram before and after jitter compensation can be seen in Figure 4.6. The separated periodic jitter and the standard deviation of the random jitter are shown as Table 4.1. As can be seen from the table, due to the non-linear effect of the noise injection, the extracted random jitter of the test setup with noise injection is greater than that of the test setup without the noise injection.

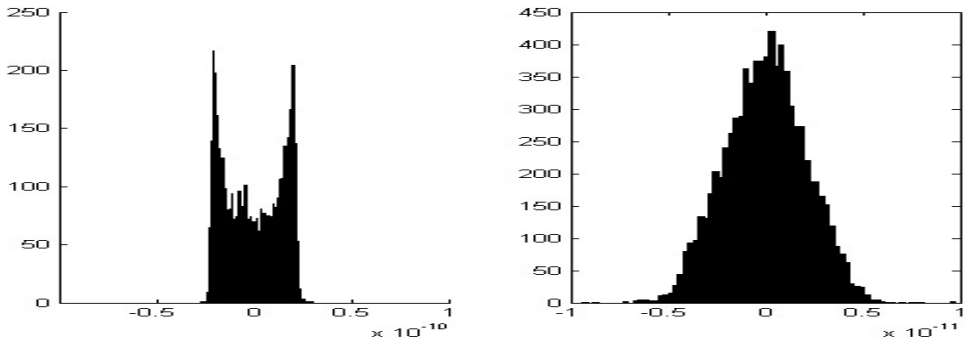

Figure 4.6. Jitter histogram before and after jitter separation. The noise is injected from the reference clock.

	Without Any Noise	Supply Noise	Ref. Clock Noise
Measured Peak-to-peak periodic jitter	0	47.87 ps	20.713 ps
Standard deviation of random jitter after removing deterministic jitter	1.3443 ps	1.7662 ps	2.1032 ps

Table 4.1. Measured periodic jitter and random jitter

4.1.3 Reference Spur Characterization for PLL Tuning

The experiment results in this section show that the information obtained from characterizing periodic jitter can be used for tuning a PLL. The conventional architecture of a PLL is shown in Figure 4.17, which includes a phase frequency detector (PFD), a charge pump (CP), a voltage-controlled oscillator (VCO), a loop filter, and feedback dividers.

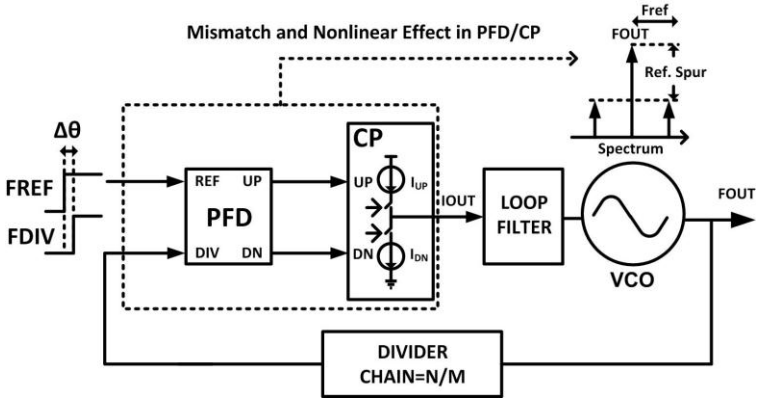

Figure 4.7. The reference spur of a conventional PLL includes the mismatch and nonlinear effect from PFD/CP.

Reference spurs arise because of the mismatch and nonlinear effect in the path from the PFD to the CP. A reference spur presents in the output signals as a deterministic periodic

jitter, which can be measured with specially designed sensors. The measurement result can be used as an indicator of the mismatch in the system to tune the PLL circuitry. Instead of using the specially designed sensors for the reference spur, it is possible to perform system tuning by characterizing the periodic jitter.

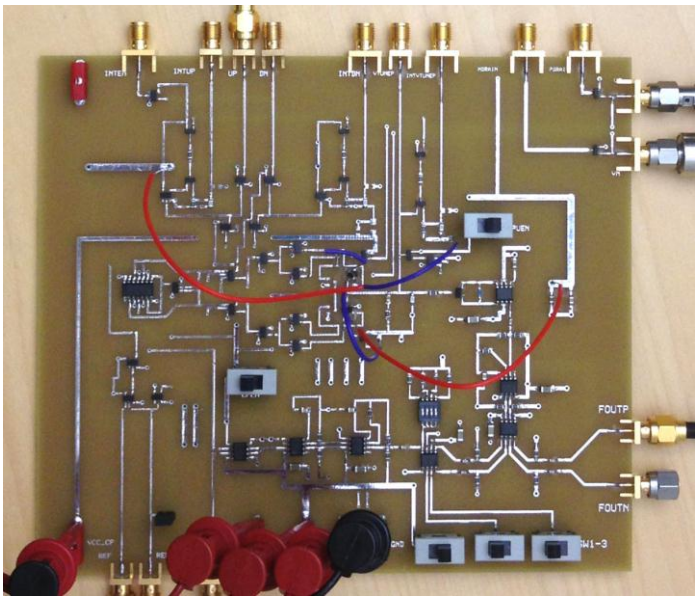

Figure 4.8. The PCB of PLL with tunable CP

A PCB of a PLL is implemented as shown in Figure 4.8. At the steady state, the reference spur can be adjusted by the CP current ratio. The PLL is locked at 224MHz with a 5.6 MHz reference clock. When the reference tone becomes objectively measureable, the corresponding static phase offset increases toward extreme directions as well. The waveforms of an optimal-matched and two unmatched static phase offsets (SPOs) are demonstrated in Figure 4.9. The performance of the reference spur is centered in the case with a matched SPO and degraded toward both one and the other direction.

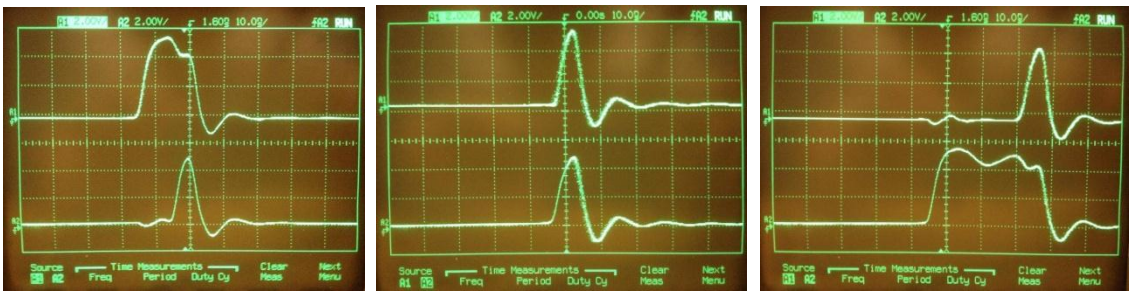

(a) (b) (c)

Figure 4.9. The waveforms of UP (top) and DN (bottom) pulses are shown in different cases: (a) The UP pulse is leading the DN pulse, (b) the UP and DN pulses are approximately matched, and (c) the UP pulse is lagging the DN pulse.

The time interval error of four different tuning settings is measured and reconstructed with incoherent undersampling. The separated periodic jitter and the associated jitter spectrum are shown in Figure 4.10 (a-d). The mismatch of the system can be tuned by changing the bias voltage of the PLL. Figure 4.10(a) (bias voltage = 3.86 V) and Figure 4.10(d) (bias voltage = 4.12 V) represent two extreme settings for the system, which give the two worst-case periodic jitter measurements. The optimal value exists between two extreme cases, which correlate with the design.

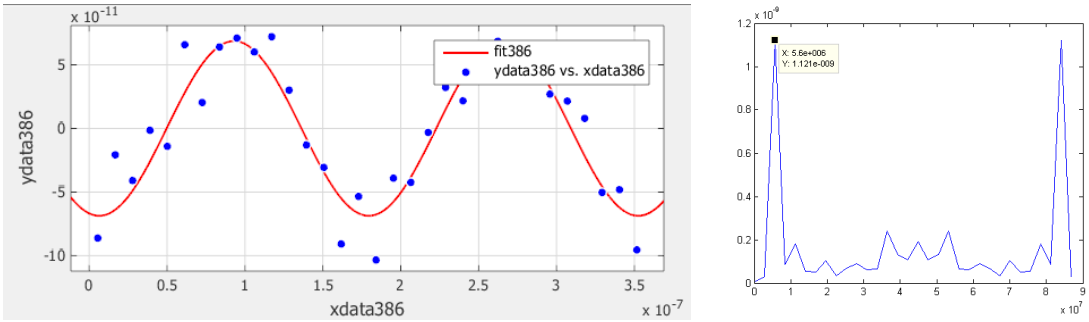

Figure 4.10 (a) Separated periodic jitter (bias voltage = 3.86V, extreme case)

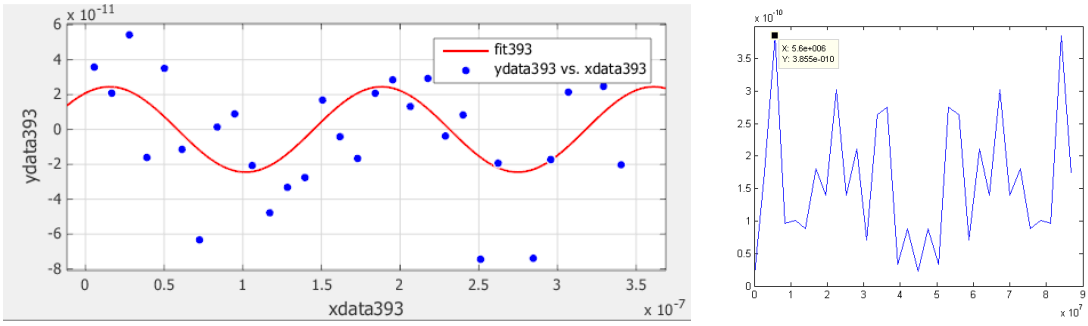

Figure 4.10 (b) Separated periodic jitter (bias voltage = 3.93V)

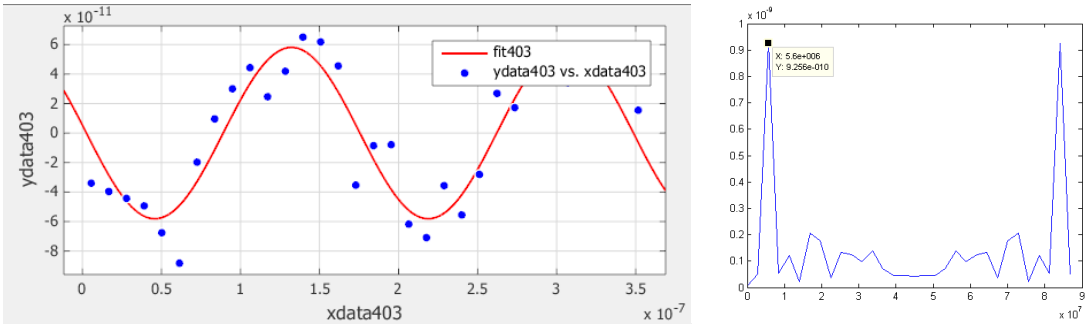

Figure 4.10 (c) Separated periodic jitter (bias voltage = 4.03V)

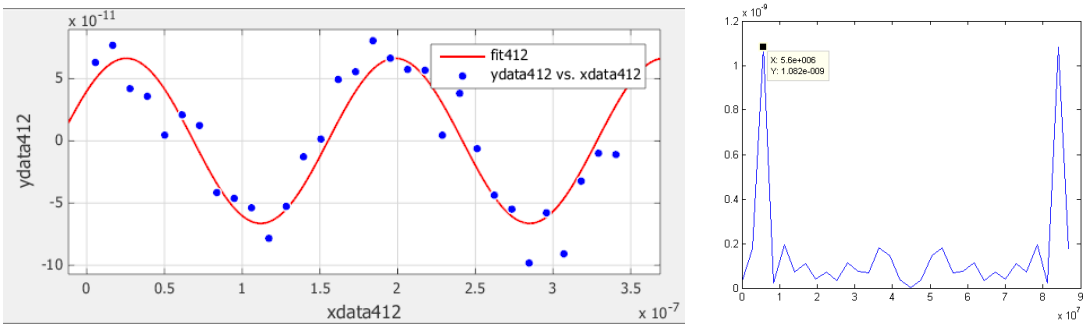

Figure 4.10 (d) Separated periodic jitter (bias voltage = 4.12V, extreme value)

The measurement result shows that the system information can be extracted by characterizing the jitter and noise. System tuning can be performed without redesigning or inserting sensor logics into the system.

4.2 Concurrent Multi-Channel Crosstalk Jitter Characterization Using Coprime Period Channel Stimulus

High-speed signals traveling on adjacent electrical interconnects suffer from signal degradation due to crosstalk coupling. Excessive crosstalk can result in timing uncertainties and "induced jitter". Figure 4.11 shows how different types of jitter can be classified.

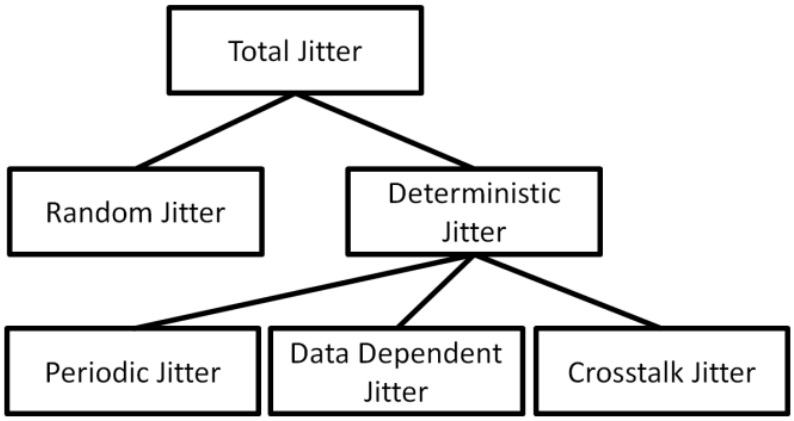

Figure 4.11 Jitter classification scheme

Total signal jitter consists of two components: random jitter and deterministic jitter. Random jitter is caused by device noise (e.g. thermal noise and flicker noise [68, 90]). Generally, the random jitter distribution includes contributions from Gaussian and non-Gaussian statistics [65], with Gaussian statistics being assumed in most practical cases. Deterministic jitter is composed of data-dependent jitter, periodic jitter and crosstalk jitter. Data dependent jitter can be further broken down into contributions from duty cycle distortion, which is caused by asymmetry in signal rise time and fall time, and inter-symbol interference, which is caused by the bandwidth limitations of the channel and

reflections due to impedance discontinuities and mismatch. In some printed wiring board layouts, such as those with meander delay lines, inter-symbol interference can also be caused by self-coupling [67]. Periodic jitter can be caused by multiple mechanisms. For example, periodic jitter can be caused by low-frequency power supply switching noise that couples to data and clock signal lines [91-94].

Crosstalk jitter, the key subject of this research, also called "bounded uncorrelated jitter," is caused by signals from *aggressor* channels coupling into *victim* channels. It is uncorrelated because there is no correlation between the signal transitions of physically close links [68]. It is bounded because of the finite range of the signal coupling effects. Crosstalk jitter can also be caused by switching noise coupled from the power and ground planes. The amount of crosstalk jitter depends on the aggressor data patterns, signal power, and coupling mechanisms between the aggressor and victim channel. As the speed of data links increases, the signal with a shorter rise/fall time can contain high frequency components which can easily couple into adjacent channels. In recent years, with the development of SoC technology, many serial standards have begun to mandate larger numbers of parallel interconnects to meet high(er) data transfer rate requirements. Under such operating conditions, every channel becomes both an aggressor and a victim. The crosstalk jitter problem is made worse by pre-emphasis and de-emphasis techniques [69]. These techniques boost the transmitted signal high-frequency components to compensate for signal attenuation due to limited data link bandwidth.

In general, different types of jitter occur simultaneously in signals. Therefore, there are different algorithms for separating and characterizing their individual contributions to total jitter. These measurement techniques can be classified into bit error

rate (BER) methods and sampling-based methods. Bit error rate methods monitor the available speed margins of high-speed links by transmitting known random sequences and calculating the bit error rate of the received signals. Some receiver designs allow sweeping the sampling time across the bit period or sweeping the reference voltage across a specified voltage range to monitor the received signal eye margin [95-97]. BER is a commonly used figure of merit for the quality of a communication system. Most application requires a 10^{-12} or lower BER from the high-speed interfaces. However, the time required to directly measure BER is significant and, hence, makes this approach expensive. Various accurate BER estimation methods have been proposed in the past for practical production test [98, 99]. It is important to note that bit error rate measurements do not directly yield jitter statistics but merely provide some guarantees of jitter stability since the two are strongly correlated in a statistical sense.

The other method for jitter measurement is based on direct sampling. Given a trigger or a reference signal, samples of high-speed signals from different bit periods are folded into one duty cycle to form eye diagrams or whole-period waveforms. Jitter histograms of the resulting eye diagrams are used to characterize different types of jitter. In most practical cases, random jitter is approximated by a Gaussian distribution. When multiple types of jitter are present in signals, the histogram forms more complicated distributions. In this situation, tail-fitting [66, 100] is used to characterize the distribution of random jitter. In addition to the jitter histogram, jitter information can be extracted from time interval error, which is the instantaneous phase variation from its ideal position with respect to the reference clock for each bit period. Analyzing the time interval error of edges can make it possible to analyze the effects of periodic and data-dependent jitter.

Periodic jitter can be compensated to simplify the jitter histogram [101]. A jitter spectrum can be obtained by taking the FFT of the time interval error data. Low frequency periodic and data dependent jitter are identified by the presence of specific tones in the jitter spectrum. Random jitter is characterized by the noise floor of the same jitter spectrum. A few high-end oscilloscopes are equipped with advanced jitter identification and tracking functions. However, few methods are available for separating and characterizing crosstalk jitter.

This work develops a methodology for determining the effects of crosstalk coupling from multiple active aggressors on a single interconnect embedded in a parallel lane of high-speed interconnects. The current research shows how such crosstalk effects on all the interconnects in the parallel lane can be determined from a *single data acquisition* using back-end signal processing algorithms.

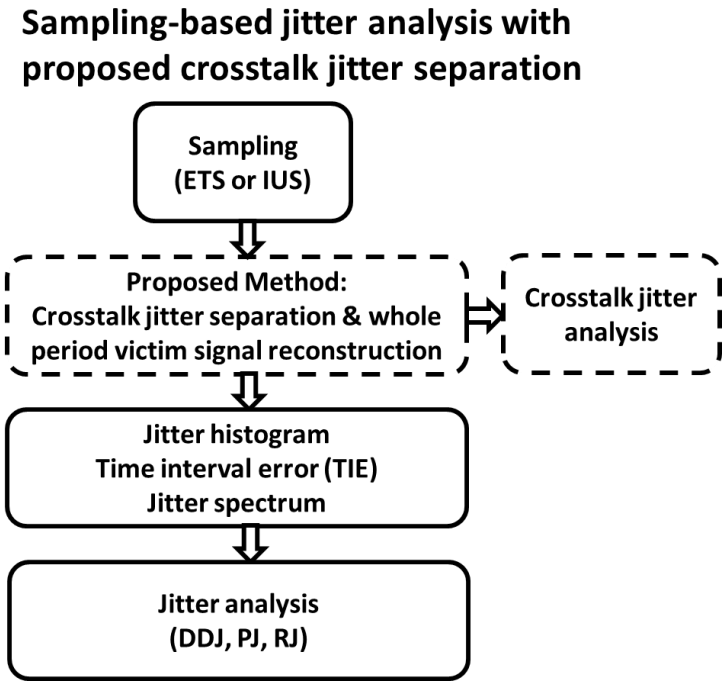

Figure 4.12 The proposed crosstalk jitter separation method can be inserted into the traditional jitter classification and analysis strategy.

Signals on each of the parallel lanes of signals in the presence of crosstalk coupling are first digitized using direct sub-Nyquist sampling and then analyzed. This analysis allows reconstruction of each of the signals in the parallel lane without the effects of crosstalk coupling under the constraint that the signals in each lane have coprime bit lengths. This makes it possible to determine the effects of crosstalk coupling on the jitter characteristics of each transmitted signal under multiple aggressors. The study shows that crosstalk components and victim signals with coprime bit periods can be determined by commercial oscilloscopes available on the market. Figure 4.12 shows how the crosstalk analysis algorithms (dotted box) can be inserted into traditional jitter classification strategies.

4.2.1 Problem Statement

Traditionally crosstalk effects are determined by transmitting data on a single channel and measuring crosstalk-induced signals on adjacent channels. The number of tests, therefore, grows linearly with the number of channels, increasing test time significantly. In the approach presented here, all the channels are stimulated concurrently with bit sequences of a coprime period. Each channel is digitized concurrently using direct Nyquist rate sampling or incoherent undersampling [60-64, 81]. The data from all channels is fed to the analysis algorithm given in Figure 4.13, which determines the crosstalk-free signals on each line as well as the respective crosstalk "noise." The constraint of the algorithm is that each channel stimulus is a bit sequence with different coprime periods. It is important to note that the proposed method is independent of the bit

patterns. The bit patterns can be chosen arbitrarily as long as they sitimulate the desired crosstalk effect.

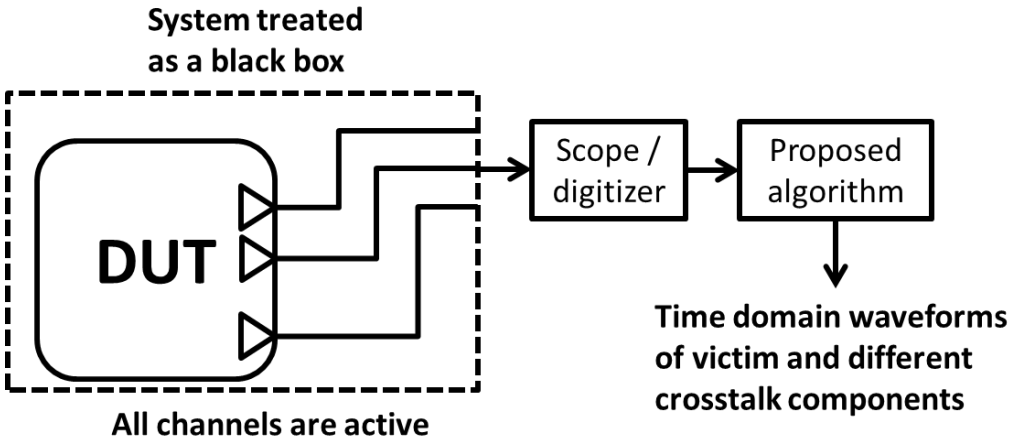

Figure 4.13 Proposed crosstalk jitter separation algorithm application scheme

4.2.2 Coprime Bit Sequence Stimulus-Based Crosstalk Analysis

On each output channel in Figure 4.13, the digitized signal consists of superposed signals consisting of the signal transmitted on that line and signals coupled onto the line from aggressor lines. The signals coupled onto a line have the same period as the signals transmitted on the corresponding aggressor lines. Let

$$s(t) = l_m(t) + l_n(t)$$

$l_m(t)$ and $l_n(t)$ are periodic signals with period mT and nT, respectively, where m and n are coprime integers.

$$l_m(t) = l_m(t + mT)$$

$$l_n(t) = l_n(t + nT)$$

$l_m(t)$ represents the original signal transmitted on the line, and $l_n(t)$ represents the signal that is coupled onto the line by an aggressor on which a signal of period nT is being

transmitted. The superposition of the two signals is a periodic signal $s(t)$ with period mnT. Over the time duration mnT, the signal $l_m(t)$ is repeated n times, and the signal $l_n(t)$ is repeated m times. Suppose $s(t)$ is sampled, and the samples are folded into period mT. We assume, for simplicity, that coherent Nyquist rate sampling is used, where coherence is established over the period mnT of the signal $s(t)$. For all $t \geq mT$, the folding operation maps the corresponding time points into the range $1 \leq t \leq mT$ with all values centered within a small time interval of some phase t' ($0 \leq t' \leq mT$) being averaged. Let $S_{t'}^{mT}$ be a set of sampling time falling close to t' after the folding operation. That is,

$$S_{t'}^{mT} = \{\, t \mid t' - \frac{1}{2}\Delta t \leq mod(t, mT) \leq t' + \frac{1}{2}\Delta t \,\}$$

Suppose there are N samples with sampling time in $\Lambda_{t'}^{mT}$. Then the average of N samples can be expressed as

$$\frac{1}{N}\sum s\left(t \middle| t \in S_{t'}^{mT}\right)$$

Given that Δt is small and $Z_i \in \mathbb{N}^+(positive\ integers)$, the average value can be approximated as

$$\frac{1}{N}\sum s\left(t \middle| t \in S_{t'}^{mT}\right) \approx \frac{1}{N}\sum_{i=1}^{N} s(t' + Z_i mT)$$

$$= \frac{1}{N}\sum_{i=1}^{N} l_m(t' + Z_i mT) + l_n(t' + Z_i mT)$$

$$= \sum_{i=1}^{N} \frac{l_m(t' + Z_i mT)}{N} + \sum_{i=1}^{N} \frac{l_n(t' + Z_i mT)}{N} \quad (Eq.1)$$

$t' + Z_i mT$is the original sampling time before the folding operation. $l_m(t)$ is a periodic signal with period mT.

$$mod(t' + Z_i mT, mT) = t'.$$

Given small Δt, $l_m(t' + Z_i mT)$ are close to $l_m(t')$ for all integers Z_i and all phases t'. $Eq.1$ can be rewritten as follows:

$$\frac{1}{N}\sum s(t|t \in S_{t'}^{mT}) = l_m(t') + \sum_{i=1}^{N} \frac{l_n(t' + Z_i mT)}{N} \quad (Eq.2)$$

$l_n(t)$ is a periodic signal with period nT

$$mod(t' + Z_i mT, nT) = t' + mod(Z_i m, n)T$$

$Eq.2$ can be simplified by letting Z_i be N consecutive integers. Since the numbers n and m are chosen to be coprime, $mod(Z_i m, n)$ generates numbers evenly from a set $Y = \{0, 1, 2, \dots, n-1\}$ periodically with period n. In other words, for $Z_i = 1, 2, \dots, N$ and $N > n$, the numbers generated by $mod(Z_i m, n)$ traverse all numbers in Y once before repeating. This is a property of two coprime numbers. The order of the generated number depends on the two coprime numbers. The second term of $Eq.2$ can be written as the following:

$$\sum_{i=1}^{N} \frac{l_n(t' + Z_i mT)}{N} = \sum_{i=1}^{N} \frac{l_n(t' + mod(Z_i m, n)T)}{N} = \sum_{i=1}^{N} \frac{l_n(t' + iT)}{N}$$

This is the same as sampling $l_n(t)$ at the same phase of each bit period and averaging acquired N consecutive samples. Since T is the bit period, the samples are collected at the same phase of every bit interval. It is important to note that if the two sequences are not coprime, $mod(Z_i m, n)$ does not traverse all numbers in Y. Hence the collected samples are only from the same phase of certain bit intervals and, thus, biased.

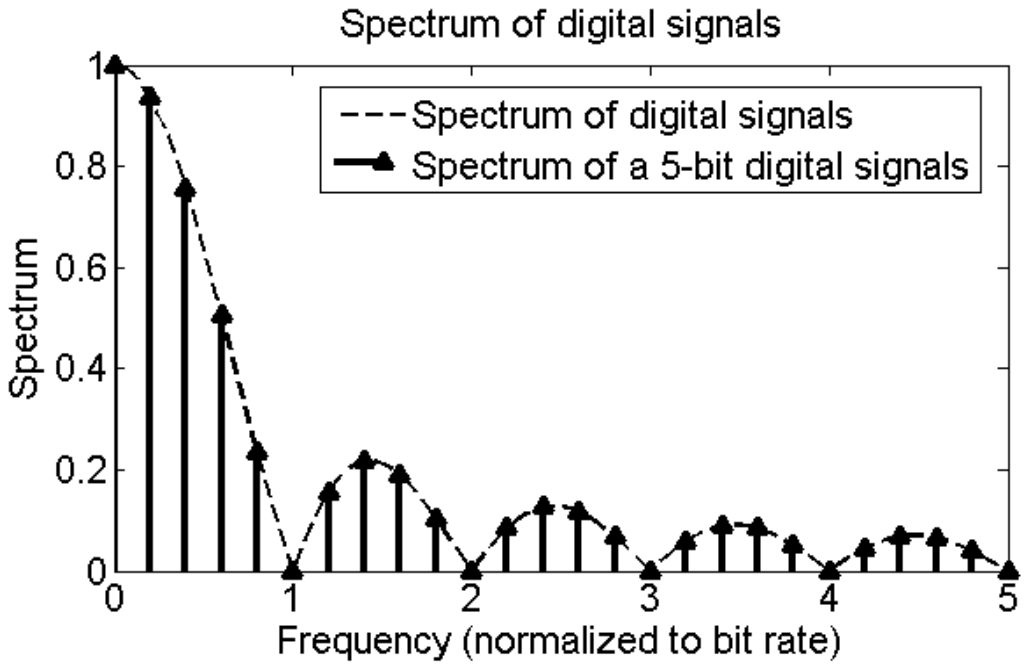

Figure 4.14 Spectrum of an ideal digital signal and an ideal 5-bit digital signal

Averaging the samples is equivalent to subsampling $l_n(t)$ wth sampling frequency $\frac{1}{T}$ and calculating the DC term using these samples. The DC term consists of the actual DC and the spectral components at frequency $\frac{k}{T}, k \in \mathbb{N}^+$. The shape of the spectra of ideal digital bit sequences is a sinc function with zero-crossing nodes at frequency $\frac{k}{T}, k \in \mathbb{N}^+$. An ideal $N - bit$ periodic bit sequence consists of multiple tones with equal frequency-spacing $\frac{1}{NT}$ and a spectral magnitude corresponding to the magnitude of the sinc function, as shown in Figure 4.14. The spectral power at frequency $\frac{k}{T}, k \in \mathbb{N}^+$, is small for digital signals. Therefore, the second term of $Eq.2$ becomes just the DC term of $l_n(t)$, and the value of the second term does not change with t'. For arbitrary phase t' in mT, the value is a constant, which is the DC term of $l_n(t)$. When incoherent undersampling is used to collect samples of $s(t)$, $mod(Z_i m, n)$ generates

numbers from 0 to $N-1$ almost evenly and randomly from set Y. This makes the second term close to a constant with a large number of samples N.

In reality, the shape of the spectra of digital signals is not exactly a sinc function. However, the energy at frequency $\frac{k}{T}, k \in \mathbb{N}^+$ is relatively low unless the duty cycle is distorted and the spectral energy at the harmonic of the bit rate, which corresponds to the zero-crossing node of the sinc function, is high. In conclusion, with coprime periodic sequences, given samples of a signal with crosstalk jitter, different periodic components can be extracted by folding samples into different periods and averaging them. After all periodic components are extracted, jitter separation can be performed by subtracting periodic aggressor components from the samples. Other jitter characterization techniques can then be applied on the post-processed samples without any crosstalk effect. It is important to note that the jitter separation algorithm is not affected by the bit pattern of each channel. Although the pattern can be chosen arbitrarily in the algorithm, choosing the proper aggressor patterns is important in worst-case crosstalk jitter analysis. Figure 4.15 is a summary of the proposed periodic component reconstruction method, which is stated in the next section.

4.2.3 Proposed Method

The flow graph of the proposed algorithm is shown in Figure 4.15. The device under test (DUT) generates N different bit sequences with coprime periods for N different output channels, and the signal of one of the sequences is digitized. In Figure 4.15, the signal of channel 2 is digitized, so channel 2 is the victim channel, and all other

channels are aggressors. The samples are then folded into the period of one of the bit sequences and averaged for the corresponding periodic component.

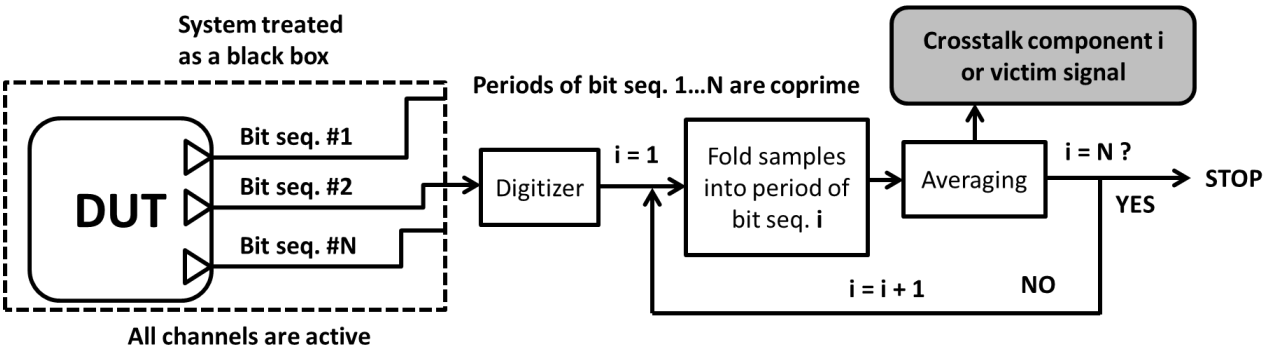

Figure 4.15 Proposed crosstalk jitter separation method. In this example, the victim signal is from channel 2, and the crosstalk components are from all other channels.

The ways to fold the samples are different depending on the sampling scheme. In an equivalent time sampling scheme, which is used for some oscilloscopes, folding the samples is done by triggering the scopes with the period of the bit sequence. The trigger signal of a periodic sequence is the integer multiple of the bit period, and it can be generated by counting the data clock. In an incoherent undersampling scheme, the fundamental period of the victim channel is first estimated using time domain techniques [26] or frequency domain techniques [25]. The periods of other periodic sequences can be calculated by using the ratio of coprime numbers, and samples are folded into these calculated periods. Hardware measurement using these two different sampling schemes is demonstrated in a later section.

After the samples are folded, the waveform is averaged, and the corresponding periodic component can be extracted. Suppose N different stimuli are used and that this

process of folding and averaging is repeated N times to extract N different periodic components from each output channel. With the proposed method, the impact of different periodic components from different channels can be determined by a single data acquisition and the proposed post-processing. In total, only N data acquisitions are needed to characterize crosstalk coupling of N different channels. Compared to the traditional characterization method, which requires N^2 data acquistions, the proposed method reduces test time by a factor of N. Different crosstalk components can be subtracted from the original samples, and other jitter analysis techniques, such as jitter histogram analysis, can be applied. The averaged victim waveform can be used for data-dependent jitter analysis, and the averaged crosstalk components can be used to determine the coupling effect between different channels.

4.2.4 Crosstalk Jitter Separation – Simulation

The proposed simulation model is shown in Figure 4.16. A 16-bit aggressor signal is passed through a band-pass filter and superimposed on a 31-bit victim signal.

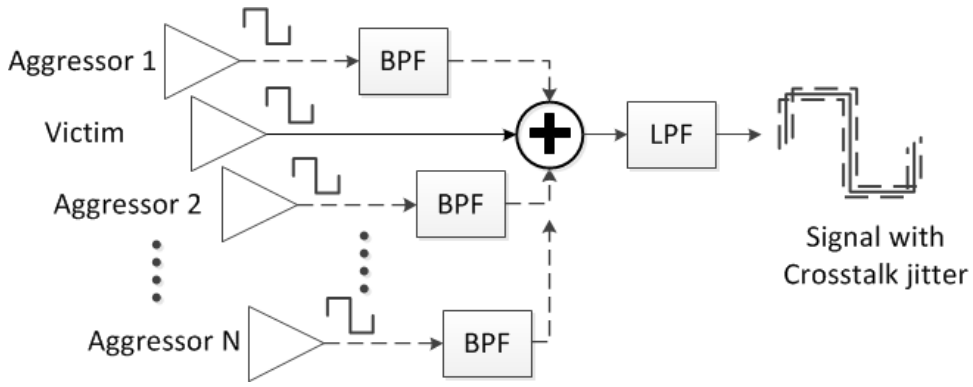

Figure 4.16 Crosstalk jitter coupling model

This noisy signal is digitized, and the samples are folded into the victim signal period, as shown in Figure 4.17. 16 (aggressor period) and 31 (victim period) are coprime. The

signal is divided into multiple intervals, and the samples are averaged within each small interval. In Figure 4.18, the original jitter-free victim signal is shown as black dots, and the average value in each interval is marked as red dots. As shown in Figure 4.18, the average values are almost the same as those of the original jitter-free victim waveform. Then, the first periodic deterministic component, the victim signal, is subtracted from the samples. Then the residual is folded into the aggressor period and the average is taken. In Figure 4.19, the original aggressor signal is shown as black dots, and the average value of the residual in each interval is marked as red dots.

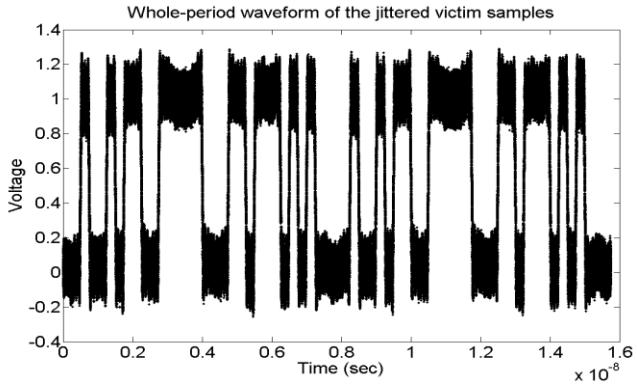

Figure 4.17 Waveform of the jittered samples folding into victim period (simulation)

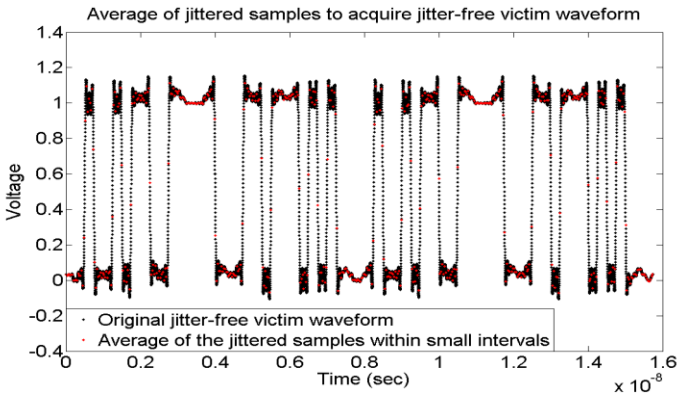

Figure 4.18 Acquiring a deterministic jitter-free victim waveform by averaging samples in small time intervals (simulation)

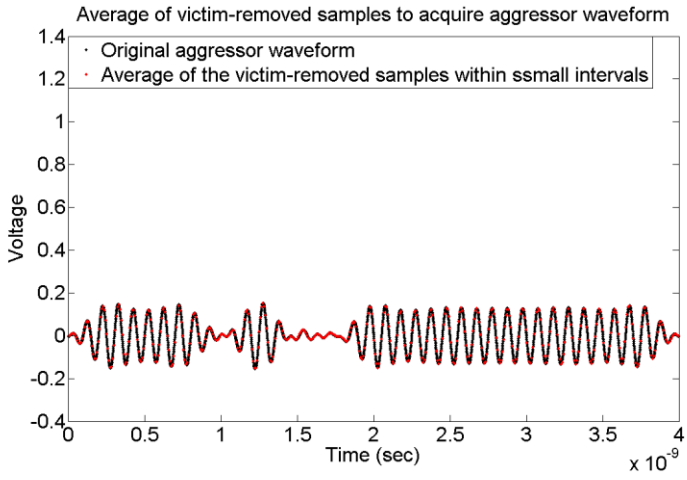

Figure 4.19 The victim signal is subtracted from the samples, and the residual is folded into the aggressor period (simulation)

In this example, the victim component is the first extracted component and is followed by the aggressor component. However, the order can be reversed. Two periodic components are extracted in this example. If there are multiple periodic components, all of the components can be extracted repeatedly. After all the crosstalk components are extracted, the crosstalk jitter components can then be subtracted from the original samples. The eye diagram after the crosstalk component is subtracted, is shown as Figure 4.20. Subtracting the crosstalk effect from the samples can simplify the analysis of other types of jitter. Figure 4.21 shows the jitter histogram before and after the crosstalk jitter is removed. Before the crosstalk component is subtracted, the histogram contains multiple types of jitter and has a more complicated distribution. After crosstalk jitter subtraction, the histogram is close to a Gaussian distribution. As the number of samples increases, the average error of the waveform obtained by averaging decreases. As shown in Figure 4.22, under different signal-to-noise-ratios (SNRs), the average error decreases as the total

number of acquired samples increases. It is important to note that as the length of each sequence increases, more samples are required to average out the residual.

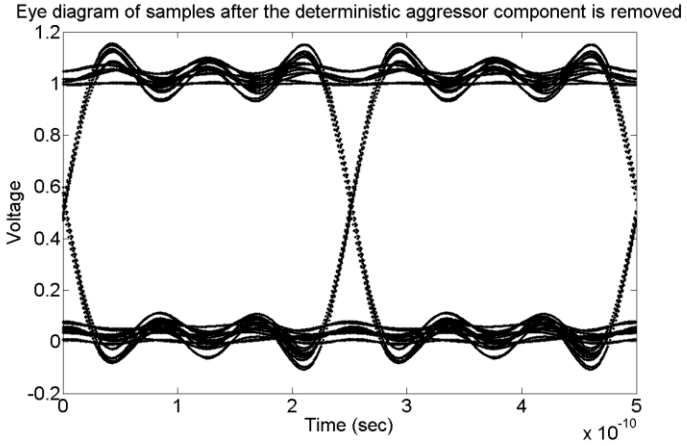

Figure 4.20 Eye diagram of the samples after removing crosstalk jitter (simulation)

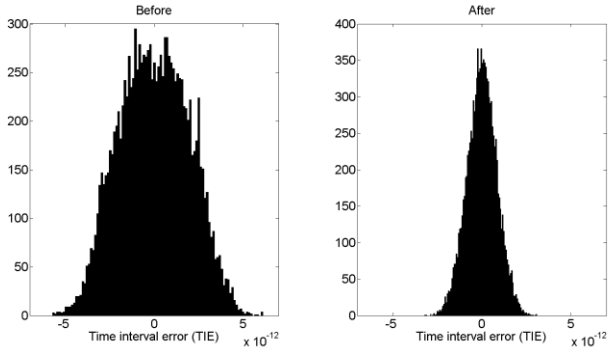

Figure 4.21 Jitter histogram before (left) and after (right) removing crosstalk jitter (Simulation)

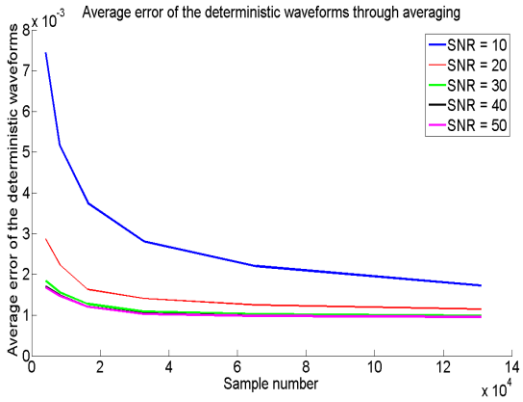

Figure 4.22 The average error decreases as the number of samples increases

4.2.5 Hardware Measurement: Two Channel Crosstalk Jitter Separation

Injecting the crosstalk jitter required the designing of a a board with two traces to couple the high frequency components of signals from one link to another, as shown in Figure 4.23. The GTX pins of a Xilinx ML605 FPGA evaluation board are programmed to generate a 3Gbps 16-bit periodic sequence as the victim signal. An Agilent 81133A is used to generate a 3Gbps 31-bit PRBS signal as the aggressor signal. The jittered signal can be observed with an oscilloscope from the other end of the crosstalk jitter injection board, as shown in Figure 4.24. A National Semiconductor ADC12D1800 evaluation board is used to sample the signal at 511 Msps, and the incoherent undersampling algorithm described in Section II is used to reconstruct the signal with crosstalk jitter and average the signal, as shown in Figure 4.25. The signal that is obtained after the average waveform is subtracted is shown in Figure 4.26. The current period is still the period of the victim, not the period of the aggressor. The correct waveform of the crosstalk jitter is obtained by folding the signals into the aggressor period, as shown in Figure 4.27. The victim signal that results after the crosstalk jitter is separated is shown in Figure 4.28. Note that with the proposed method, turning off the victim or the aggressors is not required. However, determining how effective the separation method is requires first turning off the aggressor and seeing the waveform of the victim signal before injecting any jitter by using the oscilloscope. The victim signal is also turned off, and the spectrum of the crosstalk jitter is measured. Then, FFT is applied to the average jitter waveform in Figure 4.28 to see the spectrum of the victim signal. With only one period of the average spectrum, the resolution is limited. The periodic signal in Figure 4.29 is folded by half

since the oscilloscope can be triggered only by a 1.5 GHz clock. The eye diagram before and after jitter separation can be seen in Figure 4.30.

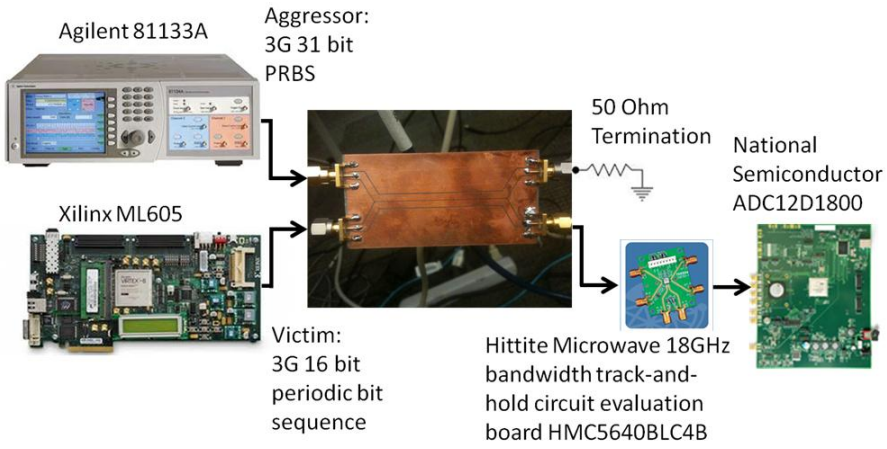

Figure 4.23 Crosstalk jitter separation experiment setup

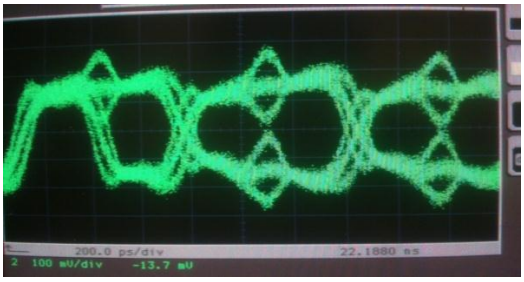

Figure 4.24 Periodic signal with crosstalk jitter

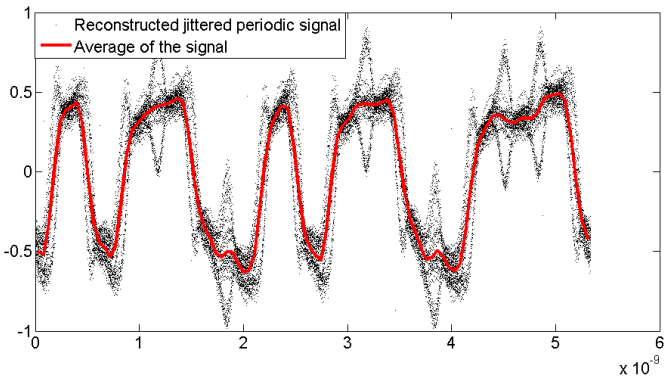

Figure 4.25 Reconstructed periodic signal with crosstalk jitter

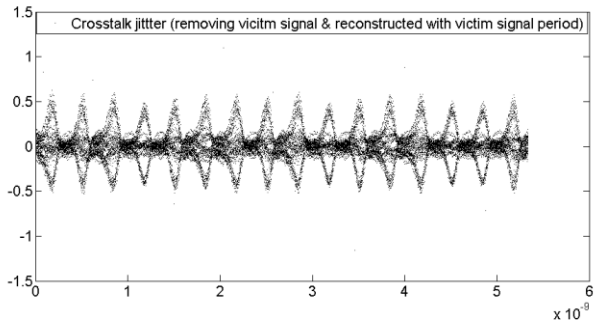

Figure 4.26 Crosstalk jitter waveform by folding the samples into victim period

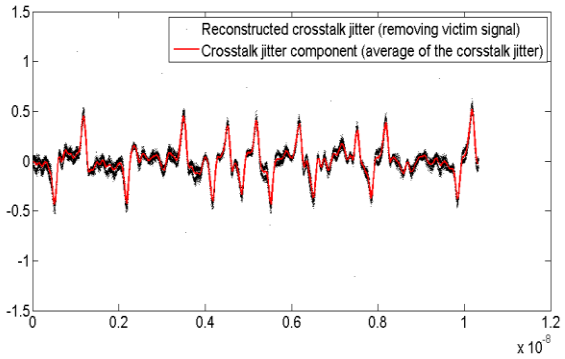

Figure 4.27 Crosstalk jitter waveform by folding the samples into crosstalk period

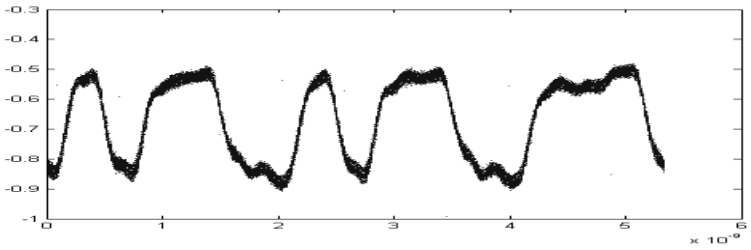

Figure 4.28 Victim signal after crosstalk jitter is separated

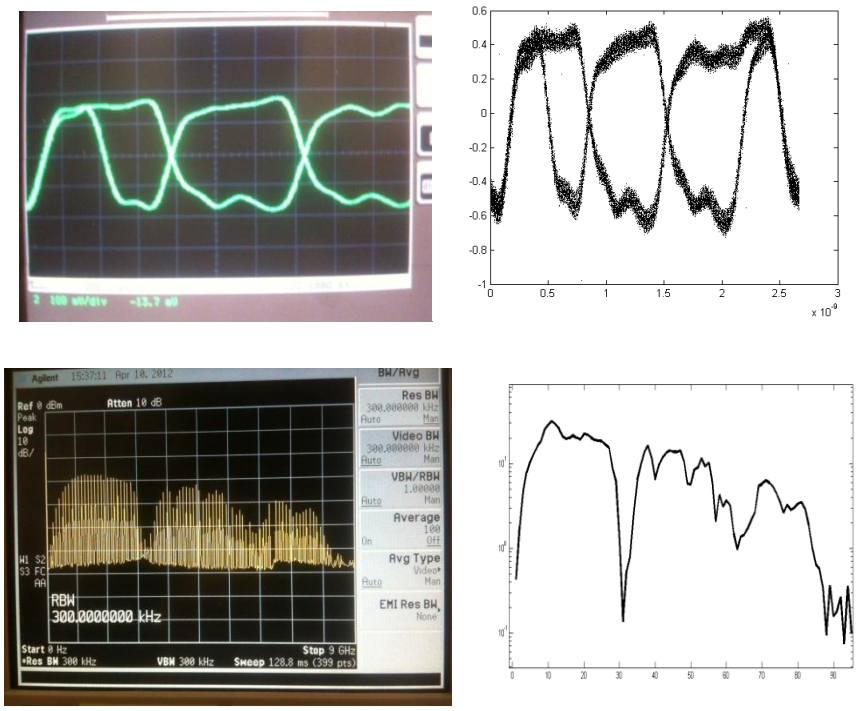

Figure 4.29 Victim signal after the crosstalk jitter is separated

Left: Jitter spectrum of the victim signal (with aggressor turned off)

(Turning off the aggressor)

Right: Victim signal and crosstalk jitter spectrum by the proposed method

(Aggressor link is still active)

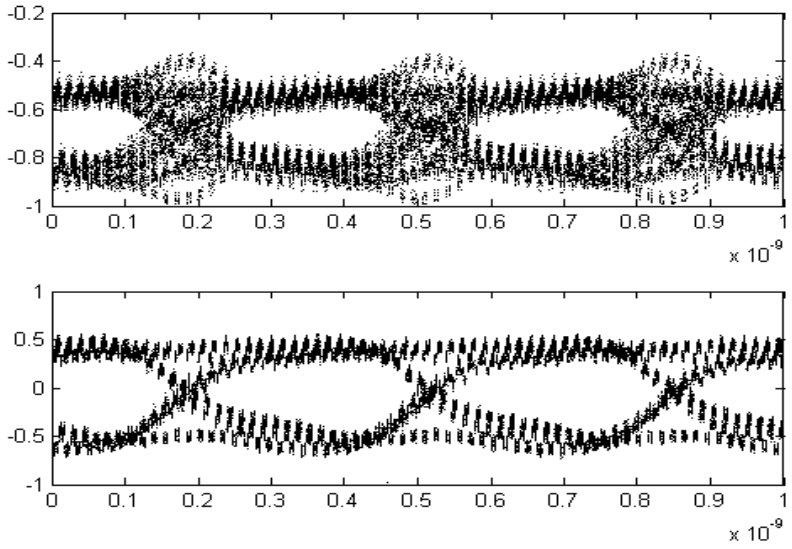

Figure 4.30 Eye diagram before and after the crosstalk jitter is separated

4.2.6 Hardware Measurement: Multi-Channel Crosstalk Separation and Characterization with Incoherent Undersampling

This section provides the hardware measurement in support of the proposed technique. Three synchronized sources (two aggressors and one victim signal) are used to generate three different coprime bit patterns. An ML605 Virtex-6 Evaluation board is used to generate a 3.2Gbps 16-bit period signal as the first aggressor source. A KC705 Kintex-7 Evaluation board is used to generate a 3.2Gbps 127-bit pseudo-random bit sequence (PRBS) as the victim signal. An Agilent 8113A signal generator is used to generate a 3.2Gbps 31-bit PRBS as the second aggressor source. 16 (period of the first aggressor), 127 (period of the victim), and 31 (period of the second aggressor) are coprime numbers.

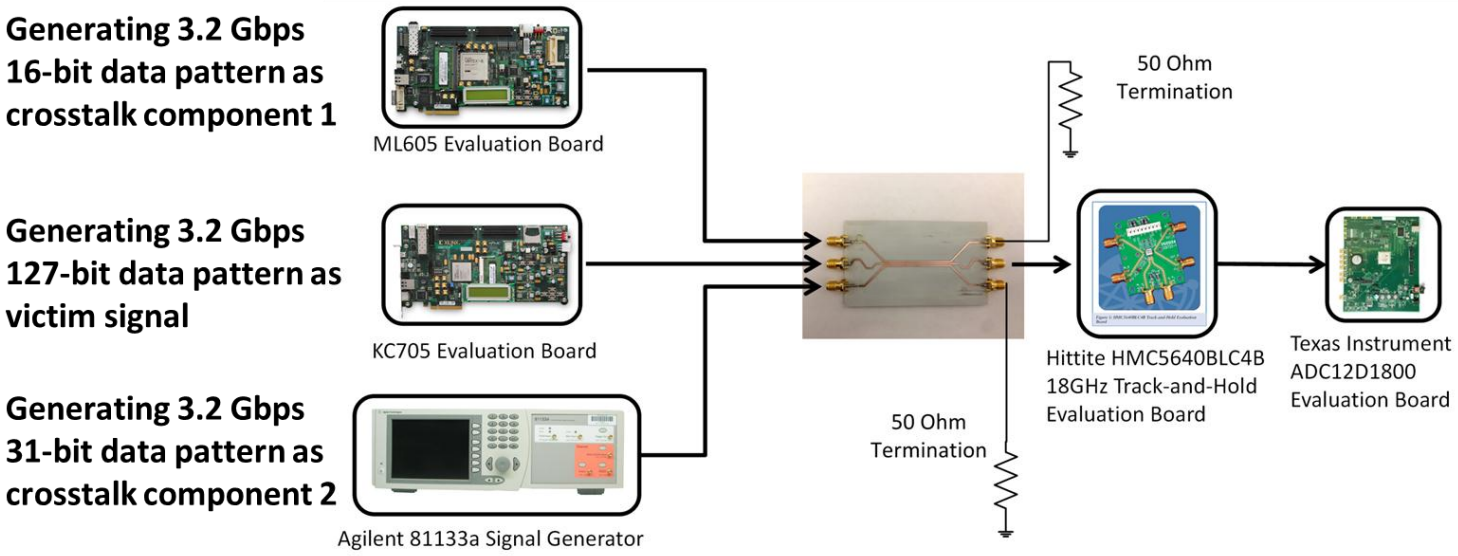

Figure 4.31 Hardware verification setup

These three digital signals are passed through a customized PCB board with very close traces to intentionally couple the “noise” from one to another. The traces are matched at 50Ω. In the proposed method, the whole system, which includes data generation and the coupling of crosstalk channels, is treated as a black box. The victim signal is then digitized by the Texas Instruments ADC12D1800 evaluation board. The Hittite HMC5640BLC4B 18GHz track-and-hold circuit evaluation board is used to increase the input bandwidth of the digitizer. The clock phase between the ADC and the track-and-hold circuit is synchronized and adjusted so that the ADC samples at the hold-phase of the track-and-hold circuit. The system setup is shown in Figure 4.31, and the eye diagram of the jittered signal is shown in Figure 4.32.

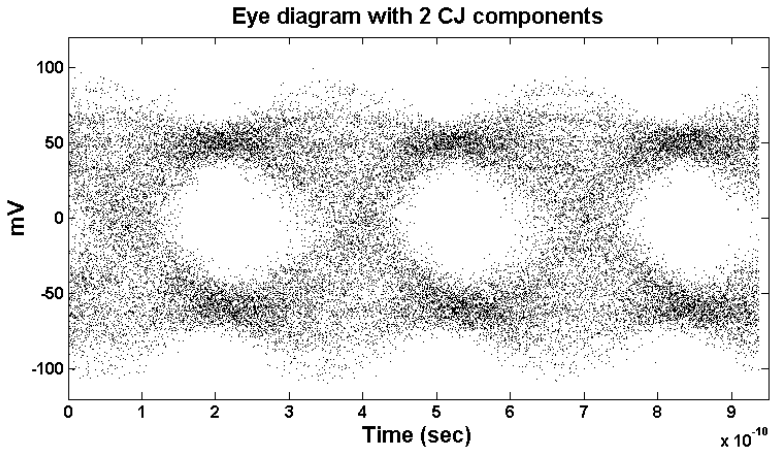

Figure 4.32 Eye diagram of a jittered victim signal with samples of ADC

With a single capture of the victim channel and with all data links operating, the proposed method is used to extract the victim and the two aggressor waveforms. One advantage of incoherent undersampling is that the folding operation is done in digital domain;

therefore, different trigger signals do not need to be generated. An equivalent time sampling scheme requires generating different trigger signals, which is done by calculating the data clock. Figure 4.33 shows the averaged victim waveform, which can be used for data-dependent jitter analysis.

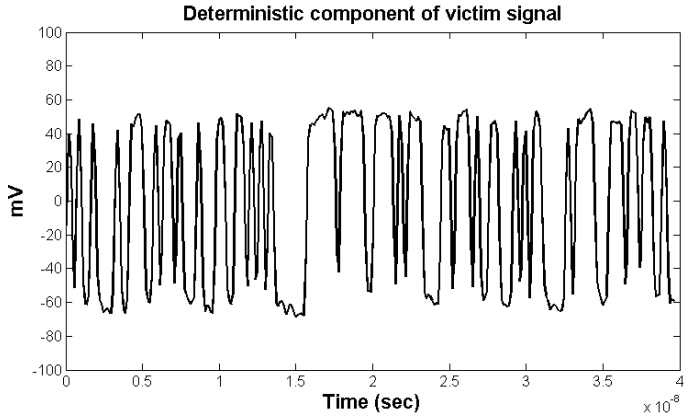

Figure 4.33 Victim signal obtained through averaging

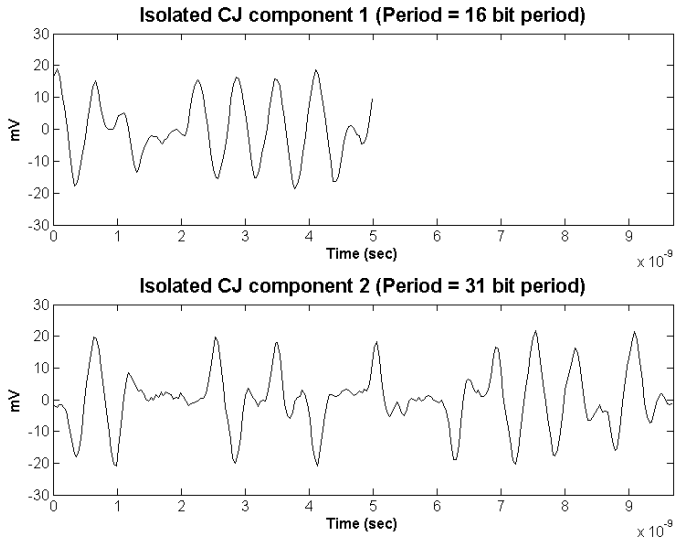

Figure 4.34 Extracted crosstalk components

The waveforms of the two aggressors are shown in Figure 4.34, which reveals that crosstalk component 2 has sharper peaks than component 1. This is caused by the fact

that the Agilent 8113A signal generator is able to achieve faster rising and falling times and contains more high-frequency components. The maximum value of the peak gives the maximum voltage perturbation to the victim signal. The crosstalk jitter can be compensated in digital domain by subtracting the crosstalk components from the original samples. The waveforms before and after jitter compensation are shown in Figure 4.35, and the eye diagram after crosstalk jitter compensation is shown in Figure 4.36. The effectiveness of the proposed method is shown in the jitter histogram before and after crosstalk jitter subtraction in Figure 4.37. As can be seen from Figure 4.37, the histogram after jitter compensation can be better approximated by a Gaussian distribution function. Analyzing random jitter using these samples is thus more effective than using the original samples.

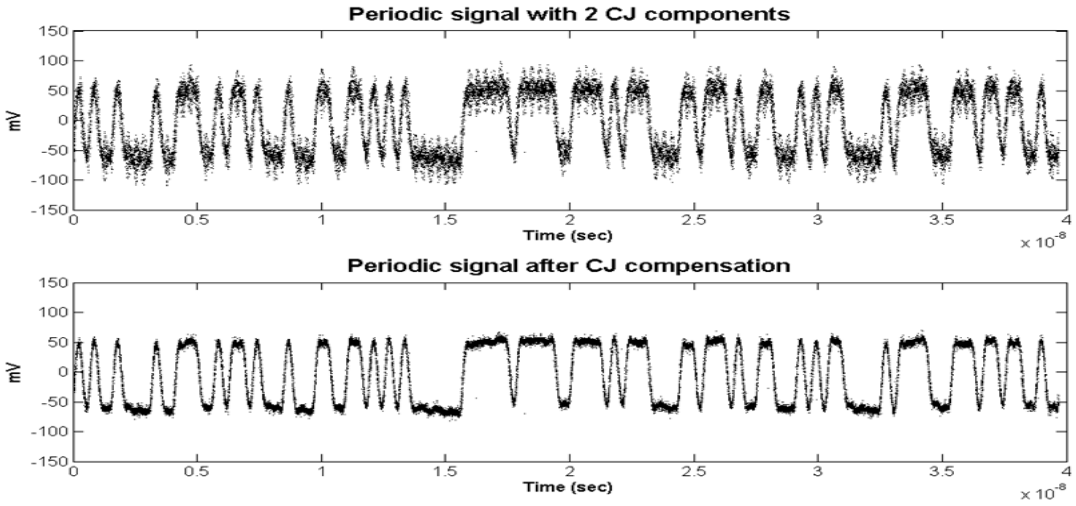

Figure 4.35 Waveform before (top) and after (bottom) crosstalk jitter compensation. The samples are folded into the period of the victim signal.

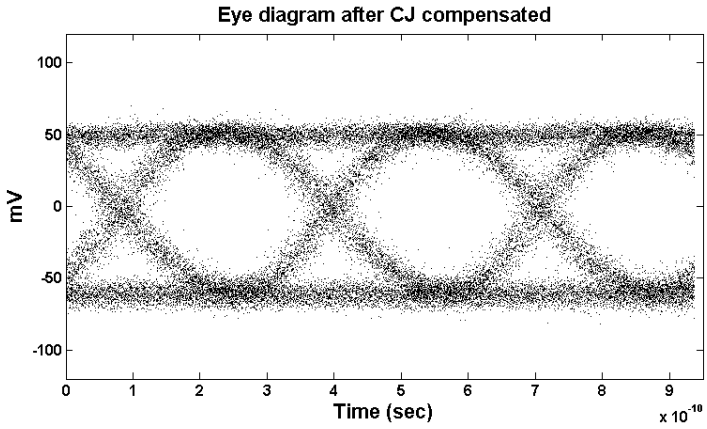

Figure 4.36 Eye diagram of the victim signal with crosstalk components removed

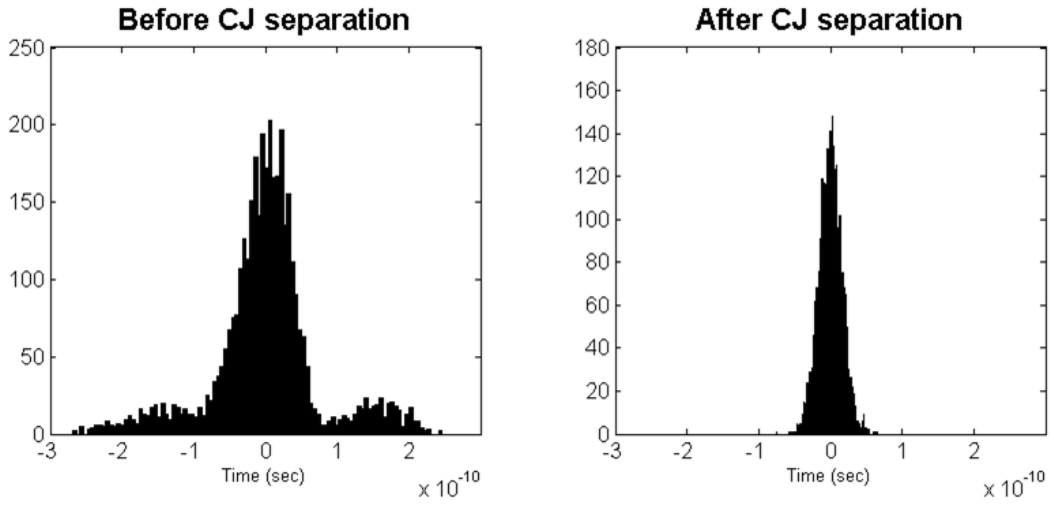

Figure 4.37 Jitter histogram before (left) and after (right) removing crosstalk jitter

4.2.7 Hardware Measurement: Crosstalk Separation with Agilent DCA-X 86100D

This section verifies the proposed method in an equivalent time sampling scheme with the use of an oscilloscope that is available on the market. As shown in Figure 4.38, a 5-bit 3.2 Gbps signal (victim), which is generated by a KC705 Kintex-7 Evaluation board, and an 8-bit 3.2 Gbps (aggressor), which is generated by the Agilent 81133A, are passed through the crosstalk board in Figure 4.31. The signal from the 5-bit signal is

digitized by an Agilent DCA-X 86100D oscilloscope with an HP 54752A Two-Channel 50 GHz module. The scope is triggered with a 5-bit period signal (640 MHz trigger signal) or an 8-bit period signal (400 MHz trigger signal), resulting in the two jittered waveforms shown in Figure 4.38. The waveforms obtained by averaging are almost the same as the waveforms acquired by turning off the aggressor or the victim signal. This shows the effectiveness of the proposed method in an equivalent time-sampling scheme. However, sampling with oscilloscopes limits access to the acquired samples. If the proposed method can be incorproated into the software of oscilloscopes, further analysis and the jitter compensation can be performed as in the last section.

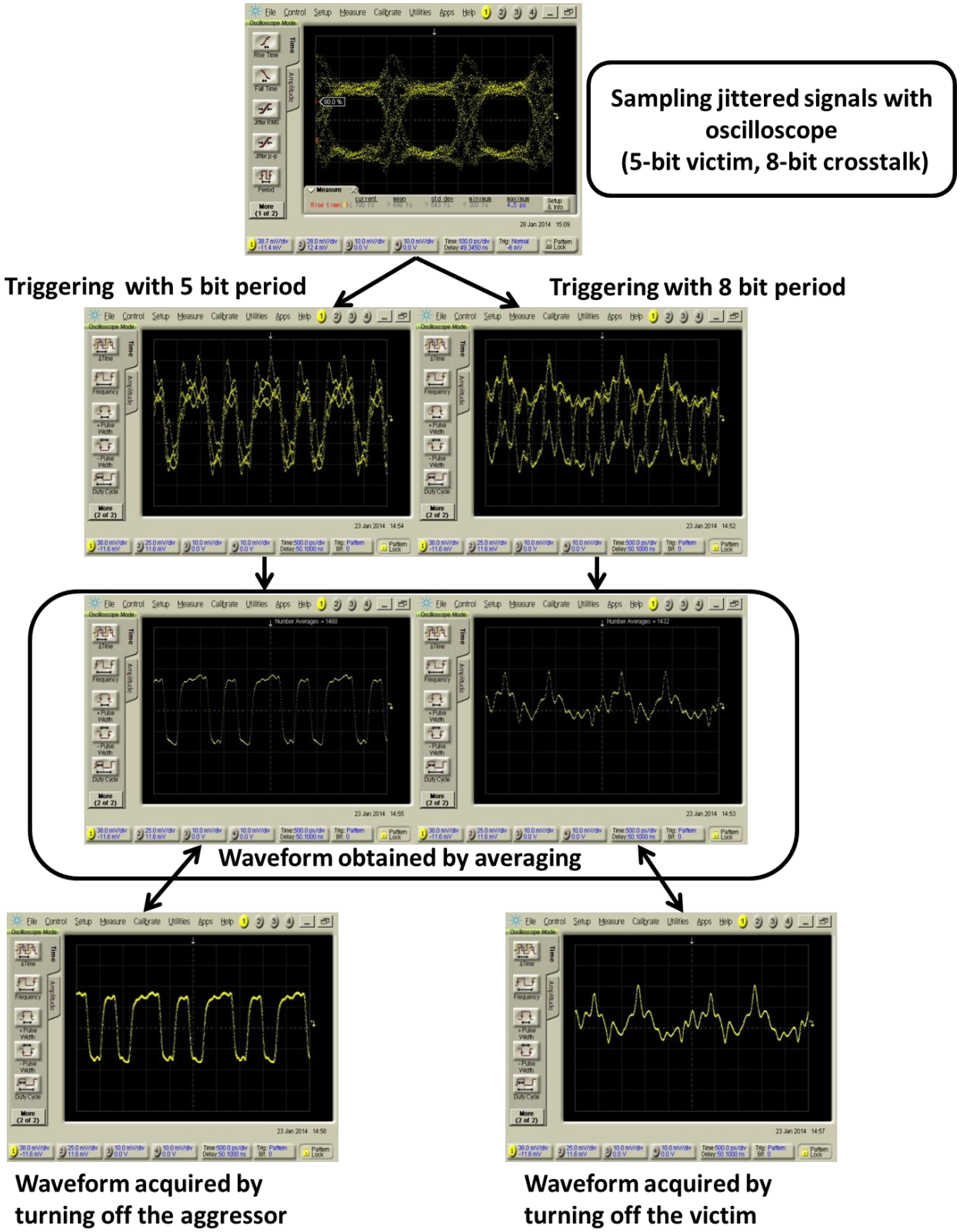

Figure 4.38 Proposed jitter separation using an Agilent DCA-X 86100D oscilloscope

4.2.8 Discussion

The extracted crosstalk components, as shown in Figure 4.34, are periodic; hence, one can find the worst-case cycle by superimposing these two crosstalk waveforms periodically and detecting the cycle with the maximum peak. Although the proposed crosstalk jitter separation method is pattern independent, it is important to find what patterns result in the worst-case crosstalk. Different patterns yield different crosstalk effects, and generally, longer sequences can be designed to have a bigger crosstalk effect. It is important to note that a PRBS sequence with a $2^n - 1$ period does not yield the worst-case pattern. With the same bit length ($2^n - 1$), one can usually design bit patterns that give a worse crosstalk effect at the cost of more memory storage.

The proposed method uses averaging to remove the effect of different periodic sequences. As can be seen in the simulation, the number of residual errors decreases as the number of samples increases. Therefore, the proposed measurement requires having enough samples, and as the lengths of different sequences increase, more samples are needed to average out different crosstalk effects. Having more samples requires more memory space to store samples and longer measurement time.

In section II B, a mathematical analysis is performed using ideal bit sequences. Periodic components can be averaged out under the assumption that the spectral power at the bit rate and its harmonic is low. In reality, duty cycle distortion and other system non-linear effects may contradict this assumption and reduce the measurement accuracy. An experiment carried out for this research showed that the reconstructed waveform becomes distorted as the assumption is violated. A 3.2Gbps 5-bit periodic victim signal was generated by the KC 705 as the victim signal. A 1.6GHz clock, which is equivalent to a

3.2Gbps 1-0 pattern, was generated by the Agilent 81133A as the aggressor. The Agilent 81133A has the ability to adjust the duty cycle of the output clock. Figure 4.39 reveals that the reconstructed victim waveform becomes more distorted as the duty cycle of the aggressor is more distorted. The spectral component of the aggressor at 3.2 GHz (bit), which corresponds to the first zero-crossing node for an ideal digital signal, contains higher energy level as the duty-cycle distortion increases. This result is consistent with the analysis in section II.B that the spectral components at the harmonic of 3.2 GHz (bit rate) can distort the reconstructed waveform.

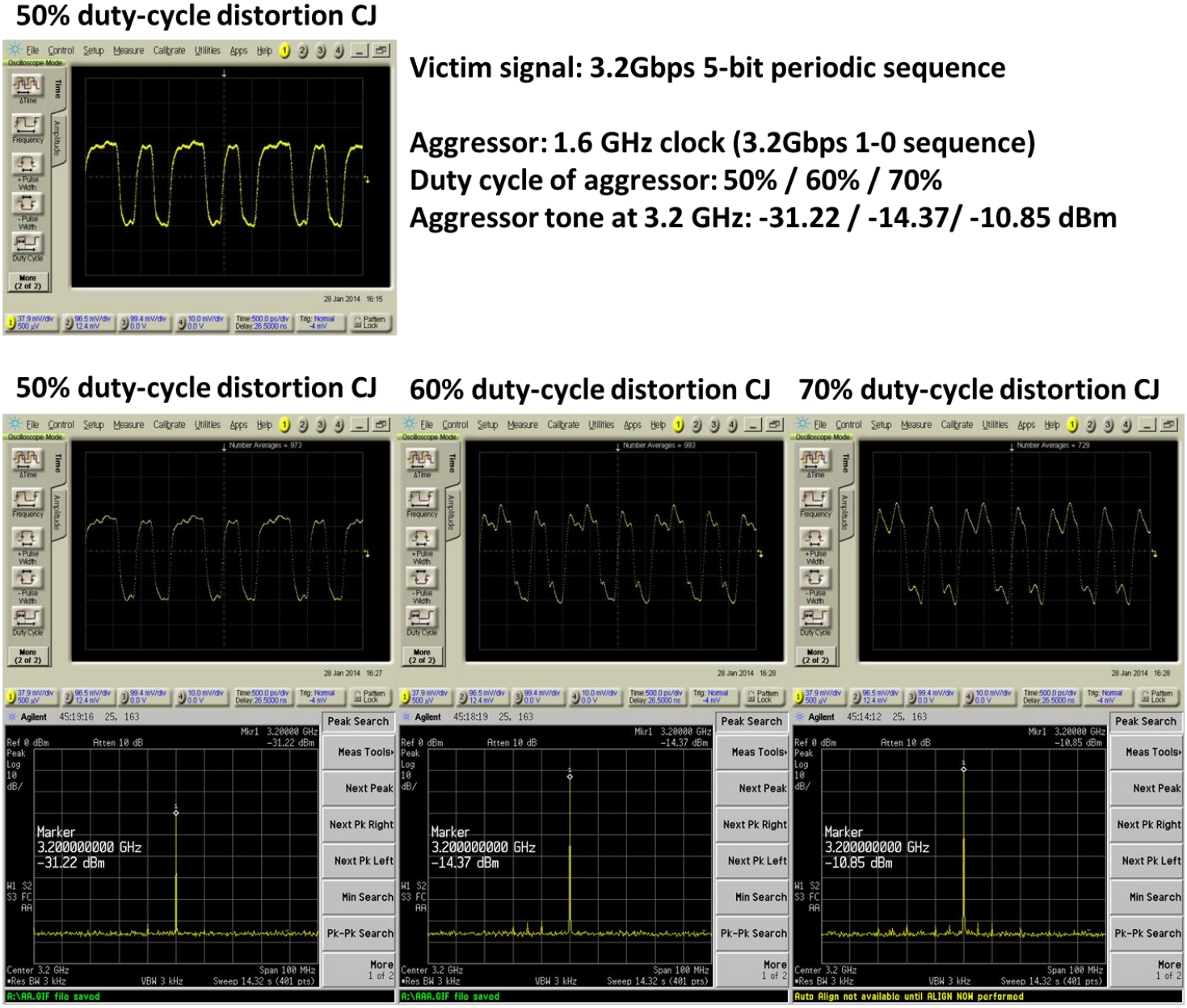

Figure 4.39 The reconstructed waveform becomes more distorted as the aggressor experiences more duty-cycle distortion and contains higher energy at 3.2 GHz (bit rate)

(Top) The victim signal measured by turning off the aggressor (Middle) The reconstructed waveform is obtained by averaging (Bottom) The spectrum of the aggressor at 3.2GHz

4.3 Summary

This chapter presents different signal and noise separation techniques. Sction 4.1 discussed and demonstrated how periodic jitter separation and compensation can be used for characterizing a DUT. The measurement result shows that the information extracted by precise characterization can be used for circuit tuning. In Sectionr 4.2, a model-free crosstalk jitter separation method is verified both by simulation and with hardware measurements. The proposed algorithm uses bit sequence stimuli with coprime periods to separate crosstalk effects from different channels. Crosstalk components from multiple channels can be determined with a single data acquisition method and the proposed method. Mathematical analysis has shown that only coprime bit length sequences can result in unbiased crosstalk measurements. The proposed method can reduce the required time for characterizing crosstalk effects in multi-channel systems.

CHAPTER 5

CONCLUSION

The final chapter concludes the research in co-designing sub-Nyquist hardware and algorithms for low-cost wideband and high-speed signal acquisition and characterization. The technical contributions of this research are summarized in Section 5.1. Potential improvement and future work are discussed in Section 5.2.

5.1 Technical Contributions

This dissertation investigates and designs low-cost systems for signal acquisition and characterization for testing. Designing such systems requires innovations in both hardware and algorithms. The thesis makes three main contributions. The first two are the low-cost systems introduced in Chapters 2 and 3. The signal acquisition system in Chapter 2 is used for characterizing the spectrum of sparse wideband signals, while the system in Chapter 3 is used for characterizing the time-domain of periodic signals. The third contribution is a crosstalk jitter separation methodology for high-speed signals, which is introduced in Chapter 4.

Chapter 2 introduces multi-rate sub-Nyquist sampling as a low-cost method for characterizing the spectrum of sparse wideband signals. The design of an asynchronous algorithm allows the hardware to acquire signals without synchronization across different parallel channels. In addition, the use of a programmable frequency synthesizer together with the asynchronous algorithms makes the hardware implementation scheme scalable from one channel to multiple channels. Compared to other sub-Nyquist sampling

schemes, the introduced method requires only minimum calibration effort. These three factors, asynchronous design, high scalability, and low required calibration effort, result in an efficient, low-cost system. The feasibility of the proposed system is demonstrated by means of a hardware prototype that was built using off-the-shelf components and verified along with the algorithms.

Chapter 3 introduced a system that combines a band-interleaved scheme with incoherent undersampling to form a low-cost time-domain waveform reconstruction system, which does not require any hardware synchronization mechanism. This advantage greatly reduces the hardware complexity. This is made possible by using back-end signal processing algorithms to compensate the lack of synchronization. Compared to other time-domain reconstruction techniques using mixers to extend the input bandwidth, the proposed system has the lowest hardware complexity. A prototype was built and tested to verify the feasibility of the proposed method.

Chapter 4 introduces a crosstalk jitter separation method for high-speed signals. The proposed method uses bit sequences with coprime periods as channel stimuli and uses a back-end signal processing algorithms to separate crosstalk jitter. With all channels being active and with one waveform acquisition of the victim channel, the proposed method can separate and characterize the waveform of each crosstalk component and the victim signal. This dramatically reduces the testing time, and thus, the cost. The methodology can be inserted into the current jitter characterization method without re-designing any hardware. Chapter 4 also investigates the mathematical analysis and the limitations of this method, concluding by describing the hardware measurement that is performed to support the proposed method.

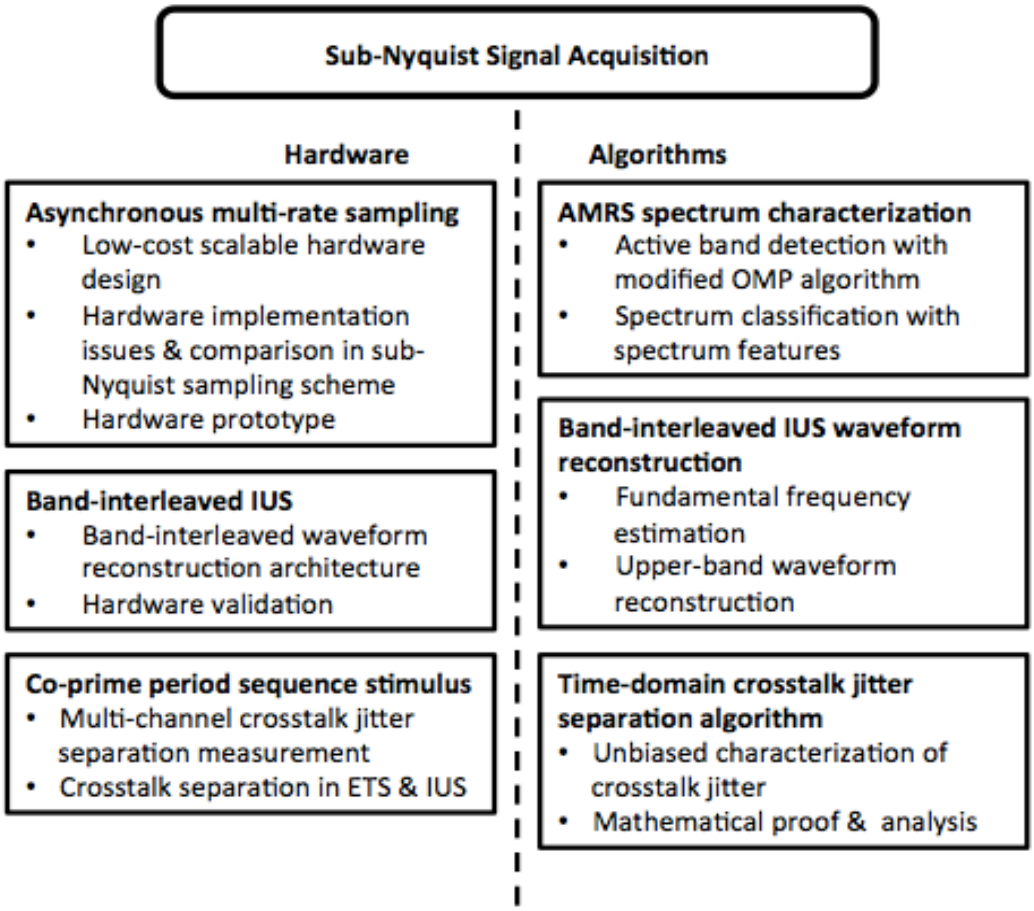

Figure 5.1 The scope of this research

The overall scope of this research can be summarized in Figure 5.1. As shown in the Figure, in all three major works, characterizing high-speed and wideband signals with low-cost hardware is achieved by co-designing hardware and algorithms.

5.2 Future Work

Low-cost system designs for testing are one of the key factors in reducing overall cost. This research has made efforts to design such systems. This research work can be extended in several different directions in the future.

The first direction is to integrate the proposed signal acquisition method into different systems. In Chapter 2 and Chapter 3, two systems are introduced. However, different systems require different levels of acquisition precision and performance. Tailoring the hardware components and algorithms for different systems to further minimize the cost is important. The low-cost integration method of the proposed systems based on the performance requirements needs further research.

The second direction is to investigate the feasibility of the proposed low-cost system in other applications that require signal acquisition. Characterizing the spectrum and the time-domain waveform of signals is important in testing as well as in many other fields. One common goal in different fields is to achieve signal characterization at a low cost or by using minimum resources.

The crosstalk jitter separation in Chapter 4 has been proven effective. The concept of using bit sequences with coprime periods needs to be integrated into the current testing and characterization of devices. The post-processing of compensating for the crosstalk jitter in the acquired samples needs to be implemented.

In summary, the main future work will be to implement and apply these proposed methods to reduce the cost and solve problems in practical cases. Another important direction for future research is to investigate the opportunities to apply the proposed systems and algorithms in different fields.

APPENDIX A

MATLAB CODE FOR CREATING FOURIER SENSING MATRIX

```
%%%%%%%%
% Function description:
%   Given samples and sampling time, Nx1 vector,
%   and the frequency to be recovered,
%   return the corresponding sensing matrix
%
% input:
%   freqSupp: frequency support, 1xN vector
%   t: sampling time of ADC, Mx1 vector
%
% output:
%   output: corresponding sensing matrix, MxN matrix
%%%%%%%%

function output = sensingMx(freqSupp, t)

M = size(t,1);
output = 1/sqrt(M)*exp(2j*pi*t*freqSupp);
```

APPENDIX B

MATLAB CODE FOR SYNC. MULTIRATE ACTIVE BANDS DETECTION

```
%%%%%%%%%%%%%%%%%%%%%%%%%%%%%%%%%%%%%%%%%%%%%%%
% Input:
% y - Samples (from all sample sets) MQx1 vector
% freqSupp - frequency support to be recovered, 1x2N vector
% t - sampling time for all samples MQx1
% K - Sparsity level (number of nonzero coefficient), integer
%
% Output:
% x - Recovered spectral coefficient, 2Nx1 vector
%%%%%%%%%%%%%%%%%%%%%%%%%%%%%%%%%%%%%%%%%%%%%%%

function x = OMP_F_k(y,freqSupp,t,k)

N = size(freqSupp,2);
PHI = sensingMx(freqSupp, t); % create sensing matrix
% Step1: Initialization
res = y;
x = zeros(N,1);
selInd = [];

for ii = 1:k
    % Calculate proxy
    proxy = PHI'*res;

    % select maximum index
    [ maxVal, maxInd ] = max(abs(proxy));

    % Sort all the selected indicies
    selInd = [selInd; maxInd; N-maxInd+1];

    % Update x
    x_est = pinv(PHI(:,selInd))*y;
    x(selInd) = x_est;

    % Update residual
    res = y - real(PHI*x);
end
```

APPENDIX C

MATLAB CODE FOR ASYNCHRONOUS MULTIRATE ACTIVE BANDS DETECTION

```
%%%%%%%%%%%%%%%%%%%%%%%%%%%%%%%%%%%%%%%%%%%%%%%
% M: Sample number form each set
% Q: Number of sets
% Input:
% Y - Samples from ADC MxQ
% freqSupp - frequency support to be recovered 1xN
% TS - sampling time for each set MxQ
% BLK - BLK size
% Output:
% X - Recovered spectral coefficient NxQ
%%%%%%%%%%%%%%%%%%%%%%%%%%%%%%%%%%%%%%%%%%%%%%%
function [X, selInd] = MR_ASYNC_BLK(Y,freqSupp,TS,BLK)

N = size(freqSupp,2);
M = size(Y,1);
Q = size(Y,2);
PHI = [];
for ii = 1:Q
    PHI = cat(3,PHI,sensingMx(freqSupp, TS(:,ii)));
end
res = Y;
X = zeros(N,Q);
selInd = [];
while(sum(sqrt(sum(res.^2)./sum(Y.^2)))>0.65*Q)
    % Calculate proxy for different sampling set
    proxy = [];
    for jj = 1:Q
        proxy = [proxy, abs(PHI(:,:,jj)'*res(:,jj))];
    end
    % Calculate minimum proxy among two measurement
    proxyMin = min(proxy, [], 2);

    % Convolve with a window to find the center of a block
    proxyMin = conv(proxyMin,ones(2*BLK+1,1));
    proxyMin = proxyMin(BLK+1:end-BLK);

    % Find the largest components
    [ maxVal, maxInd ] = max(proxyMin);

    % Add the indice to the indice set
    selInd = [selInd; (maxInd+(-BLK:BLK)'); (N-(maxInd+(-BLK:BLK)')+1)];
    selInd = unique(selInd);

    % Update each sample set
    for jj = 1:Q
        % min|y - PHI1*x1_ind|_2
        x_est = pinv(PHI(:,selInd,jj))*Y(:,jj);
```

```
            X(selInd,jj) = x_est; % Update x
            res(:,jj) = Y(:,jj) - real(PHI(:,:,jj)*X(:,jj)); % Update res
        end
    end

    end
```

REFERENCES

[1] USB Implementers Forum, "Universal Serial Bus 3.0 Specification," June 2011 [Online]. http://www.usb.org/developers/docs/usb_30_spec_071012.zip (Accessed Aug. 12, 2012).

[2] High-Definition Multimedia Interface, "What functionality was added to each version of HDMI?" [Online]. http://www.hdmi.org/learningcenter/faq.aspx#12.

[3] VESA, "Why DisplayPort." [Online]. http://www.vesa.org/displayport-developer/why-displayport.

[4] Intel, "Thunderbolt Technology: Overview." [Online]. http://www.intel.com/content/dam/www/public/us/en/documents/product-briefs/thunderbolt-overview-brief.pdf.

[5] Status of Project IEEE 802.11ac [Online]. Available: http://www.ieee802.org/11/Reports/tgac_update.htm (Accessed Aug. 12, 2012).

[6] Wireless Gigabit Alliance, "WiGig White Paper: Defining the Future of Multi-Gigabit Wireless Communications," July 2010 [Online]. Available: http://wirelessgigabitalliance.org/?getfile=1510 (Accessed Aug. 12, 2012).

[7] Status of Project IEEE 802.11ad [Online]. Available: http://www.ieee802.org/11/Reports/tgad_update.htm (Accessed Aug. 12, 2012).

[8] WirelessHD, "WirelessHD Specification Version 1.1 Overview," May 2010. [Online]. Available: http://www.wirelesshd.org/pdfs/WirelessHD-Specification-Overview-v1.1May2010.pdf.

[9] Natarajan, Vishwanath, et al, "BIST driven power conscious post-manufacture tuning of wireless transceiver systems using hardware-iterated gradient search." Asian Test Symposium, 2009. ATS'09.. IEEE, 2009.

[10] Senguttuvan, Rajarajan, Shreyas Sen, and Abhijit Chatterjee. "VIZOR: Virtually zero margin adaptive RF for ultra-low power wireless communication." Computer Design, 2007. ICCD 2007. 25th International Conference on. IEEE, 2007.

[11] Ashouei, Maryam, et al. "Probabilistic self-adaptation of nanoscale CMOS circuits: yield maximization under increased intra-die variations." VLSI Design, 2007. Held jointly with 6th International Conference on Embedded Systems., 20th International Conference on. IEEE, 2007.

[12] Prony, R. "Essai Expérimental et Analytique sur les lois de la Dilatabilité des fluides élastiques et sur celles da la Force expahsive de la vapeur de l'eau et de la vapeur de l'alkool,a différentes températures." Journal Polytechnique du Bulletin du Travail faita L'Ecole Centrale des Travaux Publics, Paris, Premier Cahier, An. III (1795).

[13] Carathéodory, Constantin. "Über den Variabilitätsbereich der Koeffizienten von Potenzreihen, die gegebene Werte nicht annehmen." Mathematische Annalen 64, no. 1 (1907): 95-115.

[14] Carathéodory, Constantin. "Über den Variabilitätsbereich der Fourier'schen Konstanten von positiven harmonischen Funktionen." Rendiconti del Circolo Matematico di Palermo (1884-1940) 32, no. 1 (1911): 193-217.

[15] Eldar, Yonina C., and Gitta Kutyniok, eds. Compressed sensing: theory and applications. Cambridge University Press, 2012.

[16] Gorodnitsky, Irina F., John S. George, and Bhaskar D. Rao. "Neuromagnetic source imaging with FOCUSS: a recursive weighted minimum norm algorithm." Electroencephalography and clinical Neurophysiology 95, no. 4 (1995): 231-251.

[17] Gorodnitsky, Irina F., and Bhaskar D. Rao. "Sparse signal reconstruction from limited data using FOCUSS: A re-weighted minimum norm algorithm." Signal Processing, IEEE Transactions on 45, no. 3 (1997): 600-616.

[18] Gorodnitsky, Irina F., Bhaskar D. Rao, and J. George. "Source localization in magnetoencephalography using an iterative weighted minimum norm algorithm." In Signals, Systems and Computers, 1992. 1992 Conference Record of The Twenty-Sixth Asilomar Conference on, pp. 167-171. IEEE, 1992.

[19] Rao, Bhaskar D. "Signal processing with the sparseness constraint." In Acoustics, Speech and Signal Processing, 1998. Proceedings of the 1998 IEEE International Conference on, vol. 3, pp. 1861-1864. IEEE, 1998.

[20] Bresler, Yoram, and Ping Feng. "Spectrum-blind minimum-rate sampling and reconstruction of 2-D multiband signals." In Image Processing, 1996. Proceedings., International Conference on, vol. 1, pp. 701-704. IEEE, 1996.

[21] P. Feng. "Universal spectrum blind minimum rate sampling and reconstruction of Multi-band signals. PhD thesis, University of Illinois at Urbana-Champaign, Mar. 1997.

[22] Feng, Ping, and Yoram Bresler. "Spectrum-blind minimum-rate sampling and reconstruction of multiband signals." In Acoustics, Speech, and Signal Processing, 1996. ICASSP-96. Conference Proceedings., 1996 IEEE International Conference on, vol. 3, pp. 1688-1691. IEEE, 1996.

[23] Venkataramani, Raman, and Yoram Bresler. "Further results on spectrum blind sampling of 2D signals." In Image Processing, 1998. ICIP 98. Proceedings. 1998 International Conference on, vol. 2, pp. 752-756. IEEE, 1998.

[24] Vetterli, Martin, Pina Marziliano, and Thierry Blu. "Sampling signals with finite rate of innovation." Signal Processing, IEEE Transactions on 50, no. 6 (2002): 1417-1428.

[25] Candès, Emmanuel J. "Compressive sampling." In Proceedings of the International Congress of Mathematicians: Madrid, August 22-30, 2006: invited lectures, pp. 1433-1452. 2006.

[26] Candes, Emmanuel J., and Justin Romberg. "Quantitative robust uncertainty principles and optimally sparse decompositions." Foundations of Computational Mathematics 6, no. 2 (2006): 227-254.

[27] Candès, Emmanuel J., Justin Romberg, and Terence Tao. "Robust uncertainty principles: Exact signal reconstruction from highly incomplete frequency information." Information Theory, IEEE Transactions on 52, no. 2 (2006): 489-509.

[28] Candes, Emmanuel J., Justin K. Romberg, and Terence Tao. "Stable signal recovery from incomplete and inaccurate measurements." Communications on pure and applied mathematics 59, no. 8 (2006): 1207-1223.

[29] Candes, Emmanuel J., and Terence Tao. "Near-optimal signal recovery from random projections: Universal encoding strategies?." Information Theory, IEEE Transactions on 52, no. 12 (2006): 5406-5425.

[30] Donoho, David L. "Compressed sensing." Information Theory, IEEE Transactions on 52, no. 4 (2006): 1289-1306.

[31] Yucek, Tevfik, and Huseyin Arslan. "A survey of spectrum sensing algorithms for cognitive radio applications." Communications Surveys & Tutorials, IEEE 11.1 (2009): 116-130.

[32] Collab Akyildiz, Ian F., Brandon F. Lo, and Ravikumar Balakrishnan. "Cooperative spectrum sensing in cognitive radio networks: A survey." Physical Communication 4.1 (2011): 40-62.

[33] Akyildiz, I. F., Lee, W. Y., Vuran, M. C., & Mohanty, S. (2006). NeXt generation/dynamic spectrum access/cognitive radio wireless networks: a survey. Computer Networks, 50(13), 2127-2159.

[34] Akyildiz, I. F., Lee, W. Y., Vuran, M. C., & Mohanty, S. (2008). A survey on spectrum management in cognitive radio networks. Communications Magazine, IEEE, 46(4), 40-48.

[35] Axell, E., Leus, G., Larsson, E. G., & Poor, H. V. (2012). Spectrum sensing for cognitive radio: State-of-the-art and recent advances. Signal Processing Magazine, IEEE, 29(3), 101-116.

[36] Cabric, Danijela, Shridhar Mubaraq Mishra, and Robert W. Brodersen. "Implementation issues in spectrum sensing for cognitive radios." Signals, systems and computers, 2004. Conference record of the thirty-eighth Asilomar conference on. Vol. 1. IEEE, 2004.

[37] Ma, Jun, Geoffrey Ye Li, and Biing Hwang Juang. "Signal processing in cognitive radio." Proceedings of the IEEE 97.5 (2009): 805-823.

[38] Ghasemi, Amir, and Elvino S. Sousa. "Collaborative spectrum sensing for opportunistic access in fading environments." New Frontiers in Dynamic Spectrum

Access Networks, 2005. DySPAN 2005. 2005 First IEEE International Symposium on. IEEE, 2005.

[39] Mishra, S. M., Sahai, A., & Brodersen, R. W. (2006, June). Cooperative sensing among cognitive radios. In Communications, 2006. ICC'06. IEEE International Conference on (Vol. 4, pp. 1658-1663). IEEE.

[40] Venkataramani, Raman, and Yoram Bresler. "Optimal sub-Nyquist nonuniform sampling and reconstruction for multiband signals." Signal Processing, IEEE Transactions on 49, no. 10 (2001): 2301-2313.

[41] Lu, Yue M., and Minh N. Do. "A theory for sampling signals from a union of subspaces." Signal Processing, IEEE Transactions on 56, no. 6 (2008): 2334-2345.

[42] Mishali, Moshe, and Yonina C. Eldar. "Blind multiband signal reconstruction: Compressed sensing for analog signals." Signal Processing, IEEE Transactions on 57.3 (2009): 993-1009.

[43] Image from website: http://webee.technion.ac.il/people/YoninaEldar/xampling_modulated_wideband_converter.php

[44] Mishali, Moshe, and Yonina C. Eldar. "From theory to practice: Sub-Nyquist sampling of sparse wideband analog signals." Selected Topics in Signal Processing, IEEE Journal of 4, no. 2 (2010): 375-391.

[45] Eldar, Yonina C., and Alan V. Oppenheim. "Filterbank reconstruction of bandlimited signals from nonuniform and generalized samples." Signal Processing, IEEE Transactions on 48, no. 10 (2000): 2864-2875.

[46] Johansson, Håkan, and Per Lowenborg. "Reconstruction of nonuniformly sampled bandlimited signals by means of digital fractional delay filters." Signal Processing, IEEE Transactions on 50, no. 11 (2002): 2757-2767.

[47] Elbornsson, Jonas, Fredrik Gustafsson, and J-E. Eklund. "Blind equalization of time errors in a time-interleaved ADC system." Signal Processing, IEEE Transactions on 53, no. 4 (2005): 1413-1424.

[48] Pfetsch, Stephen, Tamer Ragheb, Jason Laska, Hamid Nejati, Anna Gilbert, Martin Strauss, Richard Baraniuk, and Yehia Massoud. "On the feasibility of hardware implementation of sub-nyquist random-sampling based analog-to-information conversion." In Circuits and Systems, 2008. ISCAS 2008. IEEE International Symposium on, pp. 1480-1483. IEEE, 2008.

[49] Wakin, Michael, Stephen Becker, Eric Nakamura, Michael Grant, Emilio Sovero, Daniel Ching, Juhwan Yoo, Justin Romberg, Azita Emami-Neyestanak, and Emmanuel Candes. "A nonuniform sampler for wideband spectrally-sparse environments." (2012): 1-14.

[50] Polo, Yvan Lamelas, Ying Wang, Ashish Pandharipande, and Geert Leus. "Compressive wide-band spectrum sensing." In Acoustics, Speech and Signal Processing, 2009. ICASSP 2009. IEEE International Conference on, pp. 2337-2340. IEEE, 2009.

[51] Tropp, Joel A., Jason N. Laska, Marco F. Duarte, Justin K. Romberg, and Richard G. Baraniuk. "Beyond Nyquist: Efficient sampling of sparse bandlimited signals." Information Theory, IEEE Transactions on 56, no. 1 (2010): 520-544.

[52] Ragheb, Tamer, Jason N. Laska, Hamid Nejati, Sami Kirolos, Richard G. Baraniuk, and Yehia Massoud. "A prototype hardware for random demodulation based compressive analog-to-digital conversion." In Circuits and Systems, 2008. MWSCAS 2008. 51st Midwest Symposium on, pp. 37-40. IEEE, 2008.

[53] Carmi, Avishy, Lyudmila Mihaylova, and Simon Godsill. "Compressed sensing and sparse filtering." (2013).

[54] Mishali, Moshe, Yonina C. Eldar, Oleg Dounaevsky, and Eli Shoshan. "Xampling: Analog to digital at sub-Nyquist rates." IET circuits, devices & systems 5, no. 1 (2011): 8-20.

[55] Rosenthal, Amir, Alex Linden, and Moshe Horowitz. "Multirate asynchronous sampling of sparse multiband signals." JOSA A 25.9 (2008): 2320-2330.

[56] Fleyer, M., Linden, A., Horowitz, M., & Rosenthal, A. (2010). Multirate synchronous sampling of sparse multiband signals. Signal Processing, IEEE Transactions on, 58(3), 1144-1156.

[57] Fleyer, M., Horowitz, M., Feldtser, A., & Smulakovsky, V. (2010). Multi-rate synchronous optical undersampling of several bandwidth-limited signals. Optics Express, 18(16), 16929-16945.

[58] Tektronix: Oscilloscope Fundamentals. Online: http://circuitslab.case.edu/manuals/Oscilloscope_Fundamentals_-_Tektronix.pdf

[59] Pupalaikis, Peter J. "An 18 GHz bandwidth, 60 GS/s sample rate real-time waveform digitizing system." In Microwave Symposium, 2007. IEEE/MTT-S International, pp. 195-198. IEEE, 2007.

[60] I. Shake, H. Takara, and S. Kawanishi, “Simple measurement of eye diagram and ber using high-speed asynchronous sampling,” Lightwave Technology, Journal of, vol. 22, no. 5, pp. 1296 – 1302, May 2004.

[61] L. Noirie, F. Cerou, G. Moustakides, O. Audouin, and P. Peloso, “New transparent optical monitoring of the eye and ber using asynchronous under-sampling of the signal,” in Optical Communication, 2002. ECOC 2002. 28th European Conference on, vol. 5, 2002, pp. 1 –2.

[62] E. Mobilon, M. de Barros, and A. Lopes, “Experimental verification of an eye diagram reconstruction technique based on asynchronous undersampling,” in Microwave and Optoelectronics, 2005 SBMO/IEEE MTT-S International Conference on, 2005, pp. 603 – 606.

[63] I. Shake, H. Takara, and S. Kawanishi, “Simple q factor monitoring for ber estimation using opened eye diagrams captured by high-speed asynchronous electrooptical sampling,” Photonics Technology Letters, IEEE, vol. 15, no. 4, pp. 620 –622, 2003.

[64] Choi, Hyun, Alfred V. Gomes, and Abhijit Chatterjee. "Signal acquisition of high-Speed periodic signals using incoherent sub-sampling and back-end signal reconstruction algorithms." Very Large Scale Integration (VLSI) Systems, IEEE Transactions on 19, no. 7 (2011): 1125-1135.

[65] Shimanouchi, M.; Li, M.P.; Chow, D.; , "New modeling methods for bounded Gaussian jitter (BGJ)/noise (BGN) and their applications in jitter/noise estimation/testing," Test Conference, 2009. ITC 2009. International , vol., no., pp.1-8, 1-6 Nov. 2009

[66] M. Li, J. Wilstrup, R. Jessen, D. Petrich, “A New Method for Jitter Decomposition Through Its Distribution Tail Fitting “, ITC Proceeding, 1999.

[67] Kim, Gawon, et al. "Modeling of eye-diagram distortion and data-dependent jitter in meander delay lines on high-speed printed circuit boards (PCBs) based on a time-domain even-mode and odd-mode analysis." Microwave Theory and Techniques, IEEE Transactions on 56.8 (2008): 1962-1972.

[68] Kuo, A.; Rosales, R.; Farahmand, T.; Tabatabaei, S.; Ivanov, A.; , "Crosstalk bounded uncorrelated jitter (BUJ) for high-speed interconnects," Instrumentation and Measurement, IEEE Transactions on , vol.54, no.5, pp. 1800- 1810, Oct. 2005.

[69] Stephens, R., ed. "Crosstalk problems are back." Test & Measurement World 32.6 (2012): 16-22.

[70] Buckwalter, James F., and Ali Hajimiri. "Cancellation of crosstalk-induced jitter." Solid-State Circuits, IEEE Journal of 41.3 (2006): 621-632.

[71] “Analyzing Jitter Using a Spectrum Approach” [Online] Tektronix Application Note http://e-sites2.tek.com/cmswpt/tidetails.lotr?ct=TI&cs=apn&ci=2291&lc=EN

[72] “Understanding and Characterizing Timing Jitter” [Online] National Instruments http://www.ni.com/white-paper/14227/en/

[73] “Fibre Channel – Methodologies for Jitter Specification,” National Committee for Information Technology Standardization (NCITS) Technical Report T11.2/Project 1230/Rev 10.0, Jun. 1999.

[74] Li, Mike Peng. Jitter, noise, and signal integrity at high-speed. Pearson Education, 2007.

[75] Stephens, R., ed. "Crosstalk problems are back." Test & Measurement World 32, no. 6 (2012): 16-22.

[76] Tian, Zhi, and Georgios B. Giannakis. "Compressed sensing for wideband cognitive radios." Acoustics, Speech and Signal Processing, 2007. ICASSP 2007. IEEE International Conference on. Vol. 4. IEEE, 2007

[77] Laska, J., Kirolos, S., Massoud, Y., Baraniuk, R., Gilbert, A., Iwen, M., & Strauss, M. (2006, October). Random sampling for analog-to-information conversion of wideband signals. In Design, Applications, Integration and Software, 2006 IEEE Dallas/CAS Workshop on (pp. 119-122). IEEE.

[78] Kirolos, Sami, et al. "Analog-to-information conversion via random demodulation." Design, Applications, Integration and Software, 2006 IEEE Dallas/CAS Workshop on. IEEE, 2006.

[79] Laska, Jason N., et al. "Theory and implementation of an analog-to-information converter using random demodulation." Circuits and Systems, 2007. ISCAS 2007. IEEE International Symposium on. IEEE, 2007.

[80] Ragheb, Tamer, et al. "A prototype hardware for random demodulation based compressive analog-to-digital conversion." Circuits and Systems, 2008. MWSCAS 2008. 51st Midwest Symposium on. IEEE, 2008.

[81] Bhatta, Debesh, Joshua W. Wells, and Abhijit Chatterjee. "Time domain characterization and test of high speed signals using incoherent sub-sampling." Test Symposium (ATS), 2011 20th Asian. IEEE, 2011.

[82] Domınguez-Jiménez, M. E., and N. González-Prelcic. "ANALYSIS AND DESIGN OF MULTIRATE SYNCHRONOUS SAMPLING SCHEMES FOR SPARSE MULTIBAND SIGNALS." (2012).

[83] Sun, H., Nallanathan, A., Jiang, J., & Wang, C. X. (2013). Multi-rate Sub-Nyquist Spectrum Sensing in Cognitive Radios. arXiv preprint arXiv:1302.1489.

[84] Babu, DV Srihari, and P. Chandrashekhar Reddy. "Advancements of Multirate Signal Processing for Wireless Communication Networks: Current State of the Art." Global Journal of Computer Science and Technology 12.13-E (2012).

[85] Feldster, A., Shapira, Y. P., Horowitz, M., Rosenthal, A., Zach, S., & Singer, L. (2009). Optical under-sampling and reconstruction of several bandwidth-limited signals. Journal of Lightwave Technology, 27(8), 1027-1033.

[86] Tropp, Joel A., and Anna C. Gilbert. "Signal recovery from random measurements via orthogonal matching pursuit." Information Theory, IEEE Transactions on 53.12 (2007): 4655-4666.

[87] Bhatta, Debesh, Aritra Banerjee, Sabyasachi Deyati, Nicholas Tzou, and Abhijit Chatterjee. "Low cost signal reconstruction based testing of RF components using incoherent undersampling." In *Test Workshop (LATW),*

[88] LMX2541Ultra-Low Noise PLLatinum Frequency Synthesizer with Integrated VCO http://www.ti.com/product/lmx2541

[89] A. Kuo, T. Farahmand, N. Ou, S. Tabatabaei, and A. Ivanov, “Jitter models and measurement methods for high-speed serial interconnects,” in Proc. IEEE Int. Test Conf., Charlotte, NC, 2004, pp. 1295–1302.

[90] John Patrin, Mike Li, “Comparison and Correlation of Signal Integrity Measurement Techniques,” DesignCon 2002.

[91] P. Heydani and M. Pedram, “Analysis of jitter due to power-supply noise in phase-locked loops,” in Proc. IEEE 2000 Custom Integrated Circuits Conf., 2000, pp. 443–446.

[92] Jitter Analysis Techniques for High Data Rates, Agilent Technologies Inc., Application Note 1432, February 2003

[93] A. Mehrotra, “Noise analysis of phase-locked loops,” in Proc. IEEE Int.Conf. Computer-Aided Design, Nov. 2000, pp. 277–282.

[94] Sam Chang and D. Oh, “System-level modeling and simulation of periodic jitter in high-speed links,” in IEEE 19th Conference on Elect. Performance of Electron. Package and System, Austin, Texas, Oct. 2010, pp.117-120.

[95] Sunter, Stephen, and Aubin Roy. "On-chip digital jitter measurement, from megahertz to gigahertz." Design & Test of Computers, IEEE 21.4 (2004): 314-321.

[96] Rearick, Jeff, and Aaron Volz. "A Case Study of Using IEEE P1687 (IJTAG) for High-Speed Serial I/O Characterization and Testing." In Test Conference, 2006. ITC'06. IEEE International, pp. 1-8. IEEE, 2006.

[97] Casper, Bryan, Aaron Martin, James E. Jaussi, Joe Kennedy, and Randy Mooney. "An 8-Gb/s simultaneous bidirectional link with on-die waveform capture." Solid-state Circuits, IEEE Journal of 38, no. 12 (2003): 2111-2120.

[98] Jeruchim, Michel. "Techniques for estimating the bit error rate in the simulation of digital communication systems." Selected Areas in Communications, IEEE Journal on 2.1 (1984): 153-170.

[99] Stojanovic, Vladimir, and Mark Horowitz. "Modeling and analysis of high-speed links." Custom Integrated Circuits Conference, 2003. Proceedings of the IEEE 2003. IEEE, 2003.

[100] Cai, Yi, et al. "Jitter testing for multi-gigabit backplane SerDes-techniques to decompose and combine various types of jitter." Test Conference, 2002. Proceedings. International. IEEE, 2002.

[101] Tzou, Nicholas L., Debesh Bhatta, Sen-Wen Hsiao, and Abhijit Chatterjee. "Periodic jitter and bounded uncorrelated jitter decomposition using incoherent undersampling." In Proceedings of the Conference on Design, Automation and Test in Europe, pp. 1667-1672. EDA Consortium, 2013.

[102] Tzou, Nicholas, et al. "Low-cost wideband periodic signal reconstruction using incoherent undersampling and back-end cost optimization." Test Conference (ITC), 2012 IEEE International. IEEE, 2012.

[103] Pupalaikis, Peter J. "Digital bandwidth interleaving." LeCroyTM Technical Brief (2005).

[104] Knierim, Daniel G. "Test and measurement instrument including asynchronous time-interleaved digitizer using harmonic mixing." U.S. Patent Application 13/116,234.

[105] Bhatta, Debesh, et al. "Time Domain Reconstruction of Incoherently Undersampled Periodic Waveforms Using Bandwidth Interleaving." Test Symposium (ATS), 2013 22nd Asian. IEEE, 2013.

PUBLICATION

Conference Papers:

[1] **Nicholas L. Tzou**, Xian Wang, Thomas Moon, Hyun Choi, Abhijit Chatterjee, "Dual-frequency Incoherent Sub-sampling Technique Driven Signal Reconstruction of Spectrally Sparse Wideband Signals with Enhanced Time/Frequency Resolution," *2012 VLSI Testing Symposium*

[2] **Nicholas L. Tzou**, Debesh Bhatta, Sen-Wen Hsiao, Hyun Woo Choi, Abhijit Chatterjee, "Low-Cost Wideband Periodic Signal Reconstruction Using Incoherent Undersampling and Back-end Cost Optimization," *2012 International Testing Coference*

[3] Thomas Moon, **Nicholas L. Tzou**, Xian Wang, Hyun Choi, Abhijit Chatterjee," Dual-Frequency Incoherent Subsampling Driven Test Response Acquisition of Spectrally Sparse Wideband Signals with Enhanced Time Resolution," *2012 VLSI Testing Symposium*

[4] Xian Wang, **Nicholas L. Tzou**, Thomas Moon, Hyun Choi, Abhijit Chatterjee," Multi-Nyquist Waveform Synthesis and Digital Phase Noise Injection for Low Cost Test Using Time-Interleaved Data Converters," *2012 International Testing Coference*

[5] **Nicholas L. Tzou**, Debesh Bhatta, Sen-Wen Hsiao, Abhijit Chatterjee," Periodic Jitter and Bounded Uncorrelated Jitter Decomposition Using Incoherent Undersampling," *2013 Design Automation & Test in Europe*

[6] Sen-Wen Hsiao, **Nicholas L. Tzou**, Debesh Bhatta, Abhijit Chatterjee," 24GHZ Dual Core PLL Design for 60 GHz Transceiver and Efficient Validation Methodology," *2012 Asia Pacific Microwave Conference*

[7] Debesh Bhatta, **Nicholas Tzou**, Hyun Choi, and Abhijit Chatterjee. "Spectral

Estimation Based Acquisition of Incoherently Under-Sampled Periodic Signals: Application to Bandwidth Interleaving." In *Asian Test Symposium (ATS), 2012 IEEE 21st Asian, pp. 196-201. IEEE, 2012*.

[8] Sen-Wen Hsiao, **Nicholas L. Tzou**, Abhijit Chatterjee, "A Programmable BIST Design for PLL Static Phase Offset Estimation and Clock Duty Cycle Detection," *2013 VLSI Test Symposium*

[9] Debesh Bhatta, Aritra Banerjee, Sabyasachi Deyati, **Nicholas Tzou**, and Abhijit Chatterjee. "Low cost signal reconstruction based testing of RF components using incoherent undersampling." In *Test Workshop (LATW), 2013 14th Latin American, pp. 1-5. IEEE, 2013*.

[10] Debesh Bhatta, **Nicholas Tzou**, Sen-wen Hsiao, and Abhijit Chatterjee. "Time Domain Reconstruction of Incoherently Undersampled Periodic Waveforms Using Bandwidth Interleaving." In *Asian Test Symposium (ATS), 2013 22nd Asian, pp. 283-288. IEEE, 2013*.

Journal Papers:

[11] Sen-Wen Hsiao, Xain Wang, **Nicholas Tzou**, Debesh Bhatta, Abhijit Chatterjee. "Analog-based Sensor Testing for Phase-locked Loop Reference Spur and Loop Behavior", submitted to *IEEE Transactions on Circuits and Systems I, 2014*.

[12] **Nicholas L. Tzou**, Debesh Bhatta, Xian Wang, Sen-Wen Hsiao, Barry Muldrey, Hyun Woo Choi, and Abhijit Chatterjee. "Parallel Multi-Channel Crosstalk Jitter Separation Using Periodic Bit Sequences with Coprime Bit Periods", submitted to *Computer-Aided Design of Integrated Circuits and Systems, 2014*.

[12] **Nicholas L. Tzou**, Debesh Bhatta, Barry Muldrey, and Abhijit Chatterjee. “Low-Cost Hardware and Algorithm Design for Sparse Multiband Signal Characterization Using Asynchronous Multirate Sampling”, submitted to *IEEE Transactions on Circuits and Systems I, 2014*.

VITA

Nicholas L. Tzou

Nicholas Lin Tzou was born in Atlanta, Georgia. He grew up in Taipei, Taiwan and received the B.S. degree in Electrical Engineering from National Taiwan University in 2009. He joined Georgia Institute of Technology to work toward the Ph.D. degree in 2009 Fall. He received his Ph.D. degree in 2014 Spring.

From June 2012 to January 2013, he was a graduate architect intern in an Intel Architecture group in Chandler, Arizona. From May 2013 to August 2013, he served as HW/SW engineer intern in an Intel signal integrity team in Santa Clara, California. He has broad research interests in signal processing, compressed sensing, dimension reduction for high-dimensional data, parallel programming, hardware-software co-design, and signal integrity measurement and characterization. In March 2014, He joined Agilent Technologies and serve as an Advanced R&D in the High-Speed Digital team, EE Measurement Group.